Physics Reports 908 (2021) 1–65

Contents lists available at ScienceDirect

Physics Reports

journal homepage: www.elsevier.com/locate/physrep

Controlling macroscopic heat transfer with thermal metamaterials: Theory, experiment and application

Shuai Yang [a], Jun Wang [a], Gaole Dai [b], Fubao Yang [a], Jiping Huang [a,*]

[a] Department of Physics, State Key Laboratory of Surface Physics, and Key Laboratory of Micro and Nano Photonic Structures (MOE), Fudan University, Shanghai 200438, China
[b] School of Sciences, Nantong University, Nantong 226019, China

ARTICLE INFO

Article history:
Received 28 August 2020
Received in revised form 17 December 2020
Accepted 21 December 2020
Available online 31 December 2020
Editor: N. Nagaosa

Keywords:
Heat conduction
Heat convection
Heat radiation
Theoretical thermotics
Transformation method
Effective medium theory
Fourier law
Thermal band theory
Phase transition
Thermal cloak
Thermal concentrator
Thermal rotator
Thermal transparency
Thermal illusion
Thermal camouflage
Thermal crystal
Daytime radiative cooling
Thermal rectification
Energy-free thermostat
Thermal chameleon
Temperature-dependent thermal conductivity
Nonlinear phenomenon
Thermal intelligence
Infrared detection
Complex thermotics
Modern thermodynamics

ABSTRACT

Classical thermodynamics often helps to passively describe macroscopic heat phenomena of natural systems, which means people almost cannot change the heat phenomena, but understand them according to the four thermodynamic laws. In contrast, thermal metamaterials, together with the governing theories, make it possible to actively manipulate macroscopic heat phenomena of artificial systems, which enables people to change the heat phenomena at will. Such metamaterials or metamaterial-based devices refer to those artificial structures that yield novel functions in controlling heat transfer. Since the concept of thermal cloak was proposed in 2008, this field has been developed rapidly with fruitful research results, which range from both theoretical models and experimental techniques in scientific research to practical applications in industry, such as radiative cooling and infrared camouflage. In this review, we comb through the research history of thermal metamaterials, and present novel functions and their associated theories in four areas. Such theories include both transformation theories and their extended theories, which are called theoretical thermotics for convenience. The four areas are classified according to the different ways of heat transfer, namely, heat conduction, heat conduction–convection, heat conduction–radiation, and heat conduction–convection–radiation. The corresponding experiments and applications are also introduced. At last, we provide our views on future opportunities and challenges in thermotics of metamaterials.

Contents

* Corresponding author.
E-mail address: jphuang@fudan.edu.cn (J. Huang).

https://doi.org/10.1016/j.physrep.2020.12.006
0370-1573/

1. Introduction

Heat energy, existing everywhere, has close relationship with human life, so it is of particular importance to control heat flux at will. Together with the rapid development of electromagnetic/optical metamaterials [1–7], thermal metamaterials [8] also emerged and became a powerful tool to manipulate heat energy, which started from the proposal of transformation thermotics [9,10], a thermal counterpart of transformation optics [4]. Generally speaking, metamaterials can be used to reveal novel physics and develop new applications because of their novel artificial structures. Up to now, a large number of metamaterials were designed and fabricated in the fields of microwaves [6], elastic waves [11,12], hydroscience [13], matter waves [14,15], acoustics [16–18], thermotics [9,10,19–23], and so on.

In order to systematically understand metamaterials, Wegener [24] and Kadic et al. [25] divided them into two categories: (I) one is metamaterials in optics/electromagnetism, namely, optical/electromagnetic metamaterials; (II) the other is metamaterials beyond optics/electromagnetism, say, acoustic metamaterials and thermal metamaterials (for controlling heat conduction, convection, and radiation). Clearly, (I) is for wave systems, and (II) is not only for wave systems, but also for diffusion systems. Since both waves and diffusion are two different crucial methods for transferring energy, a further classification [26] might be necessary as shown in Fig. 1.1. With this classification, according to Wegener [24] and Kadic et al. [25], wave systems are divided into "wave in optics or electromagnetics" and "wave beyond optics or electromagnetics". In contrast to wave systems, diffusion systems come to appear as a different branch. Incidentally, for wave systems, the characteristic length of the corresponding metamaterials is known to be the incident wavelength of various kinds of waves. Hence, according to the concept or definition of metamaterials, the geometry size of the functional unit of the metamaterials should be smaller or much smaller than the incident wavelength (characteristic length). Similarly, thermal metamaterials also have characteristic lengths [24,27], which should be larger or much larger than the functional unit: for controlling heat conduction, the characteristic length is the heat diffusion length [24],

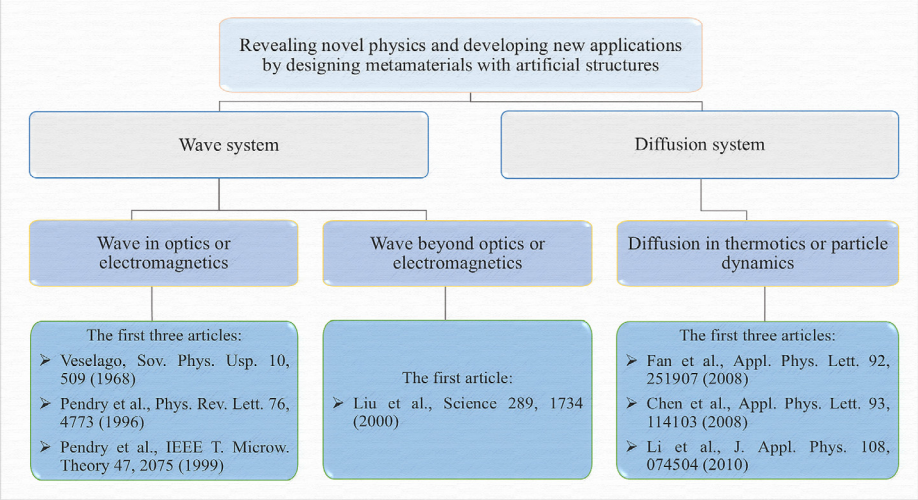

Fig. 1.1. Brief overview of the physics of metamaterials: two systems and three main branches [24–26]. In the third main branch ("Diffusion in thermotics or particle dynamics"), currently thermal metamaterial plays a dominant role.

which is a function of time; for controlling heat convection, the characteristic length is the time-dependent geometry length of matter or mass transfer; for controlling heat radiation, the characteristic length is the wavelength of radiated electromagnetic waves.

Now Fig. 1.1 enables us to briefly comb through the research history of the physics of metamaterials in a chronological order. First of all, Veselago proposed the concept of negative refractive index in 1968 [1], which cannot be found in naturally occurring materials. Almost 30 years later, during the visit at the Marconi Research Centre, Pendry realized that artificial microstructures can be an approach to such unusual electromagnetic properties and studied the metal wire arrays [2] and split rings structures [3]. As a result, the concept of negative refractive index started to receive extensive research interests. The two basic structures proposed by Pendry et al. opened a new gate for metamaterial physics. On that basis, Pendry et al. further proposed the theory of transformation optics [4], which has become a general method for controlling not only electromagnetic fields but also other physical fields, such as those in acoustics, thermotics, and mechanics. With experimental researches and many other follow-up studies [28–34], electromagnetic/optical metamaterials have become a mature research field.

Beyond electromagnetic waves which are mainly featured by transverse wave properties, Sheng and his coauthors revealed local resonance in sonic materials [35], which also have longitudinal wave properties. Their work paved a new way for sonic metamaterials, based on which people can explore negative refraction, Dirac materials, and topological physics in acoustics.

The great success of metamaterials in wave systems also ignited the research of metamaterials (including metamaterial devices) in diffusion systems, which were initially designed to control steady-state thermal conduction (diffusion) by establishing transformation thermotics [9,10,26]. Within the past decade, thermal metamaterials have been rapidly developed and applied in human daily life, say, radiative cooling [36,37]. Besides, thermal metamaterials are also important in the field of military infrared detection, because they can help objects to hide their own infrared signals on the basis of artificial structures with specific conductivity distributions. The so-called "hide" includes both the concealment of a true target [38,39] and the display of a false target [40,41], which has applications in misleading infrared detection. In the current literature, the former (or the latter) is called "camouflage" (or "illusion").

In what follows, we review thermal metamaterials in four areas, which are classified according to the different modes of heat transfer, namely, heat conduction, heat conduction–convection, heat conduction–radiation, and heat conduction–convection–radiation. In each area, we focus on both the transformation method and its extended methods (other methods), all of which are particularly developed to theoretically design and experimentally fabricate thermal metamaterials for controlling macroscopic heat transfer at will. For the sake of convenience, such methods are called theoretical thermotics as a whole [26]. The comparison between theoretical thermotics and traditional thermodynamics is shown in Table 1. Contrary to thermodynamics, theoretical thermotics enables people to actively control heat phenomena of artificial systems at will. For thermal metamaterials, Table 1 also suggests a complete research route from fundamental theories (science), to technological development (technology), and to industrial applications (industry). The route covers the following steps: establishing/developing theoretical thermotics → designing artificial systems/structures → achieving thermal metamaterials or metamaterial devices → actively controlling heat transfer and obtaining novel heat phenomena/properties → realizing applications.

For the convenience of reference, we make a preview of phenomena and devices involved in each chapter. In Chapter 2, we introduce several typical thermal conduction metamaterials including thermal cloaking, thermal concentrating,

Table 1
Thermodynamics versus theoretical thermotics. Here "passive description" means that people cannot change the heat phenomena of natural systems, but understand them according to the four thermodynamic laws. In contrast, "active control" means that people can change the heat phenomena at will, by designing artificial systems on the basis of transformation thermotics and their extended theories. Such theories also make theoretical thermotics distinctly differ from the existing heat transfer theory [42] (which is much more familiar to engineering thermophysicists than to physicists).
Source: Adapted from Ref. [27].

	Main purpose	Key systems	Theoretical framework
Thermodynamics	Passive description	Natural systems	The four laws of thermodynamics
Theoretical thermotics	Active control	Artificial systems	Transformation thermotics and extended theories

thermal rotating, and thermal camouflaging. Moreover, some novel thermal metamaterials are also involved, such as digital thermal metasurfaces, thermal chameleon-like metashells, energy-free thermostat devices, thermal dipoles, thermal crystals, phonon transport, and printed circuit boards containing various thermal metamaterials for heat dissipation of electronic devices. In Chapter 3, in addition to the typical thermal convection metamaterials, we also summarize the phenomena of thermal wave, zero-index cloak, thermal anti-parity-time symmetry, thermal convection–conduction crystal, negative thermal transport, and so on. Typical thermal radiation metamaterials and some developments in near-field thermal radiation can be found in Chapter 4. Chapter 5 presents (switchable) omnithermal metamaterials, radiative cooling, and restructurable metasurfaces, which is followed by conclusion and outlook in Chapter 6.

2. Controlling heat conduction

2.1. Transformation method

2.1.1. Thermal cloak

Inspired by transformation optics [4], Fan et al. [9] proposed the theory of transformation thermotics, with which they designed thermal cloaking and found apparently negative thermal conductivities. Nowadays thermal cloaking is featured by both zero temperature gradient in a central region and undistorted temperature distribution in the matrix outside the central region. So, such cloaking has applications in hiding or protecting objects from being detected or destroyed, see Fig. 2.1(a). Apparently negative thermal conductivities indicate that the direction of heat flux is from the region with low temperatures to that with high temperatures, which seems to violate the second law of thermodynamics. In fact, it is a local apparent effect which is still of physical feasibility.

Very soon Chen et al. [10] extended the theory of transformation thermotics from treating isotropic thermal conductivities of backgrounds to treating anisotropic ones. They revealed that as long as the anisotropic thermal conductivities are expressed in tensorial forms, the original transformation rule can still be applied. They also designed thermal cloaking which can work in the backgrounds with anisotropic thermal conductivities. Their work makes thermal cloaking more applicable under more complex conditions.

The above two works discussed steady cases of heat conduction, and neglected transient cases. To solve this problem, Guenneau et al. [20] extended the theory of transformation thermotics from steady cases to transient cases by taking time-changing parameter (here refers to temperature) into consideration. They revealed the transformation principle of density and heat capacity, yielding a good performance of transient thermal cloaking. Their work started to make thermal cloaking applicable in both steady cases and transient cases. In other words, a complete framework for manipulating thermal conduction was established, which promoted the development of thermal metamaterials.

So far, the exploration of thermal metamaterials was limited to theories, and no experiments were performed. To go further, Narayana et al. [21] performed the first experiment on thermal metamaterials. By applying multilayered structures based on the effective medium theory, they fabricated three devices with functions of cloaking, concentrating, and rotating. Multilayered structures provide the possibility of implementing anisotropic thermal conductivities. Sample structures, computer simulations, and experimental results are displayed in Fig. 2.2. Although their work considered only steady cases, it started the experimental exploration of thermal metamaterials. The field of thermal metamaterials started developing rapidly, and more thermal functions with different artificial structures became experimentally possible.

The experimental demonstration of thermal cloaking was also extended from steady cases to transient states soon. By additionally considering the time-changing temperature, Schittny et al. [22] designed thermal cloaking in transient cases. Multilayered structures were still applied to fabricate the device, and holes with different sizes were drilled in each layer to match the expected parameters. Their simulations and experiments indicated that thermal cloaking can be achieved in transient cases indeed. Their work enlightened the experimental explorations of thermal metamaterials in transient cases, and other thermal metamaterials beyond thermal cloaking can be similarly extended to transient cases.

These devices of thermal cloaking are almost perfect, and a feature is that the temperature gradient in the center is zero as mentioned above. Nevertheless, the feature is adverse in some specific cases. For example, let us see the object

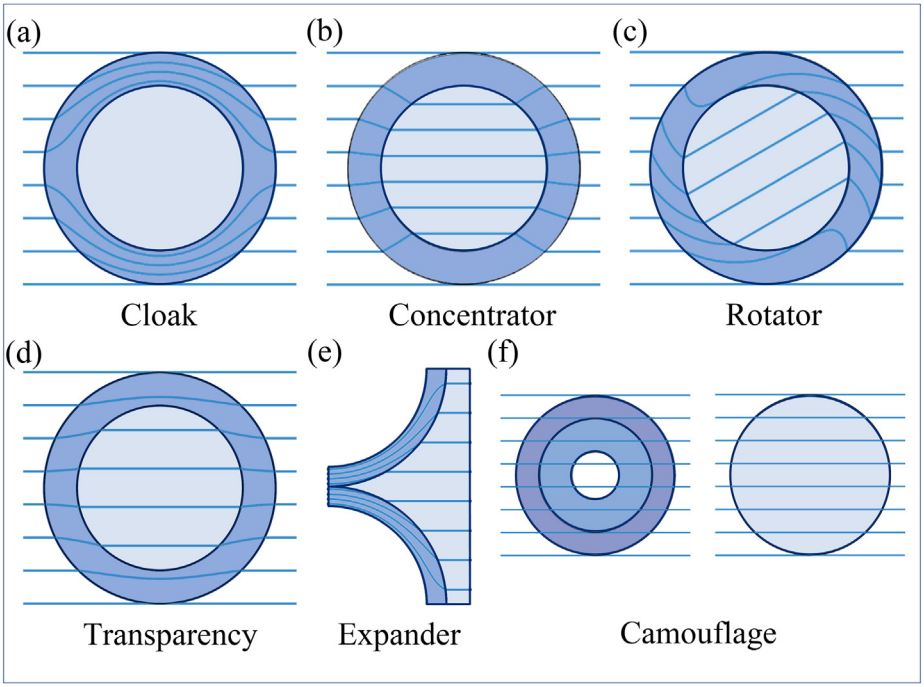

Fig. 2.1. Schematic graph showing the behavior of six representative thermal metamaterials or devices (made of thermal metamaterials). Solid lines denote the flow of heat.

as a sensor. In this case, although thermal cloaking can protect the sensor from being detected, the sensor in a cloak also cannot detect the local temperature distribution due to the zero temperature gradient inside. To solve this problem, Shen et al. [43] proposed a method to hide an object with thermal feeling, which was based on the theory of transformation thermotics. As a result, the object can not only keep thermally invisible, but also detect the local temperature distribution. Therefore, their work largely broadened the application scope of thermal cloaking.

So far, the discussion on the theory of transformation thermotics was limited to linear thermal conductivities (which indicate that thermal conductivities are temperature-independent). However, many natural materials are nonlinear (thermal conductivities are temperature-dependent), such as glasses and ceramic. Naturally, it becomes a problem whether the existing transformation thermotics can be applied to nonlinear cases. Li et al. [44] solved the problem by proposing the theory of temperature-dependent transformation thermotics. By taking nonlinear thermal conductivities into consideration, they designed switchable thermal cloaking and further fabricated a macroscopic thermal diode. In the experimental setup, shape-memory alloys were applied to achieve such a nonlinear thermal conductivity. And the composites of shape-memory alloys, copper and expanded-polystyrene result in the behavior of thermal diode indeed. Their work started the exploration of nonlinear thermotics and intelligent thermal metamaterials.

As is known, thermal cloaking can keep the central region at a constant temperature with fixed boundary conditions. However, this constant temperature may change its value if the boundary conditions are changed. This is not beneficial if one requires a thermostat. To solve this problem, Shen et al. [45] designed a thermostat with shape-memory alloys (acting as nonlinear materials). By applying two types of shape-memory alloys, the temperature of the central region can be maintained unchanged. Such a scheme requires no extra energy import, thus also called zero-energy-consumption thermostat. This device can help to reduce energy consumption.

Above, we have discussed thermal conduction at the macroscopic scale, which can be described by the Fourier law. In fact, this Fourier law is also valid at the microscale due to the same diffusive transport of heat as that at the macroscopic scale. Indeed, a microscopic thermal cloak was experimentally fabricated by focused ion irradiation [46,47]. However, thermal conduction at the nanoscale may have different mechanisms from that at the macroscopic scale or microscopic scale, due to the ballistic transport of heat. In other words, the traditional Fourier law cannot be directly utilized at the nanoscale. Therefore, the exploration of thermal metamaterials at the nanoscale becomes particularly important. Ye et al. [48] extended the exploration of thermal metamaterials to the nanoscale. They applied the method of molecular dynamics simulation and revealed a similar cloaking effect at the nanoscale. Owing to the microminiaturization of electronic devices, their work has practical applications in thermally protecting electronic devices from being destroyed by large heat flux.

Most studies on thermal cloaking are based on circular/spherical shapes. However, actual shapes can be more plentiful [9]. For example, to promote the development, Han et al. [49] designed thermal cloaking with noncircular

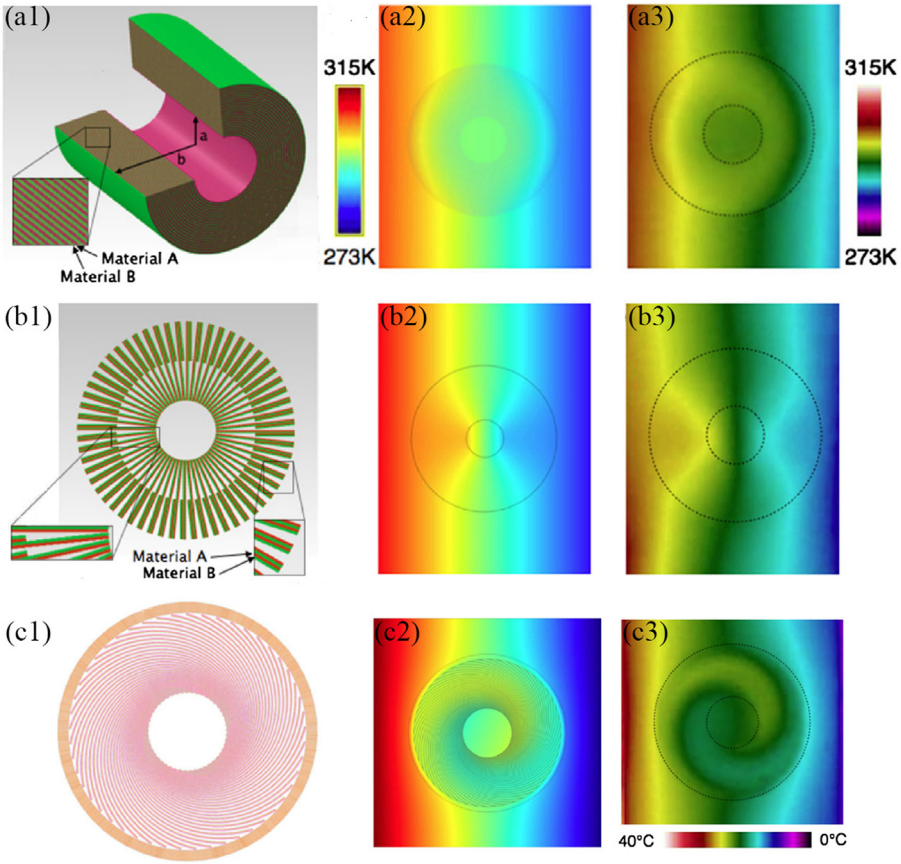

Fig. 2.2. (a1–a3) Thermal cloak. (b1–b3) Thermal concentrator. (c1–c3) Thermal rotator. The first, second, and third columns present the schematic diagrams, simulation results, experimental results, respectively.
Source: Figure reproduced with permission from Narayana et al. Phys. Rev. Lett., 108, 214303, 2012.

shapes; see Fig. 2.3. Fig. 2.3(a) presents the schematic diagrams of cloaked sensor, invisibility cloak, and super expander, whose practical structures are shown in Fig. 2.3(b). The thermal conductivity along y axis of the structure κ_y is plotted as a function of period L; see Fig. 2.3(c). Then, one can design devices according the shell size and background thermal conductivity according to Fig. 2.3(d).

2.1.2. Thermal concentrator

Beyond the function of thermal cloaking, thermal concentrating was also a research focus, see Fig. 2.1(b). Yu et al. [50] applied transformation thermotics to design thermal concentrating, and Guenneau et al. [20] extended the scheme to transient states. Thermal concentrating can enhance the local heat flux without distorting external thermal fields, which has practical applications in harvesting heat energy. Similar to thermal cloaking, multilayered structures were also applied to design thermal concentrating [21,51–54]. These thermal concentrating were not switchable. To promote practical applications, Li et al. [55] designed switchable thermal concentrating based on the temperature-dependent transformation thermotics. Their work provided intelligence into thermal concentrating, making the scheme more flexible.

With the proposal of more and more functions, researchers found that it is possible to design bifunctional devices. For this purpose, Li et al. [19] designed thermal cloaking and electrical cloaking on a single device based on the transformation theory. Their work opened the gate for bifunctional devices and had practical applications in device integration. From then on, bifunctional devices were proposed intensively. Ma et al. [56] experimentally demonstrated a device with functions of both thermal cloaking and electrical cloaking; see Figs. 2.4–2.5. Fig. 2.4(a–d) show the electrical cloaking results and Fig. 2.5(a–d) show the thermal cloaking results.

In addition, Moccia et al. [57] theoretically designed a device with functions of both thermal concentrating and electrical cloaking. Lan et al. [58] proposed a device with functions of both thermal concentrating and electrical concentrating. Stedman et al. [59] considered the coupling effect of heat and electricity (say, thermo-electric effect) to design cloaking. Shen et al. [60] fabricated a device with functions of both thermal cloaking and thermal concentrating (switching according to concrete temperatures).

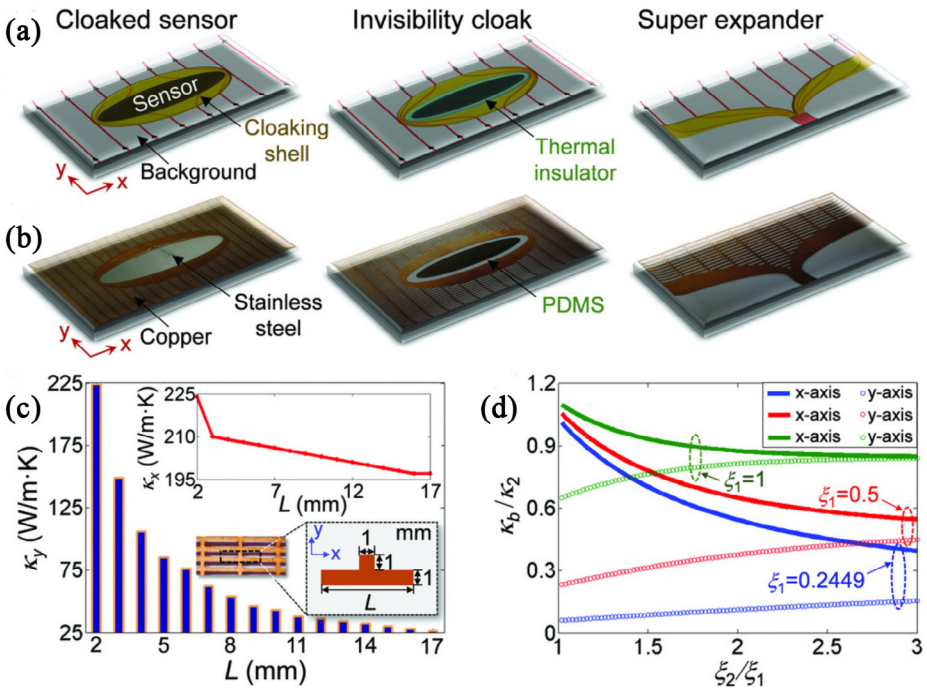

Fig. 2.3. (a) Schematic diagrams and (b) practical structures of sensor, cloak, and expander. (c) Thermal conductivity κ_y as a function of period L. (d) κ_b/κ_2 as a function of ξ_2/ξ_1.
Source: Figure reprinted with permission from Han et al. Adv. Mater., 26, 1731–1734, 2018.

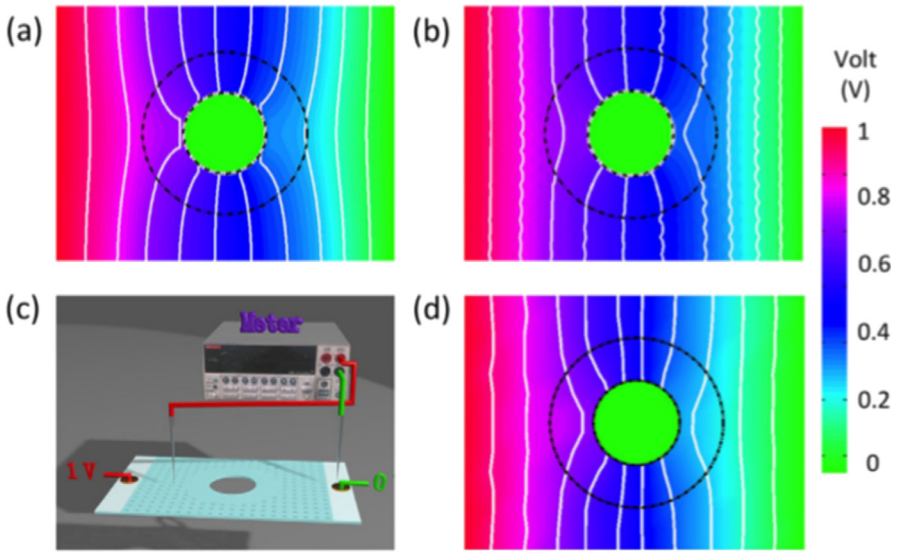

Fig. 2.4. Electrical cloaking. (a) Simulation result without a cloaking shell. (b) Simulation result with a cloaking shell. (c) Experimental set up. (d) Experimental result with a cloaking shell.
Source: Figure reprinted with permission from Ma et al. Phys. Rev. Lett., 113, 205501, 2014.

2.1.3. Thermal rotator

Thermal rotating is also a representative function of thermal metamaterials, see Fig. 2.1(c). Based on the multilayered structures, Narayana et al. [21] fabricated the first device with thermal rotating, which can control the local direction of heat flux. Their work considered only steady cases. To go further, Guenneau et al. [61] designed thermal rotating in

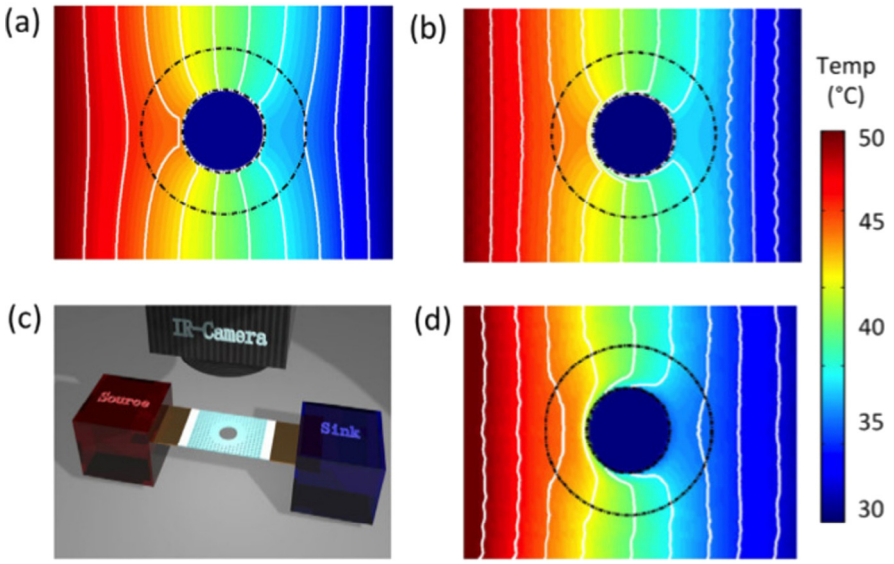

Fig. 2.5. Thermal cloaking. (a) Simulation result without a cloaking shell. (b) Simulation result with a cloaking shell. (c) Experimental set up. (d) Experimental result with a cloaking shell.
Source: Figure reprinted with permission from Ma et al. Phys. Rev. Lett., 113, 205501, 2014.

transient cases based on transformation thermotics. These results are expected to have more applications, such as realizing waste-heat recovery and designing apparently negative thermal conductivities.

Transformation thermotics has achieved great success till now, and the metamaterials based on it have also yielded fruitful results. However, the intelligence of materials is more concerned nowadays, so the lack of intelligence is a sore point for transformation-thermotics-based metamaterials. Their key parameters, such as thermal conductivities, are directly related to the background materials, which means that if the background changes, the designed metamaterials will fail. This shortcoming greatly limits the practical application because the well-designed meta-device can only work in a specific environment, but it is obvious that the environment cannot remain unchanged in real life.

To overcome this problem, Yang et al. proposed a mechanism to improve the intelligence of transformation thermal metamaterials [62]. They used transformation-invariant materials to design thermal metamaterials. Transformation-invariant materials are also called highly anisotropic materials which have aroused great interest in acoustics and electromagnetism. This kind of material can respond adaptively to the changes in the environment because of its extremely anisotropic parameters. Therefore, it is an excellent choice to design intelligent thermal metamaterials based on transformation-invariant materials. Then they applied coordinate transformations to this kind of material, and obtained corresponding thermal meta-devices. These meta-devices retain the property of transformation-invariant materials, which can have adaptive responses to environmental changes, just like a chameleon. Therefore, they call it chameleon-like metamaterial. For application, they took thermal rotators as an example to demonstrate the intelligence of designed metamaterials. To realize highly anisotropic parameters, they used air and copper as transformation-invariant materials, and fabricated a multilayer composite structure to realize a thermal rotator. Their experiment results are consistent with the simulation results, which verifies their theory and the feasibility of chameleon-like thermal metamaterials.

2.1.4. Thermal camouflage

As a more general concept, thermal camouflaging (Fig. 2.1(f)) also aroused attention due to its broad application in the fields of industry and military. Chen et al. [63] theoretically designed a camouflage device based on transformation thermotics. Such a device can thermally disguise an object into another one. In addition, Hu et al. [64] experimentally fabricated a camouflage device which can make one heat source look like four heat sources; see Fig. 2.6. They fabricated three devices to validate their theory. These devices have applications in future infrared detection.

2.2. Other methods

2.2.1. Macroscopic theory based on conduction equation

Transformation thermotics usually requests anisotropy, inhomogeneity, and singularity of thermal conductivity, which brings difficulties to manufacturing. Fortunately, this problem was soon removed by two groups almost at the same time [65,66]. Inspired by the previous work of shielding static magnetic fields with scattering cancellation method [67],

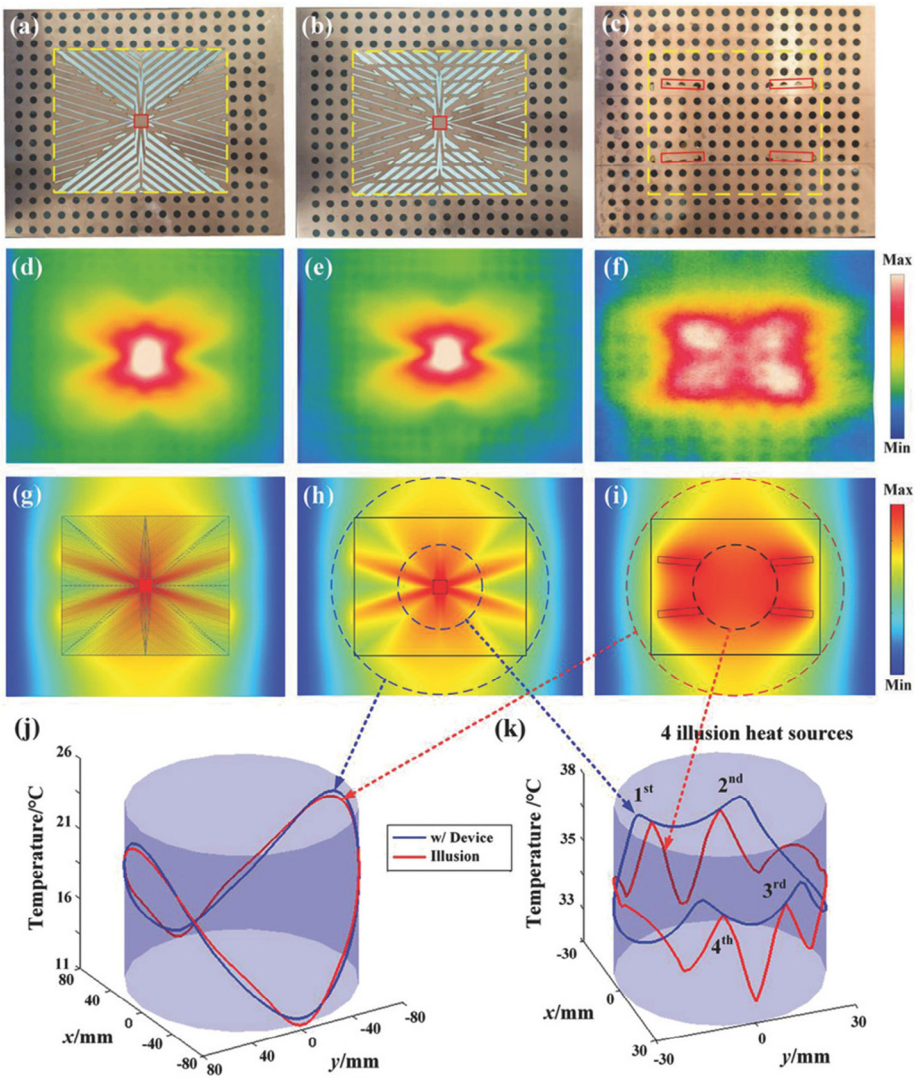

Fig. 2.6. Experimental result of thermal camouflaging. (a–c) Experimental samples. (d–f) Experimental results corresponding to (a–c). (g–i) Simulation results corresponding to (d–f). (j) Temperature curves along the large dashed circle in (h) and (i). (k) Temperature curves along the small dashed circle in (h) and (i).
Source: Figure reprinted with permission from Hu et al. Adv. Mater., 30, 1707237, 2018.

they solved this trouble by solving the conduction equation directly. Accordingly, a bilayer structure was theoretically proposed and experimentally verified for cloaking heat flux with isotropic materials, instead of extreme parameters. Starting from the steady-state Laplace equation, the temperature field of a bilayer structure located at a homogeneous background medium could be analytically obtained. After setting the thermal conductivity of inner layer as zero (e.g., approximately achieved by air), both the desired thermal conductivity and radius of the outer shell can be determined accurately. With appropriate selection of materials and geometric dimensions, the two-dimensional [65] and three-dimensional [66] experimental demonstrations were executed. Simulation and experimental results of the two-dimensional bilayer thermal cloak are shown in Fig. 2.7 and the fabrication process of the three-dimensional bilayer thermal cloak is shown in Fig. 2.8. This method overcame the weakness of transformation thermotics, offering a more convenient scheme for thermal cloaking. Incidentally, inspired by Ref. [68], some researchers [69] proposed an exact approach to achieving an effectively infinite thermal conductivity with constant-temperature boundary conditions, which can be realized by an external thermostat. Since the effectively infinite thermal conductivity corresponds to zero refractive indexes in photonics, they theoretically designed and experimentally demonstrated zero-index thermal cloaks working in highly conductive backgrounds with simple structures [69].

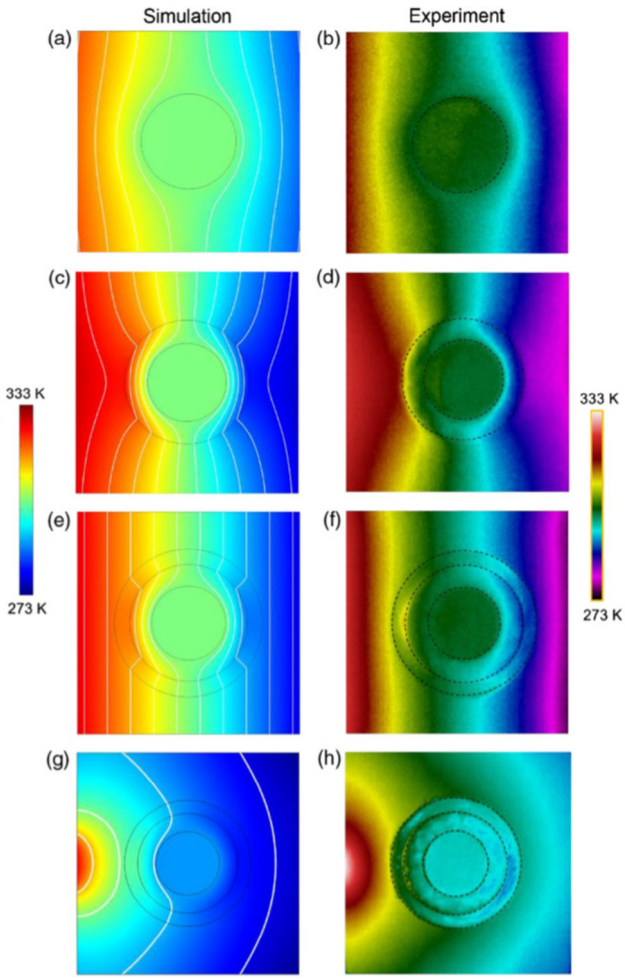

Fig. 2.7. Simulation and experimental results of a two-dimensional bilayer thermal cloak. (a–d) Results without a bilayer cloak. (e–f) Results with a bilayer cloak. (g–h) Results with a bilayer cloak in nonuniform field.
Source: Figure reprinted with permission from Han et al. Phys. Rev. Lett., 112, 054302, 2014.

Besides thermal cloaking, the devices of thermal illusion and camouflage were also developed on the basis of the direct solution of governing equations. These devices are particularly interesting and have direct applications in industrial or military domains. Similar to bilayer cloaking, the illusion and camouflage phenomena were achieved with natural materials. Han et al. extended the bilayer structure with an additionally pre-designed pattern outside the shell [65]. Then, the original object hidden in the center was undetectable, and another signature (caused by the new pattern outside the shell) emerged instead, as if only the new pattern was located in the background. The illusion effects were omnidirectional and time-independent, which were verified by experiments. This result makes it feasible to fabricate illusion devices with subsistent natural materials. However, the proposed scheme has some limitations. For example, it works imperfectly under transient conditions, where the central regions are distinct from the sole illusion patterns through out-of-plane detection. This is because the inner layer is thermally insulated. The heat flux hardly runs into the interior. Yang et al. improved this illusion device by taking the time-dependent conduction equation into consideration [70]. In their design, the inner layer does not require a near-zero thermal conductivity. Thus, the central temperature distribution could match the sole illusion, as if no objects existed inside the bilayer cloaks. Experimental demonstrations behaved well under time-dependent conditions. The camouflaging effects were also generalized to a multi-physical-field sensor [71], which was invisible under multiple physical fields. They checked the conduction equations of heat and direct current together, and obtained the condition of simultaneous invisibility with a single layer. By elaborately selecting natural materials for matching the ratio of thermal and electric conductivities, this kind of sensor was easy to fabricate, as demonstrated in their experiments. In this case, impedance (or thermal conductivity) matching is an indispensable condition. Recently, an anisotropic monolayer scheme was also designed and fabricated to make thermal sensors accurate and invisible [72]. The above discussions are mostly based on two-dimensional models. Beyond the aforementioned bilayer schemes, Wang

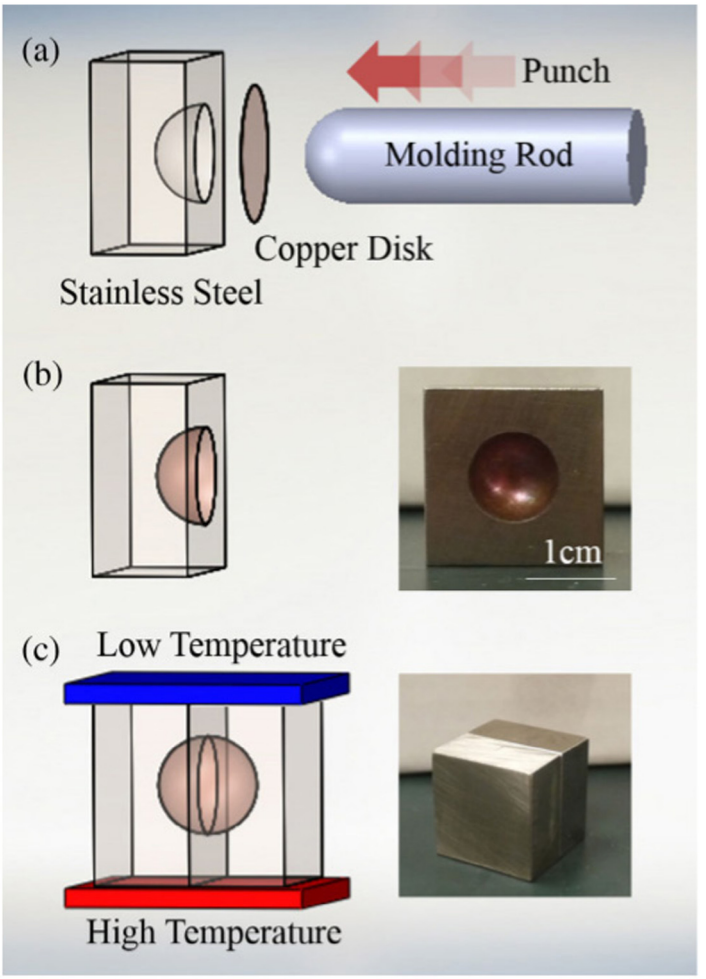

Fig. 2.8. Experimental set up of a three-dimensional bilayer thermal cloak. (a) Manufacturing method of half of the three-dimensional thermal cloak. (b) Schematic diagram and picture of half of the three-dimensional thermal cloak. (c) Schematic diagram and picture of full three-dimensional thermal cloak.
Source: Figure reprinted with permission from Xu et al. Phys. Rev. Lett., 112, 054301, 2014.

et al. designed different devices for illusion [54] or camouflage [73] with other structures. They adopted many-particle composite structure for illusion and graded layer structure for camouflage, whose effective thermal conductivities were in accordance with the predictions of the classical Bruggeman theory and the Maxwell–Garnett theory, respectively. The reported results gave prototypes for combining metamaterial design with the known effective medium approximations, leading to numerous subsequent studies on designing novel thermal devices with composite media. More recently, Peng et al. [41] proposed the concept of three-dimensional illusion with separated thermal illusions.

Thermal transparency is another novel phenomenon achieved by solving exact solutions of conduction equations. Different from thermal cloaking, transparency allows heat flux to run into the center of the shells, allowing the feeling of external thermal environments, see Fig. 2.1(d). So bilayer structures can be extended to multilayer ones without the need of zero thermal conductivities. He et al. [74] transferred the effective parameter conclusions from direct-current fields to thermal fields, and examined spherical and spheroidal shapes for thermal transparency. Owing to the form analogy between direct-current and heat-conduction equations, the effective thermal conductivities of the above structures are easy to be obtained. With the parameter matching between structures and backgrounds, the expected effects were obtained indeed. Soon after, the proposed transparency scheme was verified by experiments [75]. Zeng et al. [75] demonstrated that such transparency device could be used to measure the time evolution of heat sources without the disturbance of surroundings.

Based on the effective medium approximation, the structures with particles embedded in media were carefully investigated beyond core–shell structures. For example, Yang et al. [76] investigated the case that a single elliptical particle is located at the center of background, and designed a full control of thermal signature in different directions. Then, it

was generalized to many-particle systems. Random [77] and periodic [78,79] distributions of particles were theoretically studied and experimentally designed for transparency, which echoed with the Bruggeman theory and the Maxwell–Garnett theory. This kind of device can effectively reduce the heat-stress concentration caused by heat-flux concentration in some critical parts of devices. Besides, the advantage of out-of-plane invisibility makes it possess a high survival ability. The remaining challenges may be the lack of theory for treating the cases that shapes and thermal conductivities are anisotropic simultaneously, which is more common in applications.

The one-dimensional heat conduction equation in homogeneous materials is formally concise. In 2018, Shang et al. proposed a digital thermal metasurface with the one-dimensional heat transfer along z axis [80] to demonstrate a thermal imitator. They designed an ultrathin structure with tiny cells arrayed periodically. The thermal conductivity of each cell was specially designed with different composite ratios. So this kind of metasurface showed specific temperature distribution with out-of-plane observation, which could, in principle, be used for mimicking thermal signatures of arbitrary objects. In experiments, they fabricated a human pattern with this metasurface, and observed the target infrared signature; see Fig. 2.9. This method can be applied in remote infrared camouflage or illusion, expanding its functionality from in-plane observation to out-of-plane observation. Moreover, as the scheme does not request specific materials, it is easy to fabricate different kinds of samples. Future works are required to adapt to complex environments, or to adjust feature patterns for varying external conditions.

Core–shell structures have attracted various research interests due to their symmetries associated with parameters and geometries. So this is an extremely ideal platform for tailoring novel thermal functionality, which has been studied completely in electromagnetism. As the form-similarity of electrostatic fields and steady temperature fields, the pre-existing technologies can be readily transferred to control the flow of heat. With the elaborate design of anisotropic parameters of the shells, the thermal properties of a core can be extended to the whole cylinder or sphere. As a result, thermal golden touch [81], heat flow rotation [82], and chameleon-like metashells [62,83] were successively implemented. Then, one can take the chameleon-like metashells as an example to expound the manipulation of core–shell structures.

Chameleon-like metashells can be defined as a kind of intelligent thermal metamaterials. Different from the previous "active" schemes [44,45,60,84] to fabricate intelligent metamaterials which need to consider environmental effects in advance, here Xu et al. adopted the "passive" method without the pre-knowledge of environments. The effective thermal conductivities of the chameleon-like metashells can adaptively change with objects in the vicinity, just like chameleons whose colors can change with nearby objects. Nature creatures have helped scientific development from the aspects of phenomena and/or mechanisms, such as structure colors [85,86], adaptive camouflage [87,88], radiation cooling [36,89], and so on. To some extent, such idea is inspired by nature creatures. The scheme can be validated by theory, simulation, and experiment.

Chameleon-like thermal metashells can change their thermal conductivities adaptively. Considering a two-dimensional system; see Fig. 1(a) of Ref. [83]. The metashell (Region II) splits the system into three regions. The tensorial conductivities are $\tilde{\kappa}_1$, $\tilde{\kappa}_2$, and $\tilde{\kappa}_3$ corresponding to Regions I, II, and III, respectively. Xu et al. supposed the object and background are isotropic, and the metashell is anisotropic. All the tensors in their work are expressed in cylindrical coordinates $(r,\ \theta)$ unless otherwise indicated. Then one can obtain $\tilde{\kappa}_1 = \kappa_1\tilde{I}_2,\ \tilde{\kappa}_3 = \kappa_3\tilde{I}_2$, and $\tilde{\kappa}_2 = \mathrm{diag}\,(\kappa_{rr},\ \kappa_{\theta\theta})$ where $\tilde{I}_2$ is the second-order identity matrix.

To derive the effective thermal conductivity of the object and metashell, consider the dominate equation of heat conduction,

$$\nabla\cdot(-\tilde{\kappa}\nabla T) = 0, \tag{2.1}$$

where $\tilde{\kappa}$ is tensorial thermal conductivity and T is temperature.

Then, Eq. (2.1) for Region II in cylindrical coordinates $(r,\ \theta)$ is given by

$$\frac{1}{r}\frac{\partial}{\partial r}\left(r\kappa_{rr}\frac{\partial T_2}{\partial r}\right) + \frac{1}{r}\frac{\partial}{\partial\theta}\left(\kappa_{\theta\theta}\frac{\partial T_2}{r\partial\theta}\right) = 0, \tag{2.2}$$

where T_2 is the temperature in Region II. Analogously, T_1 and T_3 are defined for Region I and Region III.

Then, calculating the general solution of Eq. (2.2) as

$$T_2 = A_0 + B_0\ln r + \sum_{i=1}^{\infty}\left[A_i\sin(i\theta) + B_i\cos(i\theta)\right]r^{im_1} + \sum_{j=1}^{\infty}\left[C_j\sin(j\theta) + D_j\cos(j\theta)\right]r^{jm_2}, \tag{2.3}$$

where $m_{1,2} = \pm\sqrt{\kappa_{\theta\theta}/\kappa_{rr}}$. T_1 and T_3 can also be determined by the right side of Eq. (2.3) with $m_{1,2} = \pm 1$. The coefficients in T_1, T_2 and T_3 can be obtained by the following boundary conditions,

$$\begin{cases} T_1 < \infty, \\ T_1(R_1) = T_2(R_1), \\ T_2(R_2) = T_3(R_2), \\ (-\kappa_1\partial T_1/\partial r)_{R_1} = (-\kappa_{rr}\partial T_2/\partial r)_{R_1}, \\ (-\kappa_{rr}\partial T_2/\partial r)_{R_2} = (-\kappa_3\partial T_3/\partial r)_{R_2}, \\ \nabla T_3\,(r\to\infty) = \nabla T_0, \end{cases} \tag{2.4}$$

where ∇T_0 represents external linear temperature gradient.

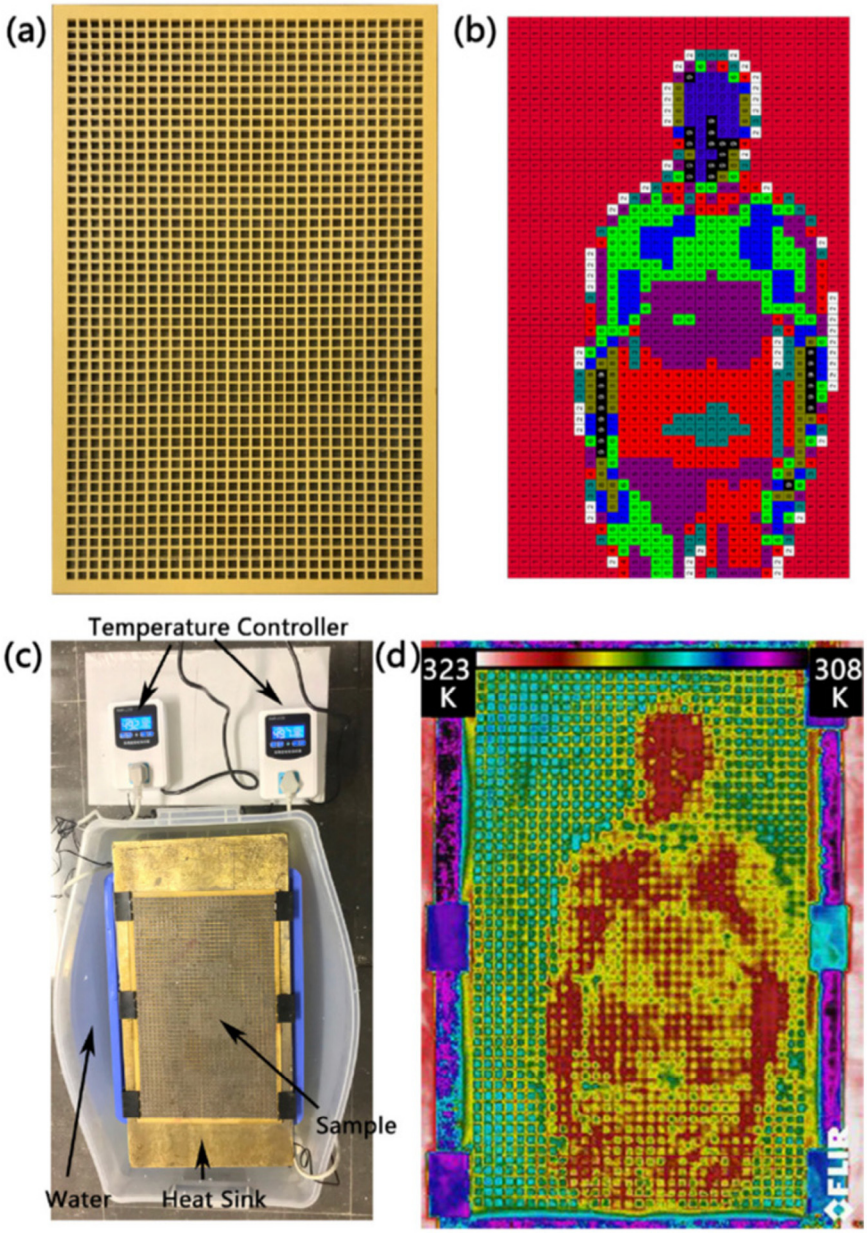

Fig. 2.9. Experimental set up of the digital thermal metasurface. (a) Schematic diagram of the sample. (b) The sample with corresponding thermal conductivities. (c) Experimental set up. (d) The temperature distribution of (a).
Source: Adapted from Ref. [80].

Consider the symmetry of boundary conditions, and only keep several terms of Eq. (2.3) to calculate T_1, T_2, and T_3. Then,

$$T_1 = A_0 + B_{11} r \cos\theta, \tag{2.5}$$

$$T_2 = A_0 + B_{12} r^{m_1} \cos\theta + D_{12} r^{m_2} \cos\theta, \tag{2.6}$$

$$T_3 = A_0 + B_{13} r \cos\theta + D_{13} r^{-1} \cos\theta. \tag{2.7}$$

Here A_0 represents the temperature at $\theta = \pm\pi/2$.

With Eqs. (2.5)–(2.7), Eq. (2.4) can then be simplified as

$$\begin{cases} B_{11}R_1 = B_{12}R_1^{m_1} + D_{12}R_1^{m_2}, \\ B_{12}R_2^{m_1} + D_{12}R_2^{m_2} = B_{13}R_2 + D_{13}R_2^{-1}, \\ \kappa_1 B_{11} = \kappa_{rr}\left(m_1 B_{12}R_1^{m_1-1} + m_2 D_{12}R_1^{m_2-1}\right), \\ \kappa_{rr}\left(m_1 B_{12}R_2^{m_1-1} + m_2 D_{12}R_2^{m_2-1}\right) = \kappa_3\left(B_{13} - D_{13}R_2^{-2}\right), \\ B_{13} = |\nabla T_0|, \end{cases} \tag{2.8}$$

The solution of Eq. (2.8) yields

$$\begin{cases} B_{11} = \frac{-4R_1^{m_1-1}R_2^{m_1+1}m_1\kappa_{rr}\kappa_3|\nabla T_0|}{R_1^{2m_1}(-\kappa_1+m_1\kappa_{rr})(m_1\kappa_{rr}-\kappa_3)-R_2^{2m_1}(\kappa_1+m_1\kappa_{rr})(m_1\kappa_{rr}+\kappa_3)}, \\ B_{12} = \frac{2(\kappa_1+m_1\kappa_{rr})R_2^{m_1+1}\kappa_3|\nabla T_0|}{R_1^{2m_1}(\kappa_1-m_1\kappa_{rr})(m_1\kappa_{rr}-\kappa_3)+R_2^{2m_1}(\kappa_1+m_1\kappa_{rr})(m_1\kappa_{rr}+\kappa_3)}, \\ D_{12} = \frac{-2(\kappa_1-m_1\kappa_{rr})R_1^{2m_1}R_2^{m_1+1}\kappa_3|\nabla T_0|}{R_1^{2m_1}(\kappa_1-m_1\kappa_{rr})(m_1\kappa_{rr}-\kappa_3)+R_2^{2m_1}(\kappa_1+m_1\kappa_{rr})(m_1\kappa_{rr}+\kappa_3)}, \\ B_{13} = |\nabla T_0|, \\ D_{13} = \frac{R_1^{2m_1}(-\kappa_1+m_1\kappa_{rr})(m_1\kappa_{rr}+\kappa_3)-R_2^{2m_1}(\kappa_1+m_1\kappa_{rr})(m_1\kappa_{rr}-\kappa_3)}{R_1^{2m_1}(\kappa_1-m_1\kappa_{rr})(m_1\kappa_{rr}-\kappa_3)+R_2^{2m_1}(\kappa_1+m_1\kappa_{rr})(m_1\kappa_{rr}+\kappa_3)}R_2^2|\nabla T_0|, \end{cases} \tag{2.9}$$

where $m_2 = -m_1$.

Finally, D_{13} is set to be zero for ensuring the thermal field of the background to be linear. Then, the value of κ_3 is exactly the overall thermal conductivity of Region I+II (denoted by κ_e),

$$\kappa_e = m_1\kappa_{rr}\frac{\kappa_1 + m_1\kappa_{rr} + (\kappa_1 - m_1\kappa_{rr})\left(\sqrt{p}\right)^{2m_1}}{\kappa_1 + m_1\kappa_{rr} - (\kappa_1 - m_1\kappa_{rr})\left(\sqrt{p}\right)^{2m_1}}, \tag{2.10}$$

where $m_1 = \sqrt{\kappa_{\theta\theta}/\kappa_{rr}}$, and $p = (R_1/R_2)^2$ is the area fraction.

The limit of κ_e can be calculated when $\kappa_{\theta\theta}/\kappa_{rr}$ goes to 0,

$$\kappa_e = \kappa_{rr}\frac{\kappa_1 - \kappa_{\theta\theta}\ln\sqrt{p}}{\kappa_{rr} - \kappa_1\ln\sqrt{p}}. \tag{2.11}$$

Eq. (2.11) help us find out the requirement of chameleon-like metashells. The chameleon-like metashell can change its thermal conductivity with nearby objects (Region I),

$$\kappa_2 = \kappa_1, \tag{2.12}$$

where κ_2 is the effective scalar thermal conductivity of chameleon-like metashell (Region II). Since the thermal conductivity of Region I or II is κ_1, that the effective thermal conductivity κ_e of Region I+II has the only possibility to be

$$\kappa_e = \kappa_1. \tag{2.13}$$

Comparing Eq. (2.12) with Eq. (2.11), the requirement of the metashell can be derived as

$$\kappa_{\theta\theta} = 0^+ \text{ and } \kappa_{rr} \gg \kappa_1, \tag{2.14}$$

for $\kappa_{\theta\theta}/\kappa_{rr} \to 0$. Clearly, Eq. (2.14) makes Eq. (2.11) satisfy the requirement of Eq. (2.13). Here $\kappa_{\theta\theta} = 0^+$ is a physical condition, which can be realized by materials with low thermal conductivities, such as air (with thermal conductivity 0.026 W m^{-1} K^{-1}). As numerically demonstrated in Fig. 1(b) of Ref. [83], a larger κ_{rr} could lead to a better chameleon-like behavior incidentally.

Then Xu et al. performed finite-element simulations to validate the theory. There are three regions in Fig. 2.10(a–f), namely, chameleon-like metashells, normal shells, and reference shells, which are respectively located in Region II of Fig. 2.10(a) and (d), (b) and (e), and (c) and (f). For the convenience of comparison, Xu et al. set the background (Region III) to have the same thermal conductivity as the corresponding object (Region I). Therefore, one can just compare the temperature profiles in the background (Region III) corresponding to the chameleon-like metashell and the reference shell to check whether the thermal conductivity of the metashell (Region II) changes with the inside object (Region I). If the temperature profiles are the same, the proposed chameleon-like metashell does work as expected.

Chameleonlike metashell yields an object can change its thermal conductivity corresponding to the object adaptively, which results in the same temperature profile in background as the reference shell; see Fig. 2.10(a) and (c). However, the normal shell distorts the background isotherms because of its different thermal conductivity; see Fig. 2.10(b). Further, Xu et al. changed the thermal conductivity of the object, and kept the metashell unchanged; see Fig. 2.10(d). As a result, the thermal conductivity of the chameleon-like metashell also changes adaptively, which results in the same background temperature profile as that corresponding to the reference shell; see Fig. 2.10(f). In this case, the normal shell cannot

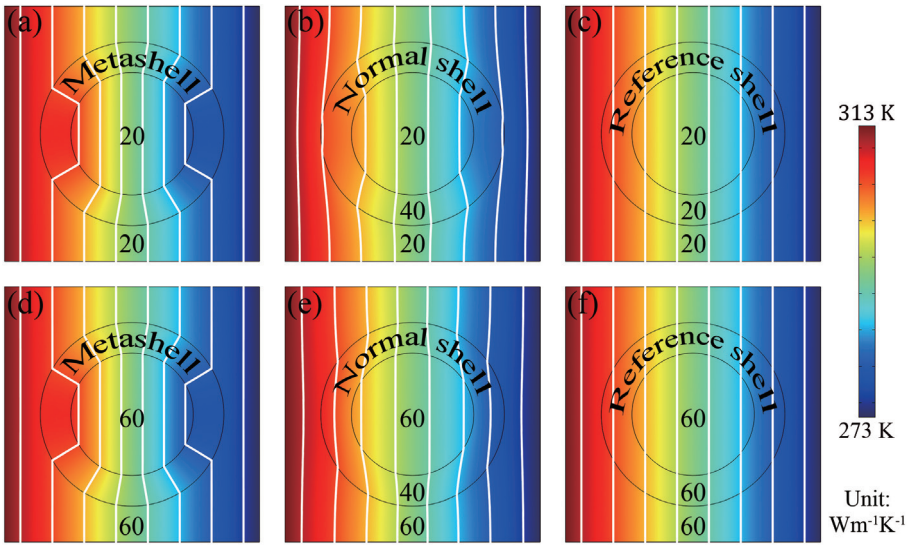

Fig. 2.10. Finite-element simulations of chameleon-like thermal metashells. The thermal conductivities of (a) and (d) chameleon-like metashell, and (b) and (e) normal shell are diag (4000, 0) and 40 (W m^{-1} K^{-1}), respectively. The thermal conductivities of the object (Region I) and background (Region III) are set to be the same, which are (a)–(c) 20 and (d)–(f) 60 (W m^{-1} K^{-1}). The thermal conductivities of reference shells in (c) and (f) are the same as those of corresponding objects. The simulation box in (a)–(f) is 20 × 20 (cm^2), $R_1 = 4.8$ (cm), and $R_2 = 7.2$ (cm). White lines represent isotherms.
Source: Adapted from Ref. [83].

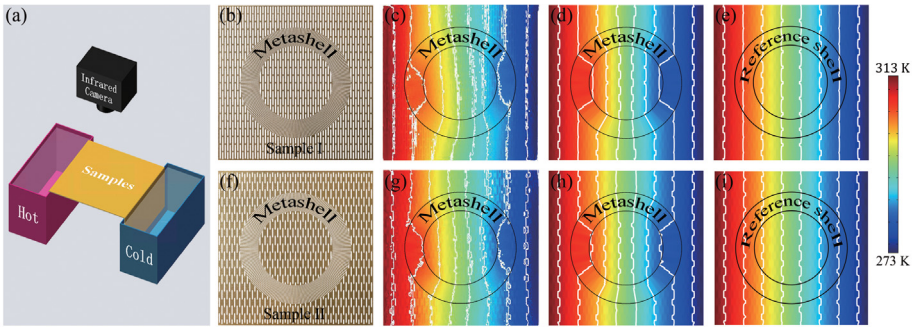

Fig. 2.11. Experimental results of chameleon-like thermal metashells. (a) Experimental setup; (b) and (f) Photos of two samples. The measured and simulation results of (b) [or (f)] are shown in (c) and (g) [or (d) and (h)], respectively. (e) and (i) Simulation results of the pure background as adopted in (b) and (f). The thermal conductivities of the copper and air are 400 and 0.026 (W m^{-1} K^{-1}), respectively. These parameters cause the tensorial thermal conductivity of the chameleon-like metashell in (b) and (f) to be diag (264.68, 0.08) (W m^{-1} K^{-1}), and the thermal conductivities of the object [or background] to be 20 (W m^{-1} K^{-1}) for (b) and 60 (W m^{-1} K^{-1}) for (f). The sample sizes in (b) and (f) are the same as those for Fig. 2.10(a).
Source: Adapted from Ref. [83].

change; see Fig. 2.10(e). The parameters of the chameleon-like metashell are designed according to Eq. (2.14), and the performance of Fig. 2.10(a) and (d) echoes with the red line in Fig. 1(b) of Ref. [83].

Xu et al. also set up the measuring device shown in Fig. 2.11(a) to validate the theory and simulations. They fabricated two experimental samples [Fig. 2.11(b) and (f)] corresponding to Fig. 2.10(a) and (d). The chameleon-like metashell in Fig. 2.10(a) and (d) is very curious material with very ideal parameters, but Xu et al. used approximate parameters to conduct experiments and the results are not affected. They fabricated the two samples by laser cutting, and measured them by the apparatus which was shown in Fig. 2.11(a). The corresponding measured results are shown in Fig. 2.11(c) and (g), proving that the thermal conductivity of chameleon-like metashell changes with different objects indeed. Xu et al. also performed simulations based on the two samples to remove the effects of convection and radiation; see Fig. 2.11(d) and (h). As references, Fig. 2.11(e) and (i) show the simulation results of the pure background with drilled air holes whose sizes are the same as the background in Fig. 2.11(b) and (f). Both simulations [Fig. 2.10(a) and (d), and Fig. 2.11(d) and (h)] and experiments [Fig. 2.11(c) and (g)] can validate the feasibility of the chameleon-like metashell.

Finally, Xu et al. extended the chameleon-like metashell from uniform/isotropic/circular to nonuniform/anisotropic/complex; see Fig. 2.12. Chameleonlike metashells, normal shells, and reference shells can be found in Fig. 2.12(a), (d),

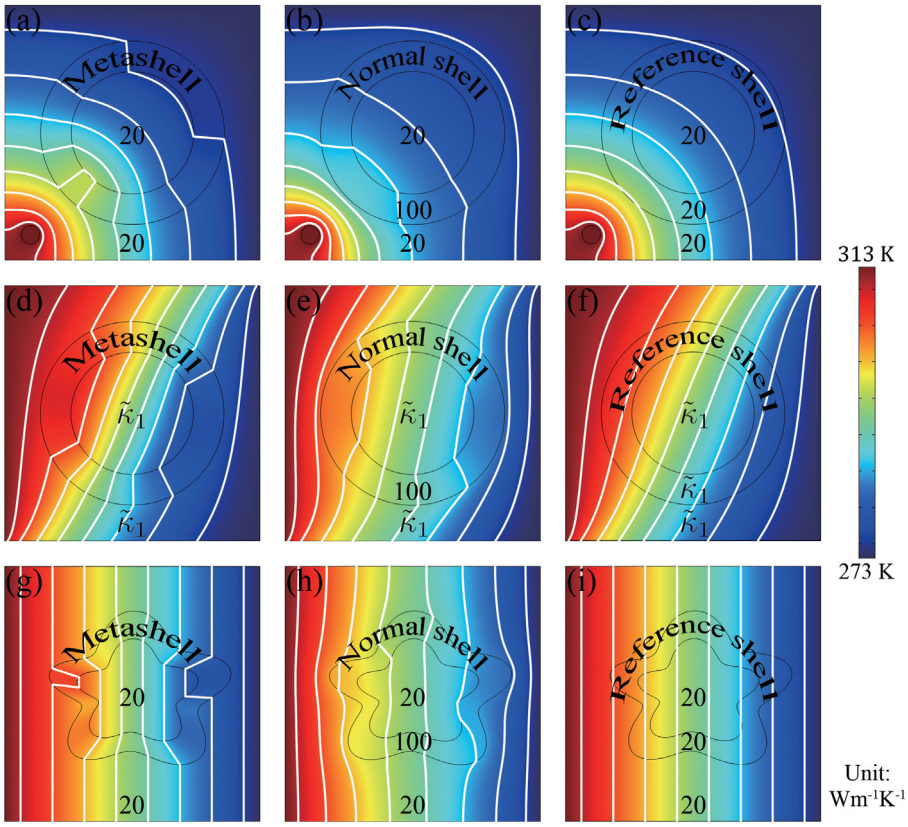

Fig. 2.12. Finite-element simulations of extended chameleon-like thermal metashells: (a)–(c) non-uniform fields generated by point heat sources; (d)–(f) anisotropic objects; (g)–(i) non-circular shapes. The thermal conductivities of object/background are (a)–(c) and (g)–(i) 20 (W m^{-1} K^{-1}), and (d)–(f) [(30, 20), (20, 30)] (W m^{-1} K^{-1}) (tensorial form in Cartesian coordinates). The metashell in (a), (d), and (g) is the same as that in Fig. 2.10(a) and (d), namely, diag (4000, 0) (W m^{-1} K^{-1}). The thermal conductivity of the normal shell is 100 (W m^{-1} K^{-1}). The thermal conductivity of the reference shell is the same as that of the corresponding object, namely 20 (W m^{-1} K^{-1}) for (c) and (i), and [(30, 20), (20, 30)] (W m^{-1} K^{-1}) for (f). Other parameters are same as those for Fig. 2.10(a).
Source: Adapted from Ref. [83].

and (g); (b), (e), and (h); and (c), (f), and (i), respectively. Chameleonlike metashell can adaptively change its thermal conductivity corresponding to the object when it reaches an object with non-uniform fields [Fig. 2.12(a)], which results in the same temperature profile in the background (Region III) as the reference shell [Fig. 2.12(c)]. However, because of the different thermal conductivity, the normal shell distorts the background isotherms [Fig. 2.12(b)] significantly. Similarly, when the chameleon-like metashell reaches an object with anisotropic parameters [Fig. 2.12(d)], it can adaptively change its thermal conductivity corresponding to the anisotropic object, which results in the same temperature profile in background (Region III) as the reference shell [Fig. 2.12(f)]. However, the normal shell also distorts the background isotherms [Fig. 2.12(e)]. Then Xu et al. arbitrarily changed the shape of the chameleon-like metashell while without changing the other parameters to check whether it still works. The ability of the chameleon-like shell is demonstrated by the same temperature profile in background (Region III) between Fig. 2.12(g) and (i). Again, the normal shell distorts the background isotherms [Fig. 2.12(h)]. These results indicate that chameleon-like metashells are applicable under different conditions.

Chameleonlike metashells in transient regimes are also promising, and good results can be expected in the light of the pioneering results on transient regimes [20,22,70,90].

These series of research provide a useful tool for calculating the effective thermal conductivities in core–shell models, which is essential to design metamaterials. However, the main studies were confined in circular or spherical cases. Elliptical or even irregular core–shell structures need to be further investigated for generalizing these theoretical predictions.

The above discussions are based on linear materials, that is, thermal conductivities are temperature-independent (linear). However, one category of natural materials has temperature-dependent (nonlinear) thermal conductivities. The nonlinear cases lead to many novel phenomena different from linear ones in most research fields [91]. A convenient method is to solve the nonlinear conduction equation directly. Dai et al. [92] and Yang et al. [93] respectively studied

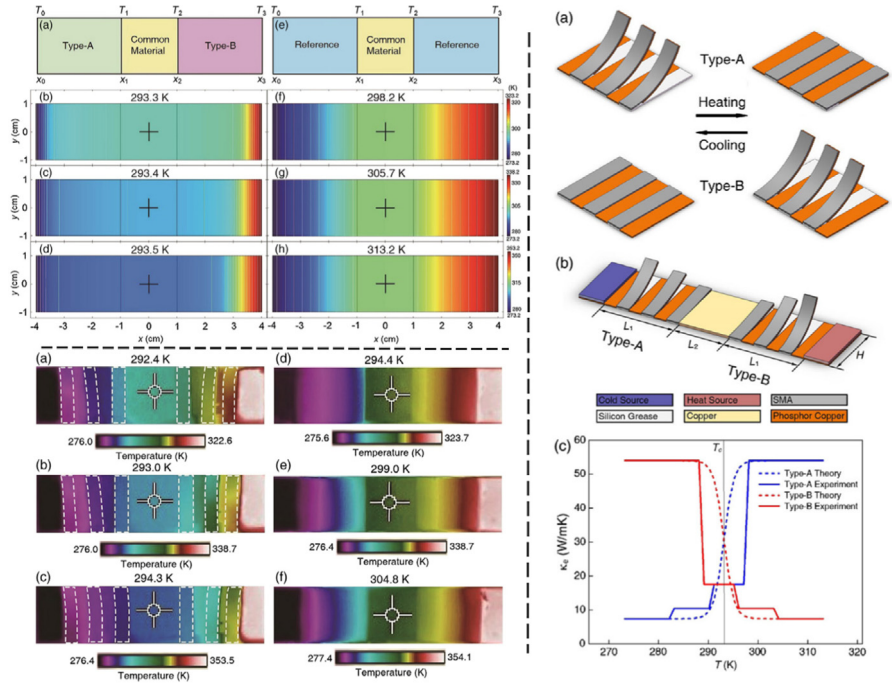

Fig. 2.13. Simulation and experimental results of an energy-free thermostat. Up-left panels: (a) Schematic graph of an energy-free thermostat, which consists of common material and type-A (type-B) nonlinear materials; (b–d) Simulations of (a) for different temperatures; (e) Schematic graph of a reference model; (f)–(h) Simulations of (e). For all the simulations, central temperatures (marked with +) are extracted and shown above each panel. Down-left panels: (-) Experimental results corresponding to (b–d) in up-left panels, respectively. The central temperatures keep almost unchanged. (d–f) Experimental results corresponding to (f–h) in up-left panels, respectively. The measured central temperature varies evidently. Right panels: (a) Schematic graph of type-A and type-B nonlinear materials; (b) Schematic graph of the experimental setup; (c) The relationship between the effective thermal conductivity and temperatures for type-A and type-B materials.
Source: Adapted from Ref. [45].

the weak nonlinearity in many-particle composite systems and core–shell structures, in which thermal conductivities can be executed by the Taylor expansion. Then, the enhancement of nonlinear coefficient can be calculated. About strong nonlinearity cases, Dai et al. developed a new approach by introducing Rayleigh method [94], and they simulated an effective thermal diode with asymmetrical nonlinear materials. Recently, Wang et al. [95] designed thermal bistability in macroscopic diffusion systems with asymmetrical nonlinearity, which is a macroscopic counterpart of microscope thermal memory proposed in 2008 [96]. The classical Kirchhoff transformation method was also introduced for treating nonlinear heat transfer problems in their work. The proposed macroscopic bistability made an attempt in macroscopic calculations. Subsequent research may be to apply the nonlinearity property in designing other macroscopic calculation elements and integrating them for practical applications.

Phase-change theory, describing a kind of extremely strong nonlinearity phenomena beyond common nonlinear cases, was introduced in the design of thermal metamaterials. In 2016, Shen et al. proposed an energy-free thermostat device with antisymmetric phase-change materials assembled at both sides of a high-conductivity common material [45]. When the ambient temperature varies, the applied phase-change material (shape-memory alloy) is self-adapting to the environments, keeping the central temperature invariant. The energy of temperature maintenance is totally from the ambient temperature. They conducted experiments and simulations to verify the theory. In detail, they used the composites of shape-memory alloys and copper to achieve the effective thermal conductivity in the form of a step function. Their simple experimental setup makes it possible to be used in daily life and industry, see Fig. 2.13. Wang et al. generalized this concept and introduced thermo-electric effects [97]. As a result, they designed a thermostat with electric-energy generation within ambient temperature differences. Coupling multiple physical fields may be a research tendency for phase-change metamaterials.

In the above discussion, no matter transformation method or scattering cancellation method, the problems of singular and uncommon thermal conductivities still cannot be solved simultaneously. For example, one may resort to a matrix with a very high thermal conductivity, such as copper (400 W m^{-1} K^{-1}) because high thermal conductivities correspond to the high efficiency of heat transfer. When a bilayer cloak is designed, thermal conductivities of the inner and outer shells are respectively 0 and 2615 W m^{-1} K^{-1}, which are singular and uncommon; see Fig. 2.14(a). When the concept of neutral inclusion [71,74,75,98] is used, the thermal conductivity of the shell should be 727 W m^{-1} K^{-1}, which is also uncommon; see Fig. 2.14(b). When a near-zero-index cloak [68] is designed, the thermal conductivity of the inner shell should tend to

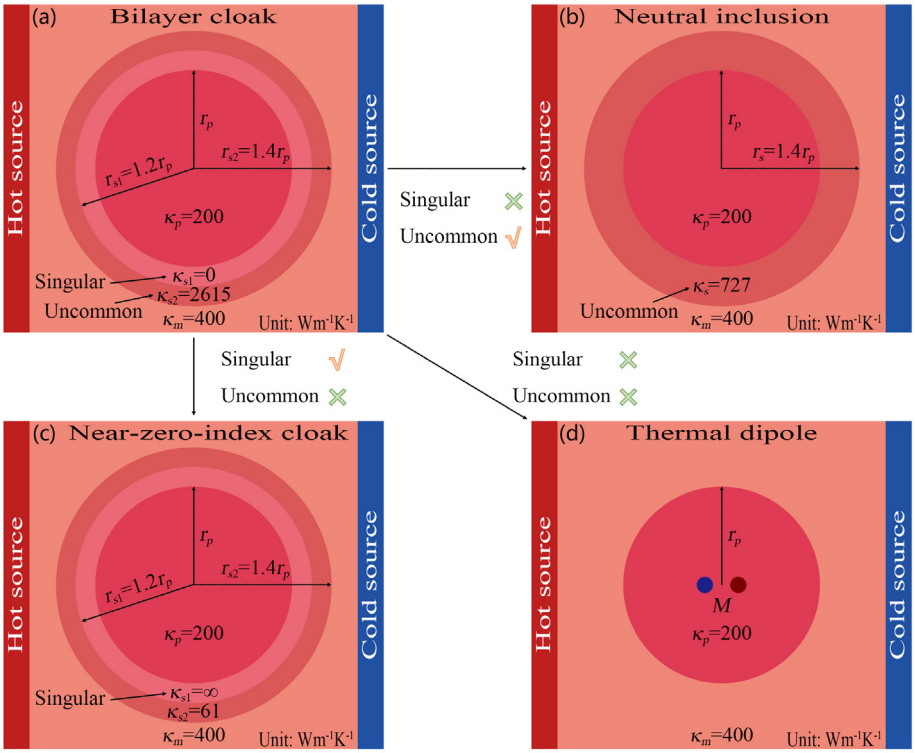

Fig. 2.14. Different approaches to thermal invisibility. (a) A bilayer cloak. $\kappa_m = \kappa_{s2}(1-p)/(1+p)$, and $p = (r_{s1}/r_{s2})^2$. (b) The concept of neutral inclusion. $\kappa_m = \kappa_s\left(\kappa_p+\kappa_s+\left(\kappa_p-\kappa_s\right)p\right)/\left(\kappa_p+\kappa_s-\left(\kappa_p-\kappa_s\right)p\right)$ where $p = \left(r_p/r_s\right)^2$. (c) A near-zero-index cloak. $\kappa_m = \kappa_{s2}(1+p)/(1-p)$, and $p = (r_{s1}/r_{s2})^2$. (d) A thermal dipole. Clearly, none of these approaches can simultaneously remove the requirements of singular and uncommon thermal conductivities except for the present dipole-driven scheme.
Source: Adapted from Ref. [99].

infinity, which is singular; see Fig. 2.14(c). These two problems (singular and uncommon thermal conductivities) largely restrict the development of thermal metamaterials because they require either complex structures or rare materials. For example, for the realization of infinite thermal conductivities, thermal convection should be introduced based on complex structures [68].

To completely solve these two problems, Xu et al. proposed the theory of dipole-assisted thermotics [99]. Such a scheme can neglect the requirements of singular and uncommon thermal conductivities simultaneously. Furthermore, dipole-assisted thermotics does not even have to design a shell, and an appropriate thermal dipole is enough which is shown in Fig. 2.14(d). This lies in the particularity of the thermal field of a thermal dipole, which can just offset the influence of a particle by designing the thermal dipole moment (M).

Aims of thermal invisibility are to keep the matrix thermal field undistorted, so one should focus on the matrix thermal field. When a particle (with thermal conductivity κ_p and radius r_p) is embedded in the matrix (with thermal conductivity κ_m) and in the presence of an external uniform thermal field $\boldsymbol{G}_0$, it will distort the matrix thermal field. The matrix thermal field (generated by the external uniform thermal field), is denoted as $\boldsymbol{G}_{me}$. It can be expressed as

$$\boldsymbol{G}_{me} = -\nabla T_{me}. \tag{2.15}$$

T_{me} denotes the temperature distribution which is given by [81]

$$T_{me} = -G_0 r\cos\theta - \frac{\kappa_m-\kappa_p}{\kappa_m+\kappa_p} r_p^2 G_0 r^{-1}\cos\theta + T_0, \tag{2.16}$$

where $(r,\ \theta)$ is the cylindrical coordinates whose origin is in the center of the particle, $G_0 = |\boldsymbol{G}_0|$, and T_0 is the temperature at $\theta = \pm\pi/2$.

The thermal dipole (with heater power Q and distance l) will generate a thermal field in the matrix when that is in the center of the particle. The matrix thermal field (generated by the thermal dipole), denoted as $\boldsymbol{G}_{md}$, which can be written as

$$\boldsymbol{G}_{md} = -\nabla T_{md}. \tag{2.17}$$

T_{md} is the temperature distribution given by

$$T_{md} = \frac{M}{\pi\left(\kappa_m + \kappa_p\right)} r^{-1}\cos\theta + T_0, \tag{2.18}$$

where M is the thermal dipole moment given by $M = Ql$. When $r \gg l$, which is investigated in the discussion section, Eq. (2.18) is valid. The following is detailed derivations of Eq. (2.18). The general solution [81] to the heat conduction equation $\nabla\cdot(-\kappa\nabla T) = 0$ in passive regions can be expressed as

$$T = A_0 + B_0\ln r + \sum_{i=1}^{\infty}\left[A_i\sin(i\theta) + B_i\cos(i\theta)\right] r^i + \sum_{j=1}^{\infty}\left[C_j\sin(j\theta) + D_j\cos(j\theta)\right] r^{-j}. \tag{2.19}$$

Because of the continuous temperatures and normal heat fluxes, boundary conditions can be written as

$$T_{pd}\left(r_p\right) = T_{md}\left(r_p\right), \tag{2.20}$$

$$\left(-\kappa_p\partial T_{pd}/\partial r\right)_{r_p} = \left(-\kappa_m\partial T_{md}/\partial r\right)_{r_p}, \tag{2.21}$$

where T_{pd} and T_{md} are temperature distributions (generated by the thermal dipole) of the particle and matrix, respectively.

To determine the forms of T_{pd} and T_{md}, Xu et al. performed some limit analyses. Suppose $r_p \to \infty$, and express the particle temperature distribution (generated by the thermal dipole) as

$$T_{pd}\left(r_p \to \infty\right) = \frac{-Q}{2\pi\kappa_p}\ln r_+ + \frac{Q}{2\pi\kappa_p}\ln r_- = \frac{Ql}{2\pi\kappa_p} r^{-1}\cos\theta = \frac{M}{2\pi\kappa_p} r^{-1}\cos\theta, \tag{2.22}$$

where r_+ and r_- are the distances to the heater and cooler of the dipole, respectively. When $r \gg l$ (or $l \to 0$), Eq. (2.22) is valid. Thus, the temperature distribution of a thermal dipole in two dimensions is characterized by $r^{-1}\cos\theta$.

Furthermore, consider that r_p is finite. The matrix temperature distribution should have the form of $r^{-1}\cos\theta$, but with a different coefficient from Eq. (2.22). The particle temperature distribution has two components. One is determined by Eq. (2.22), and the other is a uniform thermal field generated by the "thermal polarization". These can be concluded as

$$T_{pd} = \frac{M}{2\pi\kappa_p} r^{-1}\cos\theta + \alpha r\cos\theta + T_0, \tag{2.23}$$

$$T_{md} = \beta r^{-1}\cos\theta + T_0. \tag{2.24}$$

The undetermined coefficients can be derived by solving Eqs. (2.20)–(2.21) and Eqs. (2.23)–(2.24),

$$\alpha = \frac{-M\left(\kappa_m - \kappa_p\right)}{2\pi r_p^2\kappa_p\left(\kappa_m + \kappa_p\right)}, \tag{2.25}$$

$$\beta = \frac{M}{\pi\left(\kappa_m + \kappa_p\right)}. \tag{2.26}$$

With Eq. (2.26), Eq. (2.24) becomes Eq. (2.18).

Because of the superposition principle of vector fields, the matrix thermal field which is generated by the external uniform thermal field and thermal dipole together can be denoted as $\boldsymbol{G}_s$. Then,

$$\boldsymbol{G}_s = \boldsymbol{G}_{me} + \boldsymbol{G}_{md} = -\nabla T_s. \tag{2.27}$$

T_s is the temperature distribution given by

$$T_s = -G_0 r\cos\theta - \left(\frac{\kappa_m - \kappa_p}{\kappa_m + \kappa_p} r_p^2 G_0 - \frac{M}{\pi\left(\kappa_m + \kappa_p\right)}\right) r^{-1}\cos\theta + T_0. \tag{2.28}$$

When the thermal field of the matrix is undistorted, thermal invisibility is obtained, and thus the second term on the right side of Eq. (2.28) should be zero,

$$\frac{\kappa_m - \kappa_p}{\kappa_m + \kappa_p} r_p^2 G_0 - \frac{M}{\pi\left(\kappa_m + \kappa_p\right)} = 0. \tag{2.29}$$

The thermal dipole moment can be derived by solving Eq. (2.29),

$$M = \left(\kappa_m - \kappa_p\right) f G_0, \tag{2.30}$$

where $f = \pi r_p^2$ is the acreage of the particle. Thermal invisibility can be achieved when the thermal dipole moment is set as required by Eq. (2.30).

Xu et al. further performed two dimensional finite-element simulations to confirm the theoretical analyses. The temperatures of the left and right boundaries are set at 323 K and 283 K, and the upper and lower boundaries are

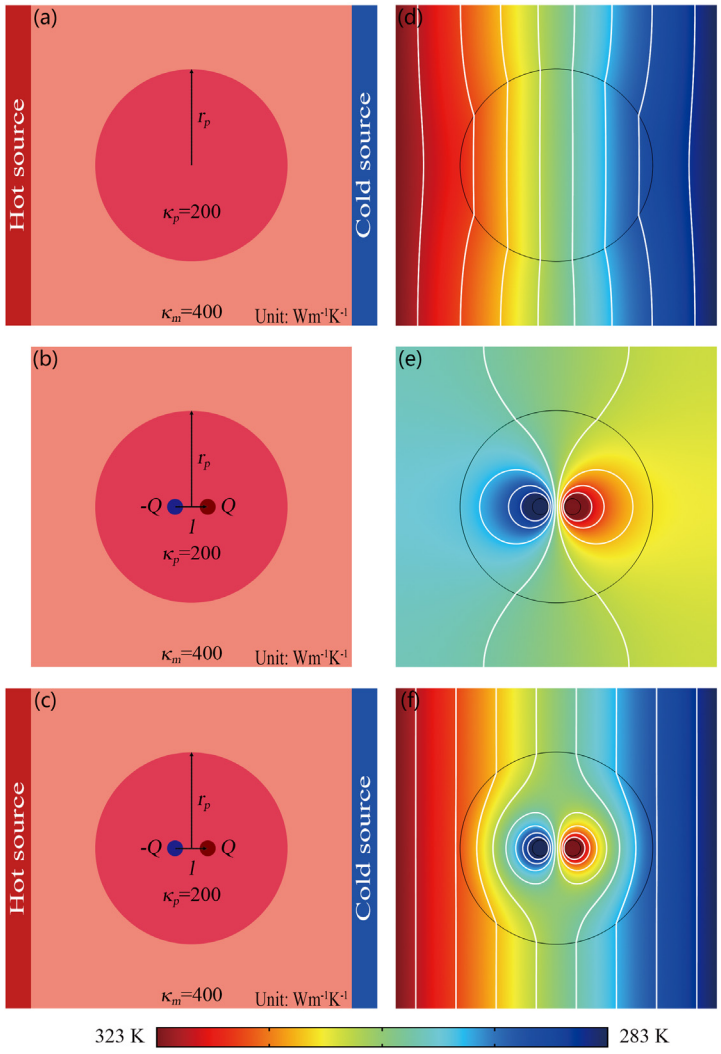

Fig. 2.15. Finite-element simulations in the presence of (a) and (d) an external uniform thermal field, (b) and (e) a thermal dipole, and (c) and (f) an external uniform thermal field and a thermal dipole together. The simulation box is 20 × 20 cm^2, r_p = 6 cm, and l = 2 cm. The thermal conductivities of the particle and the matrix are 200 and 400 W m^{-1} K^{-1}, respectively. The thermal dipole moment should be 452.4 W·m as required by Eq. (2.30), which leads to Q = 22620 W. The heater or cooler of the thermal dipole has a radius 0.5 cm. White lines represent isotherms. For the convenience of comparison, temperatures higher than 323 K are shown as 323 K, and temperatures lower than 283 K are shown as 283 K. *Source:* Adapted from Ref. [99].

insulated; see Fig. 2.15(a) and (d). In Fig. 2.15(d), there is a particle with different thermal conductivity from the matrix in the center, and the isotherms are contracted due to the smaller thermal conductivity of the particle. The particle is visible with infrared detection because of the distorted temperature profile. Then, Xu et al. explored the thermal profile of a thermal dipole; see Fig. 2.15(b) and (e). The temperature profile is presented in Fig. 2.15(e). Xu et al. set the temperature at $\theta = \pm\pi/2$ at 303 K as reference temperature and all boundaries are insulated. Finally, combine the structures which are presented in Fig. 2.15(a) and 2.15(b) together. Then, the expected structure is obtained, shown in Fig. 2.15(c). As predicted by Eq. (2.30), the distorted temperature profile can be restored; see Fig. 2.15(f). Therefore, thermal invisibility is achieved with a thermal dipole because the particle becomes invisible with infrared detection.

To validate the theoretical analyses and finite-element simulations, Xu et al. also performed laboratory experiments. The sample based on a copper plate (400 W m^{-1} K^{-1}) are fabricated by laser cut. In Fig. 2.16(a), air holes (0.026 W m^{-1} K^{-1}) are engraved on the copper plate to make the effective thermal conductivity of the corresponding region to be 200 W m^{-1} K^{-1}. To reduce the negative effects of infrared reflection and thermal convection, the upper and lower surfaces are covered with the transparent plastic and foamed plastic respectively.

The designed power of the thermal dipole is an extremely large value, say, 22 620 W for the heater and −22 620 W for the cooler, respectively. The thermal dipole can maintain the uniform thermal field of the matrix and also generate a

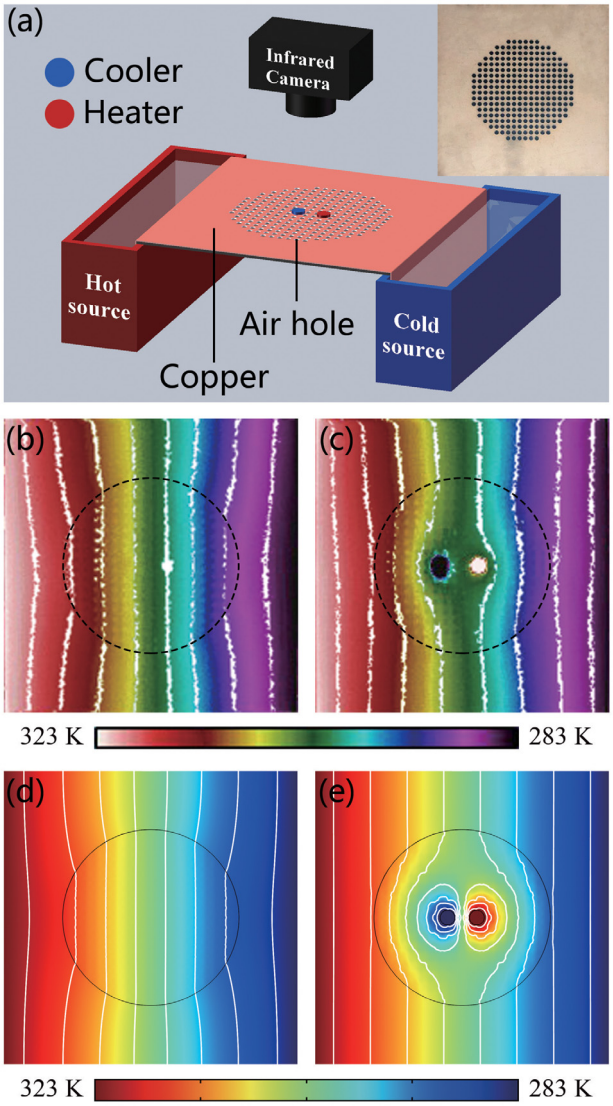

Fig. 2.16. Laboratory experiments. (a) is schematic diagrams of the experimental devices and fabricated sample. (b) and (c) are the measured results without and with a thermal dipole. (d) and (e) are the corresponding finite-element simulations based on the experimental settings in (a). Copper: thermal conductivity 400 W m^{-1} K^{-1}, density 8960 kg·m^{-3}, and heat capacity 385 J kg^{-1} K^{-1}. Air: thermal conductivity 0.026 W m^{-1} K^{-1}, density 1.29×10^{-3} kg·m^{-3}, and heat capacity 1005 J kg^{-1} K^{-1}. The radius of the 256 air holes is 0.22 cm, and the distance between air holes is 2/3 cm. *Source:* Adapted from Ref. [99].

higher/lower temperature inside the heater/cooler than the hot/cold source. To be mentioned, only the edge temperature of the heater/cooler makes sense so the higher/lower temperature inside the heater/cooler does not contribute to the effect of thermal invisibility. Such statement can be understood by the uniqueness theorem in thermotics [100]. Therefore, when the temperature of heater/cooler is kept as 325/281 K, thermal invisibility can be achieved as ensured by the uniqueness theorem in thermotics. 325/281 K is obtained from the finite-element simulation; see Fig. 2.15(f). The temperatures are dependent on the radius of the heater/cooler. Thus, the thermal dipole is realized by a ceramic heater and an ice water bag in their work. Water can maintain a constant temperature for several minutes since its heat capacity is a very large value, say, 4.2×10^3 J kg^{-1} K^{-1}. It is enough for the steady experiments.

Xu et al. measured the sample between the hot source (323 K) and the cold source (283 K) with infrared camera Flir E60. The temperature distribution without and with a thermal dipole can be found in Fig. 2.16(b) and (c), respectively. Moreover, based on the structure presented in Fig. 2.16(a), they have performed finite-element simulations. The thermal dipole is set at two constant temperatures shown in Fig. 2.16(d) and (e). The theory is validated by both the experimental results [Fig. 2.16(b) and (c)] and finite-element simulations [Fig. 2.15(d), and (f), 2.16(d), and (e)].

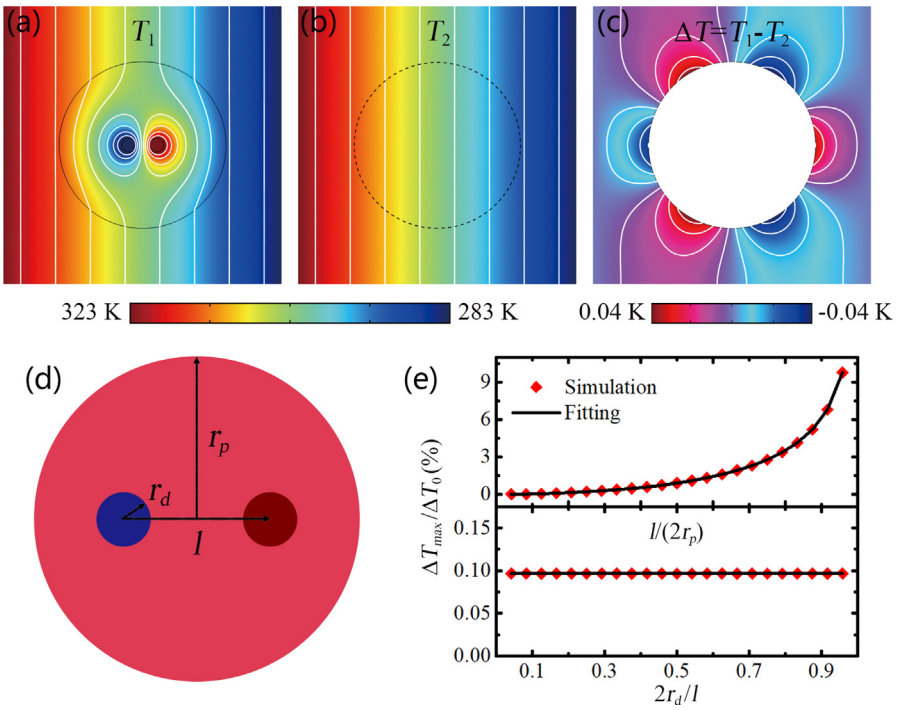

Fig. 2.17. Effects of the thermal dipole on thermal invisibility. (a) The dipole-driven temperature distribution. (b) The temperature distribution when the thermal conductivities of the matrix and particle are the same (400 W m^{-1} K^{-1}). (c) The matrix temperature-difference distribution. (d) and (e) shows the effects of two parameters (l and r_d) on thermal invisibility. The upper panel in (e) is with $r_d = 0$ cm. The lower panel in (e) is with $l = 2$ cm.
Source: Adapted from Ref. [99].

$r \gg l$ is the only one approximation in the whole process to ensure the validity of Eq. (2.18). Therefore, Xu et al. discussed the effect of the approximation on thermal invisibility. It can be seen that the matrix temperature distributions are totally the same by comparing the dipole-driven result shown in Fig. 2.17(a) whose parameters are the same as those for Fig. 2.15(f) with a reference [Fig. 2.17(b)]. Then, to present quantitative analyses, Xu et al. plotted the matrix temperature-difference distribution, say, $\Delta T = T_1 - T_2$; see Fig. 2.17(c). The maximum value of the temperature difference (ΔT_{max}) is 0.04 K. Compared with the temperature difference between the hot and cold sources ($\Delta T_0 = 40$ K), the relative error ($\Delta T_{max}/\Delta T_0$) is only 0.1%. So the dipole-driven scheme shows the excellent performance.

Clearly, the effect of the thermal dipole on thermal invisibility can be reflected by relative errors. Therefore, Xu et al. calculated $\Delta T_{max}/\Delta T_0$ with different r_d (the radius of the heater or cooler) and l (the distance between the heater and cooler); see Fig. 2.17(d), and plot two curves showing $\Delta T_{max}/\Delta T_0$ changing with $l/(2r_p)$ and $2r_d/l$; see Fig. 2.17(e). The upper curve proves that the performance of the thermal dipole decreases with the increment of $l/(2r_p)$; see Fig. 2.17(e). When $l/(2r_p) \to 0$, $\Delta T_{max}/\Delta T_0 \to 0$, which indicates the perfect performance. However, the lower curve in Fig. 2.17(e) shows that the performance of the thermal dipole keeps unchanged with the increment of $2r_d/l$. Therefore, only one parameter (say, the distance l) mainly affects the effect of the thermal dipole on thermal invisibility, and the shorter it is the better.

Based on the experimental settings presented in Fig. 2.16(a), Xu et al. also performed transient simulations; see Fig. 5 of Ref. [99]. When the initial temperature is set at the middle temperature of the hot and cold sources, the transient behavior is good. References without a thermal dipole are shown in Fig. 5(a–d) of Ref. [99]. The distorted matrix isotherms make the particle in the center visible. By contrast, the straight matrix isotherms demonstrate that the thermal dipole can realize thermal invisibility in transient regimes; see Figs. 5(e–h) of Ref. [99].

Use primes to indicate three dimensions. The matrix's thermal field (generated by the external uniform thermal field $\boldsymbol{G}_0'$), denoted as $\boldsymbol{G}_{me}'$, can be expressed as

$$\boldsymbol{G}_{me}' = -\nabla T_{me}'. \tag{2.31}$$

T_{me}' is the temperature distribution given by [81]

$$T_{me}' = -G_0' r\cos\theta - \frac{\kappa_m' - \kappa_p'}{2\kappa_m' + \kappa_p'} r_p'^3 G_0' r^{-2}\cos\theta + T_0'. \tag{2.32}$$

The matrix thermal field (generated by the thermal dipole), denoted as $\boldsymbol{G}'_{md}$, can be expressed as

$$\boldsymbol{G}'_{md} = -\nabla T'_{md}. \tag{2.33}$$

T'_{md} is the temperature distribution given by

$$T'_{md} = \frac{3M'}{4\pi\left(2\kappa'_m + \kappa'_p\right)} r^{-2}\cos\theta + T'_0. \tag{2.34}$$

The following is detailed derivations of Eq. (2.34). The general solution to the heat conduction equation in three dimensions is [81]

$$T = \sum_{i=0}^{\infty}\left(A_i r^{-1/2+\sqrt{1/4+i(i+1)}} + B_i r^{-1/2-\sqrt{1/4+i(i+1)}}\right) P_i\left(\cos\theta\right), \tag{2.35}$$

where P_i is the Legendre polynomial. The boundary conditions are given by the continuous temperatures and heat fluxes, which have the same mathematical forms as Eqs. (2.20)–(2.21). Xu et al. performed similar limit analyses to determine the forms of T'_{pd} and T'_{md}, and suppose $r'_p \to \infty$, and then the particle temperature distribution (generated by the thermal dipole) in three dimensions can be expressed as

$$T'_{pd}\left(r'_p \to \infty\right) = \frac{Q'}{4\pi\kappa'_p} r'^{-1}_{+} + \frac{-Q'}{4\pi\kappa'_p} r'^{-1}_{-} = \frac{Q'l'}{4\pi\kappa'_p} r^{-2}\cos\theta = \frac{M'}{4\pi\kappa'_p} r^{-2}\cos\theta, \tag{2.36}$$

Eq. (2.36) is valid only when $r \gg l'$ (or $l' \to 0$). The temperature distribution of a thermal dipole in three dimensions is characterized by $r^{-2}\cos\theta$. Then consider a finite r'_p. Similar to two dimensions, T'_{pd} and T'_{md} can be expressed as

$$T'_{pd} = \frac{M'}{4\pi\kappa'_p} r^{-2}\cos\theta + \alpha' r\cos\theta + T'_0, \tag{2.37}$$

$$T'_{md} = \beta' r^{-2}\cos\theta + T'_0. \tag{2.38}$$

The undetermined coefficients can be derived by solving Eqs. (2.20)–(2.21) and Eqs. (2.37)–(2.38),

$$\alpha' = \frac{-M'\left(\kappa'_m - \kappa'_p\right)}{2\pi r'^3_p \kappa'_p\left(2\kappa'_m + \kappa'_p\right)}, \tag{2.39}$$

$$\beta' = \frac{3M'}{4\pi\left(2\kappa'_m + \kappa'_p\right)}. \tag{2.40}$$

With Eq. (2.40), Eq. (2.38) becomes Eq. (2.34).

The matrix thermal field (generated by the external uniform thermal field and the thermal dipole together) can be denoted as $\boldsymbol{G}'_s$ because of the superposition principle,

$$\boldsymbol{G}'_s = \boldsymbol{G}'_{me} + \boldsymbol{G}'_{md} = -\nabla T'_s. \tag{2.41}$$

T'_s is the temperature distribution given by

$$T'_s = -G'_0 r\cos\theta - \left[\frac{\kappa'_m - \kappa'_p}{2\kappa'_m + \kappa'_p} r'^3_p G'_0 - \frac{3M'}{4\pi\left(2\kappa'_m + \kappa'_p\right)}\right] r^{-2}\cos\theta + T'_0. \tag{2.42}$$

To achieve thermal invisibility, the second term on the right side of Eq. (2.42) to be zero,

$$\frac{\kappa'_m - \kappa'_p}{2\kappa'_m + \kappa'_p} r'^3_p G'_0 - \frac{3M'}{4\pi\left(2\kappa'_m + \kappa'_p\right)} = 0, \tag{2.43}$$

The thermal dipole moment can be derived by solving Eq. (2.43),

$$M' = \left(\kappa'_m - \kappa'_p\right) f' G'_0, \tag{2.44}$$

where $f' = 4\pi r'^3_p/3$ is the volume of the particle.

The dipole-driven scheme has shown the flexibility and superiority in thermal management, and potential applications in infrared signature reduction. For example, an object (with different thermal conductivity from the matrix) in a system will distort the infrared signature. However, if applying the dipole-driven scheme, the distortion will reduce to ensure a pure infrared signature. Thermal dipoles may also realize other thermal phenomena beyond invisibility, such as thermal camouflage [101–103], thermal Janus structures [82], and many-particle systems [79,104]. Moreover, the properties of thermal quadrupole may contain other interesting points. To be mentioned, the essence of their work is about macroscopic thermal processes rather than thermal conductivities. Although the dipole-driven scheme is at the macroscale, it may also be extended to the nanoscale [105,106].

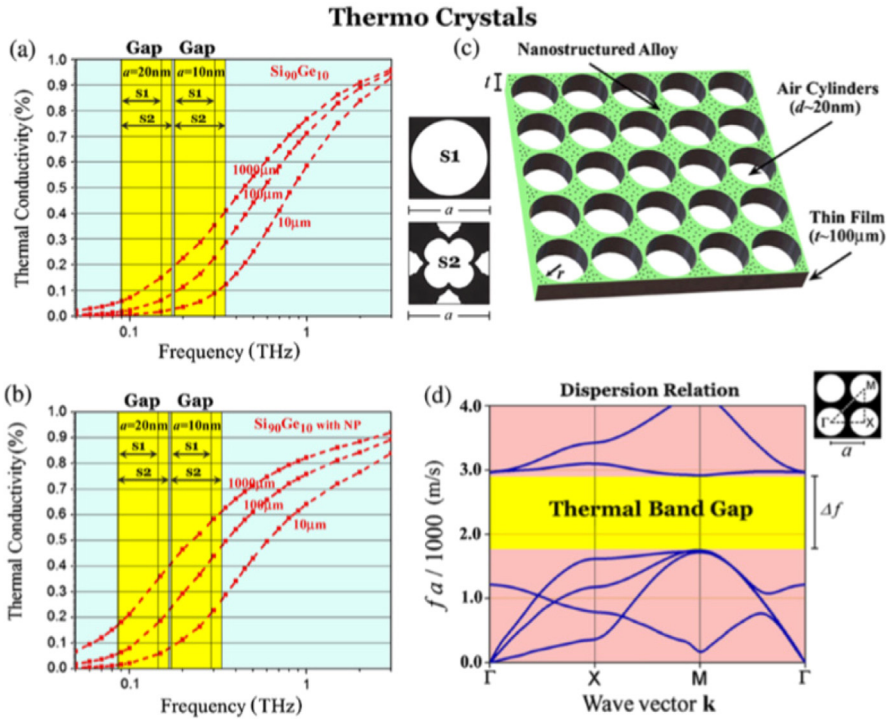

Fig. 2.18. (a) and (b) Yellow areas are the frequency gaps with patterns S1 and S2, respectively. (c) Schematic diagram of thermocrystal. (d) The corresponding phononic band diagram.
Source: Figure reprinted with permission from Maldovan Phys. Rev. Lett., 110, 025902, 2013.

2.2.2. Phonon transport theory

Phonon transport is the dominant microscopic mechanism of heat transfer in non-metal materials. For wave systems, crystal structures based on either the Bragg scattering in periodic structures or the local resonance have been widely utilized to manipulate light and sound. However, although phonons are the dominant heat carrier in non-metallic materials, thermal phonons usually have much smaller wave lengths (nanoscale) than acoustic phonons, so they are easier to be scattered. Thus, under room temperatures, thermal phonons behave more like diffusive particles than waves. Nanoscale wavelengths also make it difficult to fabricate corresponding periodic structures to control thermal phonons. To exhibit the wave nature of thermal phonons, Maldovan predicted a material with a narrow phonon spectrum for heat transfer [107]; see Fig. 2.18. On the one hand, germanium nanoparticles are incorporated into silicon germanium alloy to shorten the mean free path of high-frequency phonons. On the other hand, extreme low-frequency phonons are also blocked from transport by boundary scattering of a thin film. Thus, thermal phonons in this material are concentrated into a narrow hypersonic spectrum, which can be handled as acoustic phonons. Then, Maldovan designed periodic air-hole structures with periodicity of 10–20 nm in this material, and its phononic band simulated by continuum mechanics has a gap located in the narrow hypersonic spectrum. So, it may be called a thermocrystal, and can be used to manipulate heat flux. Based on the thermocrystal, they have some proposals about thermal devices; see Fig. 2.19. Also, local resonance can generate hybridization gaps and then control heat conduction accordingly. Davids and Hussein designed a silicon thin film with pillars periodically placed on it and called it nanophononic metamaterial [108]. Each pillar is a local resonator and can be coupled with propagating bulk phonons with the same frequency and polarization, which is called anti-crossing and can generate band gaps at frequencies below 4 THz. Thus, the thermal conductivity is reduced accordingly. In addition, Zhu et al. found that hybridization gaps can also exist when disorder is introduced into the material [109]. Random defects as localized modes can also be coupled with delocalized modes, so anti-crossing happens. One can see that the band theory in heat conduction is actually related to phononic band engineering. Two recent reviews are available on thermal transport engineering based on phononic crystals or nanophononic metamaterial [110,111].

Recently, Zhang's group made a significant progress on the theory of phonon transport [112]. Inspired by the theoretical prediction of Pendry et al. [113], they experimentally demonstrated a heat-transfer process between two plates with a hundreds-of-nanometer gap; see Fig. 2.20. The space of the intermediate region is vacuum, so only radiative transfer seems to work. Interestingly, after they checked the energy transport process, they excluded the radiative modes (even near-field radiation). As a result, they concluded that the quantum fluctuation of phonons mediated by the Casimir effect is the only reason to explain their findings related to heat conduction in vacuum. Their experimental result is a solid

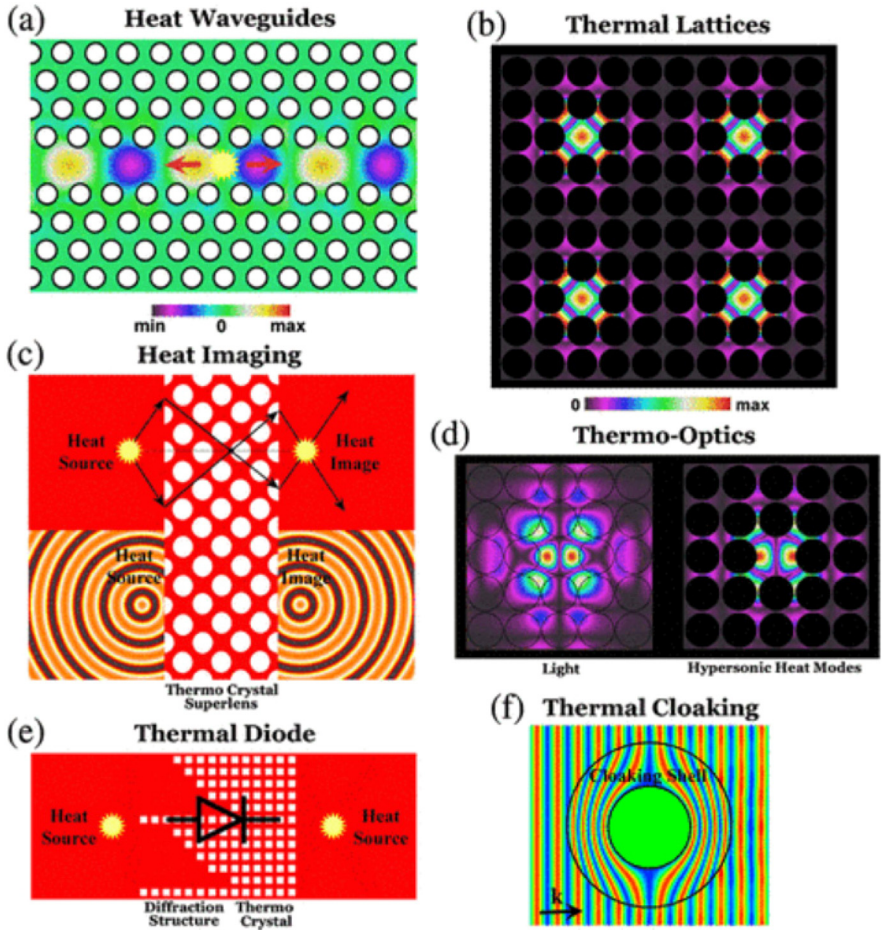

Fig. 2.19. Applications of thermocrystal. (a) Heat waveguide. (b) Thermal lattice. (c) Heat imaging. (d) Thermo-optics. (e) Thermal diode. (f) Thermal cloak.
Source: Figure reprinted with permission from Maldovan Phys. Rev. Lett., 110, 025902, 2013.

verification of the previous theoretical prediction. Their work also has practical implications to thermal management in nanotechnology.

2.2.3. Application

So far, several typical thermal metamaterials including thermal cloaking, thermal concentrating, and thermal rotating, thermal camouflaging are introduced. For practical applications, Dede et al. [114,115] combined three devices, say, thermal cloaking, concentrating, and rotating on a single printed circuit board to realize the efficient heat dissipation of electronic devices; see Fig. 2.21. The experimental results indicated that the local temperature can be 10 degrees lower than that without the designed structure, which shows an exciting performance in thermal dissipation. Simulation and experimental results can be seen in Fig. 7 of Ref. [114]. Therefore, the scheme can be expected to have more practical applications in heat dissipation, especially for miniature devices.

3. Controlling heat conduction and convection

3.1. Transformation method

3.1.1. Unsteady state

Convection is also a fundamental mechanism of heat transfer, which is usually the dominant one in moving media like fluids. Convection means that heat transport is driven by the movement of media. More precisely, the mechanism refers to advection. Usually, convection coexists with other mechanisms especially conduction, and the typical governing equation

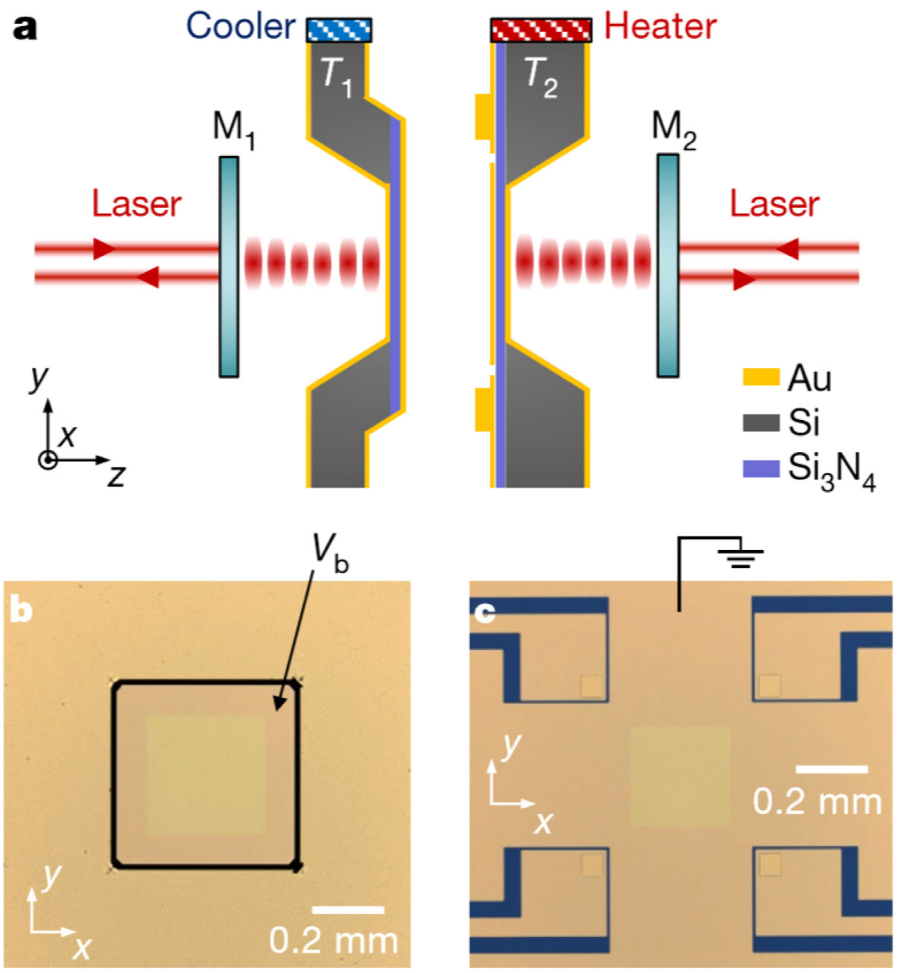

Fig. 2.20. (a) Schematic diagram of the experimental set up. (b, c) Optical images of the left and right samples. *Source:* Figure reprinted with permission from Fong et al. Nature, 576, 243, 2019.

of heat transfer in moving media is the well-known convection–diffusion equation, which can be directly obtained by using material derivative of time in the Fourier law.

Now the first question is how to extend the previous designs for heat conduction (including cloaks, concentrators and rotators) to convective environments. Guenneau et al. proved that the convection–diffusion equation satisfies the transformation theory and gave transformation rules of thermal conductivity and velocity of fluids [116,117]. However, the convection–diffusion equation cannot determine the whole thermodynamic quantities of fluids, so how to achieve the required velocity distribution is still a problem. As Landau and Lifshitz wrote in their textbook [118], one needs five quantities to describe the state of moving fluid in a three-dimensional space. Thus, there should exist five governing equations, namely, three spatial components of the Navier–Stokes equations, the continuity equation of fluid motion, and the convection–diffusion equation. In general, the processes of heat and mass transfer are coupled with each other, so manipulating thermal convection means designing a bifunctional device which can control thermal fields and fluid fields simultaneously. Since the Navier–Stokes equations do not meet the requirement of transformation theory, researchers [119,120] followed the work of Urzhumov and Smith on fluid-flow cloak with the Darcy flow [121] and established a transforming convection theory based on the creeping flows in porous media.

In this work [120], Dai et al. proposed the transformation theory to handle unsteady thermal convection of creeping flow in a porous medium based on the model raised in Ref. [119], where temperature, velocity and material density are not restricted to constants during the process of heat and mass transfer. Then, they confirmed the theoretical designs of convective cloaks, concentrators and rotators in such unsteady regimes with finite-element simulations; see Fig. 3.1.

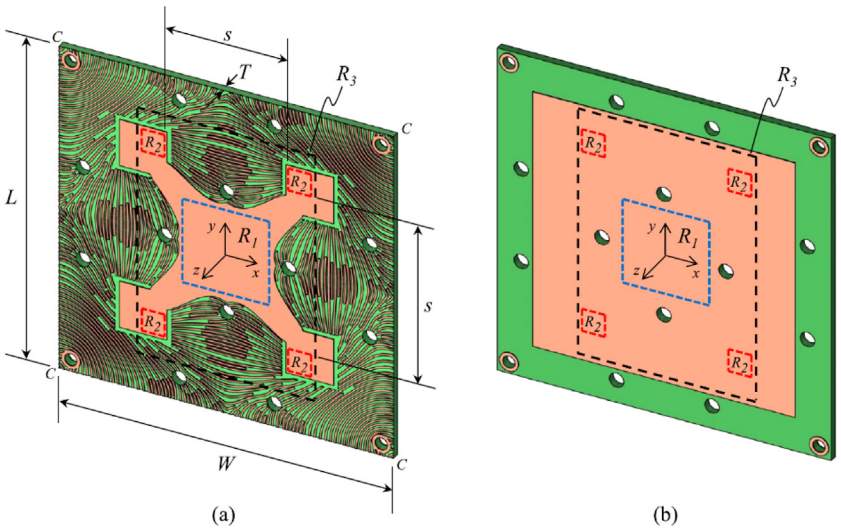

Fig. 2.21. (a) The schematic of thermal-composite substrate with optimized thermal metamaterials. (b) Baseline substrate. *Source:* Figure reprinted with permission from Dede et al. AIP Adv., 6, 055113, 2016.

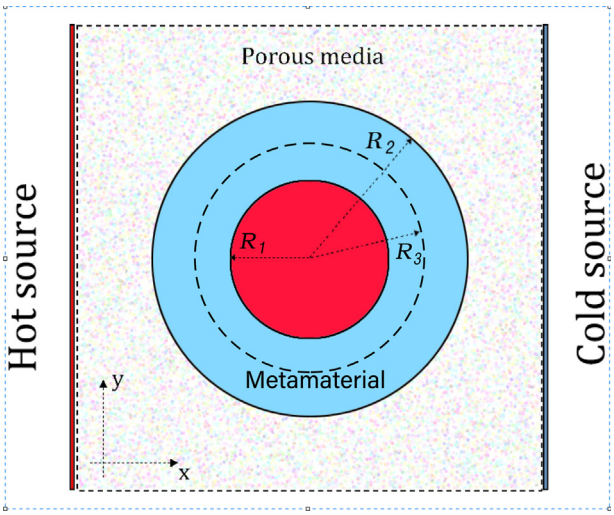

Fig. 3.1. Schematic design for cloak, concentrator or rotator in thermal conduction and convection. The ring-shaped area in light-blue is made of thermal metamaterials with the function of cloaking, concentrating or rotating for corresponding coordinate transformations. The black dashed circle with radius R_3 indicates the auxiliary parameter for concentrators.

Dai et al. extended the transformation theory to transient thermal convection in a porous medium. Firstly, the Darcy law can be modified as [122–124]

$$\tau \frac{\partial \vec{v}}{\partial t} + \vec{v} = -\frac{\beta}{\eta} \nabla p, \tag{3.1}$$

where τ is the characteristic time for varying velocity $\vec{v}$ with time t, β is the permeability of porous medium and η is dynamic viscosity. In general, the relaxation process is very fast in a porous medium, and then $\tau \frac{\partial \vec{v}}{\partial t}$ is quite small [124]. Therefore, this term can be neglected and the steady Darcy regime can be still used. Also, the continuity equation can be rewritten as [118]

$$\frac{\partial (\phi \rho_f)}{\partial t} + \nabla \cdot (\rho_f \vec{v}) = 0, \tag{3.2}$$

where ρ_f is the density of fluid material and ϕ is porosity. Then, the heat transfer of incompressible flow in a saturated porous medium is governed by [125,126]

$$\frac{\partial(\rho C)_m T}{\partial t} + \nabla \cdot (\rho_f C_f \vec{v} T) = \nabla \cdot (\kappa_m \nabla T), \tag{3.3}$$

where T is temperature and ρ_s is the density of solid. Here, C_f and C_s are the specific heat of fluid and solid material, respectively. The effective product of density and specific heat of the whole porous medium can be given by the average-volume method [126],

$$(\rho C)_m = (1-\phi)(\rho_s C_s) + \phi(\rho_f C_f). \tag{3.4}$$

Similarly, the effective thermal conductivity κ_m can also be the summation of κ_f (for fluids) and κ_s (for solids) according to the mean-volume method,

$$\kappa_m = (1-\phi)\kappa_s + \phi\kappa_f. \tag{3.5}$$

Eq. (3.3) is just the unsteady convection–diffusion equation whose form-invariance under coordinate transformations has been proved [116,117]. What is more, the substitution of Eq. (3.2) into Eq. (3.3) yields

$$(\rho C)_m \frac{\partial T}{\partial t} + \rho_f C_f (\vec{v} \cdot \nabla T) = \nabla \cdot (\kappa_m \nabla T). \tag{3.6}$$

Since Eq. (3.2) is an transient diffusion equation, it can be concluded that all the equations for unsteady heat and mass transfer in a porous medium can meet the requirement of transformation theory just like the steady cases [119]. For both steady and unsteady cases, the transformation matrix for a homogeneous space is $\frac{\mathbf{J}\mathbf{J}^{\mathrm{T}}}{\det \mathbf{J}}$, where $\mathbf{J}$ is the Jacobian matrix from the transformed coordinate to the original one. Still, Dai et al. transformed the permeability and heat conductivity as $\beta' = \frac{\mathbf{J}\beta\mathbf{J}^{\mathrm{T}}}{\det \mathbf{J}}$ and $\kappa'_m = \frac{\mathbf{J}\kappa_m\mathbf{J}^{\mathrm{T}}}{\det \mathbf{J}}$. The difference is that, for unsteady cases, Dai et al. must also transform the porosity and the product of density and specific heat as

$$\begin{cases} \phi' = \dfrac{\phi}{\det \mathbf{J}} \\ (\rho_f C_f)' = \rho_f C_f \\ (\rho_s C_s)' = \dfrac{1-\phi}{\det \mathbf{J} - \phi} \rho_s C_s \end{cases}. \tag{3.7}$$

In this way, one can keep fluid's parameters unchanged after transformation and only construct solid metamaterial as required. ρ_f is no longer a constant as it has a relationship with temperature changing with time. For simplicity, assume

$$\rho = \rho_0[1 - \gamma(T - T_0)], \tag{3.8}$$

where $\gamma = (\frac{\partial \rho}{\partial T})_p / \rho$ denotes the volume expansion ratio at constant pressure. Without loss of generality, set $\gamma > 0$. Finally, the set of transformed equations can be written as

$$\begin{cases} \vec{v}' = -\dfrac{\beta'}{\eta} \nabla p \\ \dfrac{\partial(\phi' \rho_f)}{\partial t} + \nabla \cdot (\rho_f \vec{v}') = 0 \\ (\rho C)'_m \dfrac{\partial T}{\partial t} + \rho_f C_f (\vec{v}' \cdot \nabla T) = \nabla \cdot (\kappa'_m \nabla T) \end{cases}, \tag{3.9}$$

where the transformed velocity $\vec{v}'$ is equal to $\mathbf{J}^{\mathrm{T}}\vec{v}/\det \mathbf{J}$ [116,117,119] and $(\rho C)'_m = (1-\phi')(\rho_s C_s)' + \phi'(\rho_f C_f)$.

In general, there are two ways of manipulating heat flux, namely, controlling area (volume) or direction. For heat conduction, some novel functional devices have been successfully designed, such as thermal cloaks, thermal concentrators and thermal rotators. Also, cloaks and concentrators for steady thermal convection have been theoretically designed [119], while the rotator has not. Here, Dai et al. tried to realize rotators in transient thermal convection. For simplicity, they established the model in a two-dimensional space and considered circular cloaks/concentrators/rotators.

Cloak. The familiar geometrical transformation [4]

$$\begin{cases} r' = R_1 + \dfrac{R_2 - R_1}{R_2} r, 0 < r < R_2 \\ \theta' = \theta \end{cases} \tag{3.10}$$

is used to protect the outside region $r' > R_1$ from being disturbed by objects placed in $0 < r' < R_1$. The corresponding Jacobian matrix is

$$\mathbf{J} = \begin{pmatrix} \cos\theta & -r'\sin\theta \\ \sin\theta & r'\cos\theta \end{pmatrix} \begin{pmatrix} \frac{R_2-R_1}{R_2} & 0 \\ 0 & 1 \end{pmatrix} \begin{pmatrix} \cos\theta & \sin\theta \\ -\frac{\sin\theta}{r} & \frac{\cos\theta}{r} \end{pmatrix}, \tag{3.11}$$

and it is easy to see

$$\det \mathbf{J} = \frac{R_2 - R_1}{R_2}\frac{r'}{r}. \tag{3.12}$$

Concentrator. Consider the transformation adopted in Ref. [127]

$$\begin{cases} r' = \dfrac{R_1}{R_3} r, r < R_3, \\ r' = \dfrac{R_1 - R_3}{R_2 - R_3} R_2 + \dfrac{R_2 - R_1}{R_2 - R_3} r, R_3 < r < R_2, \end{cases} \tag{3.13}$$

which squeezes the region $0 < r < R_3$ to $r' < R_1$ and stretching the region $R_3 < r < R_3$ to $R_1 < r' < R_2$. Physical quantities can be enlarged in the squeezed region. The corresponding Jacobian matrix is

$$\mathbf{J}_1 = \begin{pmatrix} \frac{R_1}{R_3} & 0 \\ 0 & \frac{R_1}{R_3} \end{pmatrix} \tag{3.14}$$

for region $r' < R_1$. So, the determinant is

$$\det \mathbf{J}_1 = \left(\frac{R_1}{R_3}\right)^2. \tag{3.15}$$

Also, for region $R_1 < r' < R_2$,

$$\mathbf{J}_2 = \begin{pmatrix} \cos\theta & -r'\sin\theta \\ \sin\theta & r'\cos\theta \end{pmatrix} \begin{pmatrix} \frac{R_2 - R_1}{R_2 - R_3} & 0 \\ 0 & 1 \end{pmatrix} \begin{pmatrix} \cos\theta & \sin\theta \\ -\frac{\sin\theta}{r} & \frac{\cos\theta}{r} \end{pmatrix} \tag{3.16}$$

and the determinant is

$$\det \mathbf{J}_2 = \frac{R_2 - R_1}{R_2 - R_3}\frac{r'}{r}. \tag{3.17}$$

Rotator. Moreover, it is also useful to guide the direction of heat flux at will. Dai et al. focused on the continuous transformation of direction, which can be realized by a rotator. To design a rotator for heat transfer, consider a space transformation proposed in Ref. [128],

$$\begin{cases} \theta' = \theta + \theta_0, r < R_1, \\ \theta' = ar + b, R_1 < r < R_2, \end{cases} \tag{3.18}$$

where $a = \frac{\theta_0}{R_1 - R_2}$, $b = \theta + \frac{R_2}{R_2 - R_1}\theta_0$ and $R_1 < r < R_2$. The transformation indicates that the region $r < R_1$ is rotated by an angle of θ_0, while in the region $R_1 < r < R_2$, the rotation angle gradually decreases from θ_0 to zero as r is reduced. The transformation matrix is also different in these two regions. For region $r < R_1$, the Jacobian matrix is expressed as

$$\mathbf{J}_1 = \begin{pmatrix} \cos\theta_0 & -\sin\theta_0 \\ \sin\theta_0 & \cos\theta_0 \end{pmatrix} \tag{3.19}$$

by which the velocity and heat flux are rotated by an angle of θ_0. Moreover, an identity transformation matrix can be written as

$$\frac{\mathbf{J}_1\mathbf{J}_1^{\mathrm{T}}}{\det \mathbf{J}_1} == \begin{pmatrix} 1 & 0 \\ 0 & 1 \end{pmatrix}, \tag{3.20}$$

so it is not necessary to do any transformation for material properties in this region. For region $R_1 < r < R_2$, a unitary Jacobian matrix can also be obtained

$$\mathbf{J}_2 = \begin{pmatrix} \cos\theta' & -r\sin\theta' \\ \sin\theta' & r\cos\theta' \end{pmatrix} \begin{pmatrix} 1 & 0 \\ \alpha & 1 \end{pmatrix} \begin{pmatrix} \cos\theta & \sin\theta \\ -\frac{\sin\theta}{r} & \frac{\cos\theta}{r} \end{pmatrix}. \tag{3.21}$$

To confirm the theory, Dai et al. performed finite-element simulations. The numerical results of temperature distribution are shown in Fig. 3.2. Fig. 3.3 illustrates the velocity distribution and Fig. 3.4 is for the thermal flux distribution.

So far, they have not taken natural convection into consideration, where the flow is driven by density difference in the field of gravity. When considering the effect of buoyancy, gravitational acceleration $\vec{g}$ should be added in the Darcy law

$$\vec{v} = -\frac{\beta}{\eta}(\nabla p - \rho_f \vec{g}). \tag{3.22}$$

It seems quite difficult to transform $\vec{g}$ to satisfy the requirement of form-invariance. However, the accuracy of cloak, concentrator and rotator can still be evaluated when considering $\vec{g}$. Here $\vec{g}$ is along the $-y$ direction, and no pressure difference is applied on any boundary with no-flux condition set on the two vertical boundaries. They presented the

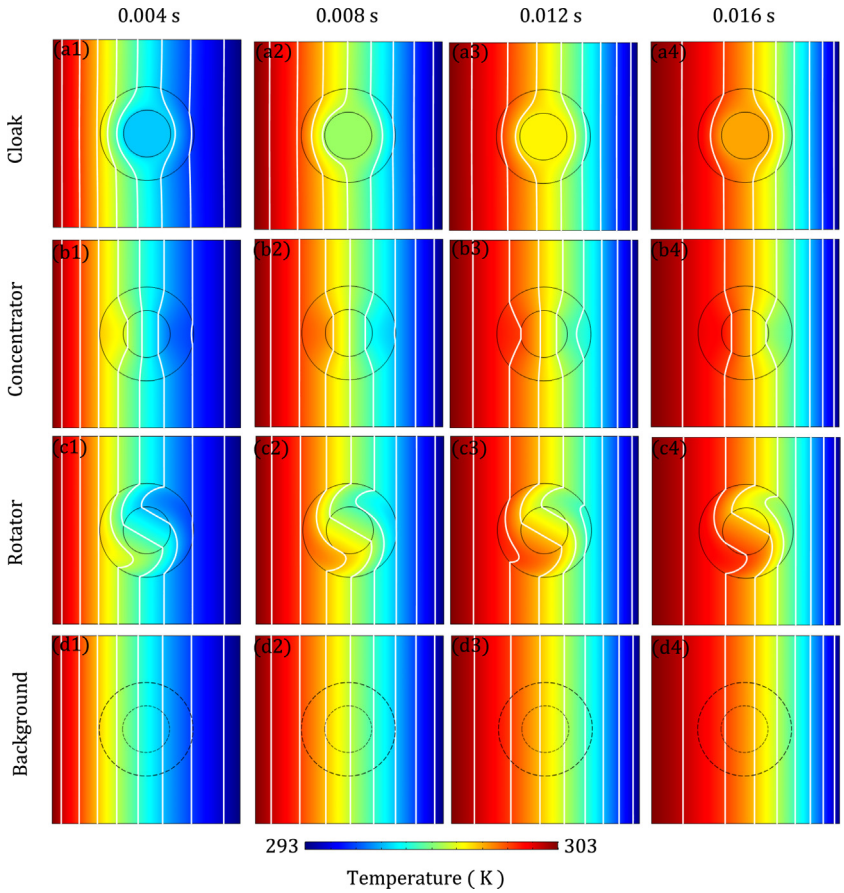

Fig. 3.2. Simulation results of temperature distribution for forced convection. The white lines represent isotherms. The first row (a1–a4) shows the temperature distributions of a thermal cloak at time $t = 0.004$ s, $t = 0.008$ s, $t = 0.012$ s and $t = 0.016$ s. Similarly, (b1–b4) shows those of a thermal concentrator, (c1–c4) shows those of a thermal rotator, and (d1–d4) shows those of the background.
Source: Adapted from Ref. [120].

simulation results of temperature, velocity and heat flux in Figs. 11–13 of Ref. [120], respectively, which illustrates the corresponding distributions for the cloak, concentrator, rotator and background.

When the density of fluid changes more drastically, one must consider other methods to control heat flux in natural or mixed convection, such as various optimization techniques for controlling flows [121,129–131].

It can be seen that the main difficulty for controlling thermal convection (with conduction) lies in the control of mass flow. Recently, researchers designed another series of hydrodynamic metamaterials for the Stokes flows based on the transformation theory, and fabricated them with microfluidics devices to realize anisotropic dynamic viscosity [132,133]. The simulation and experimental results of the hydrodynamic metamaterial cloak and rotator are shown in Figs. 3.5–3.6, respectively. They fabricated microscopic metamaterials in a microfluidic device, and added fluorescent substance to the fluid to observe the flow.

Their research implies that transforming dynamic viscosity can be used to achieve the same effect as transforming permeability in porous media. What is more, by combining the existing method to fabricate anisotropic thermal conductivities, one can expect thermal metamaterials for convection to be experimentally realized in the near future. Actually, if the convective part of heat flux is much larger than the conductive part, one can say, for example, a fluid-flow cloak is approximately a (convective) thermal cloak. This is because now only velocity is required to be transformed for both heat and mass transfer. Again, it must be emphasized that most of the studies mentioned above [119,120,132,133] are restricted to small Reynolds numbers (usually smaller than 1) and some [132,133] can be incorporated into the framework of lubrication theory or the Hele-Shaw flow since the depth of flows is much smaller than the size of the other dimensions. There are still many challenges for both larger Reynolds numbers and more general three-dimensional flows, and a feasible route might rely on optimization algorithms.

3.1.2. Thermal wave

Last but not least, recently two researchers [134–136] proposed a framework of complex thermotics for dealing with conduction and convection (advection). In detail, it is known that conduction and convection are two fundamental

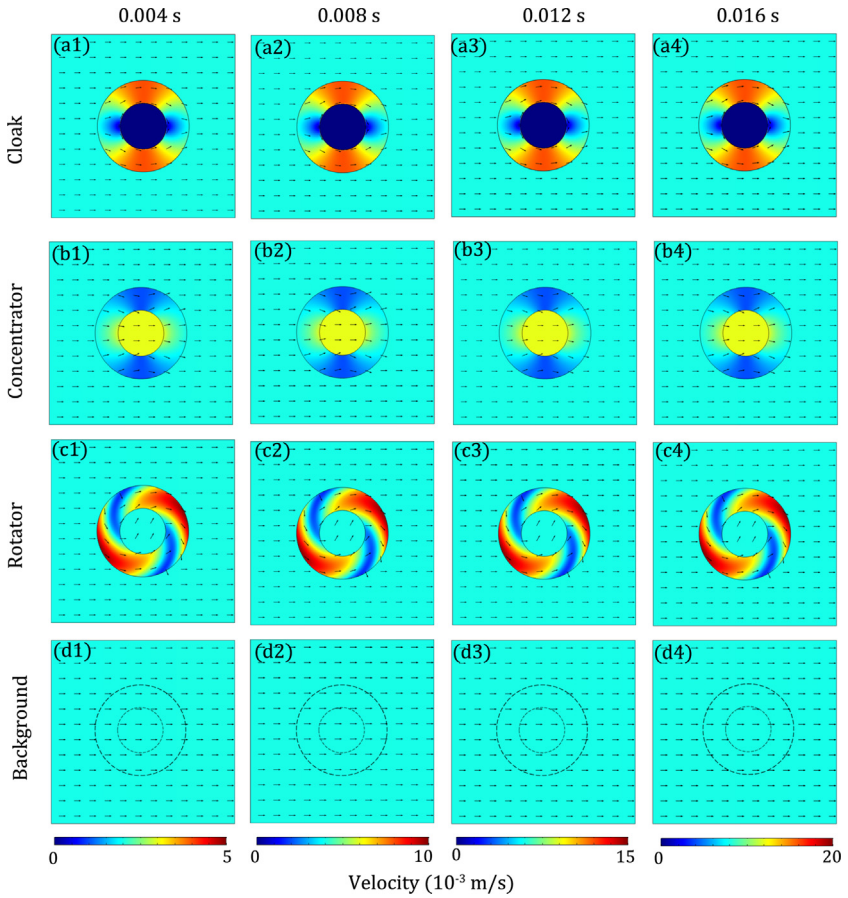

Fig. 3.3. Simulation results of velocity distribution for forced convection. The color surface represents the value of speed, and the black arrows represent the directions of velocities. Again, the row (a1–a4) shows the velocity distributions of a thermal cloak at time $t = 0.004$ s, $t = 0.008$ s, $t = 0.012$ s and $t = 0.016$ s. (b1–b4), (c1–c4) and (d1–d4) show those of a concentrator, a rotator, and the background, respectively.
Source: Adapted from Ref. [120].

methods of heat transfer, which are always considered to be independent. They managed to unify them by coining a complex thermal conductivity whose real and imaginary parts are related to conduction and convection (advection), respectively. Then, the conduction–convection process with thermal waves is dominated by the complex conduction equation, thus called complex thermotics. Further, they established the theory of transformation complex thermotics by both proving the form-invariance of the complex conduction equation and deriving the transformation principle of complex thermal conductivities. As applications, they also designed three devices for cloaking, concentrating, and rotating thermal waves. Moreover, they also suggested experimental demonstrations with a porous medium whose effective complex thermal conductivity can be calculated with the approach of weighted average. These findings could broaden the fundamental knowledge of conduction and convection, and have relevance in designing thermal metamaterials for controlling conduction and convection together.

3.2. Other methods

3.2.1. Zero-index cloak

Besides the transformation theory, metamaterial based on the scattering-canceling theory can also be realized in convective systems. Researchers attempted to manipulate heat transfer in the Darcy flow and used a core–shell structure to design thermal function including transparency, concentrating, and cloaking [137] in convection–conduction (convection–diffusion) systems. The values of thermal conductivity and permeability were obtained for homogeneous materials by solving the Darcy law, the conservation law of fluid motion, and the convection–diffusion equation. Also, dynamic viscosity can be modulated instead of permeability. For the incompressible fluid, the Darcy law and the continuity equation just give the Laplace equation for pressure, so the Darcy flows (and the Hele-Shaw flows) are potential flows and the scattering-canceling theory used here can also be applied to regulate the fluid flow individually. Yeung et al. proposed

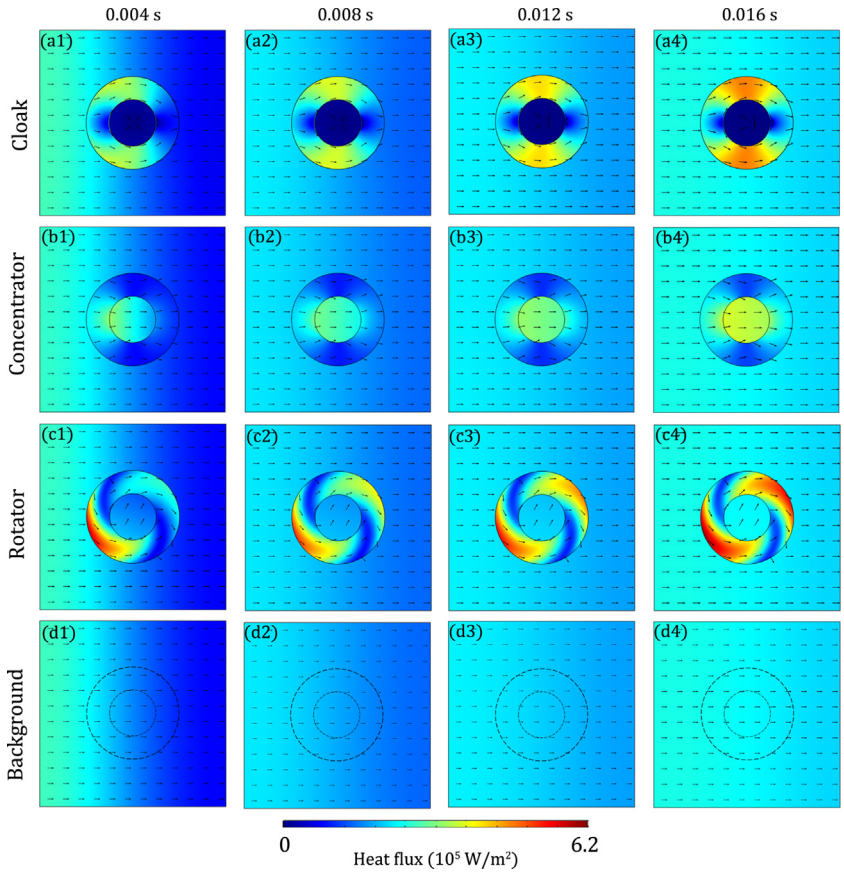

Fig. 3.4. Simulation results of heat flux distribution for forced convection. The value of heat flux is displayed by the color surface, and the black arrows here represent the directions of heat flux. The row (a1–a4) shows the heat flux distribution of a thermal cloak at time $t = 0.004$ s, $t = 0.008$ s, $t = 0.012$ s and $t = 0.016$ s. (b1–b4), (c1–c4) and (d1–d4) are for the concentrator, rotator and background, respectively.
Source: Adapted from Ref. [120].

a kind of thermal and hydrodynamic cloak using only isotropic materials [138], which provides a convenient method for the follow-up research; see Fig. 3.7.

On the other hand, convection can also bring some novel phenomena for designing new thermal devices whose functions cannot be realized only through conduction. For example, it is known that convective systems can have much higher heat dissipation efficiency than conductive ones, and related devices like heat pipes and vapor chambers have been widely used in heat management. Such a difference in heat dissipation comes from the fact that convective heat flux is proportional to the velocity, so an infinite effective conductivity might be achieved in convection. Based on this idea, Li et al. proved that thermal zero-index means an infinite thermal conductivity and designed a bilayer structure to shield an object [68].

The zero-index cloak in Ref. [68] is similar to a bilayer cloak in conduction while the parameters come from the solution of convection–diffusion equation, and the inner layer with infinite effective thermal conductivity is a channel in which water circulates around the object. Another main difference from the conduction cloaks is that the interior temperature inside the zero-index cloak is sensitive to environmental changes. In the experiment, the rotating water can be regarded as an inner layer, which is the key to an effectively infinite thermal conductivity. The background and outer layer are composed of copper. The experimental setup and results can be found in Fig. 3.8. Interestingly, Li et al. [68] provided an effective approach to breaking the upper limit of thermal conductivities of naturally occurring materials, and can be applied to control heat transfer with high efficiency.

Convective systems can also be made of only solid components if at least one component is moving or deformed. When convective term competes with the diffusive nature of conduction, some novel phenomena can be revealed. Non-Hermitian quantum physics related to parity-time symmetry [139] has become an important topic in the past two decades. However, almost all the studies focused on open wave systems with energy exchange, and diffusion systems are seldom touched. A recent work found that, in a diffusion heat transfer system including two coupled solid rings rotating with equal-but-opposite speed, anti-parity-time symmetry is broken when the rotation speed is larger than the exceptional

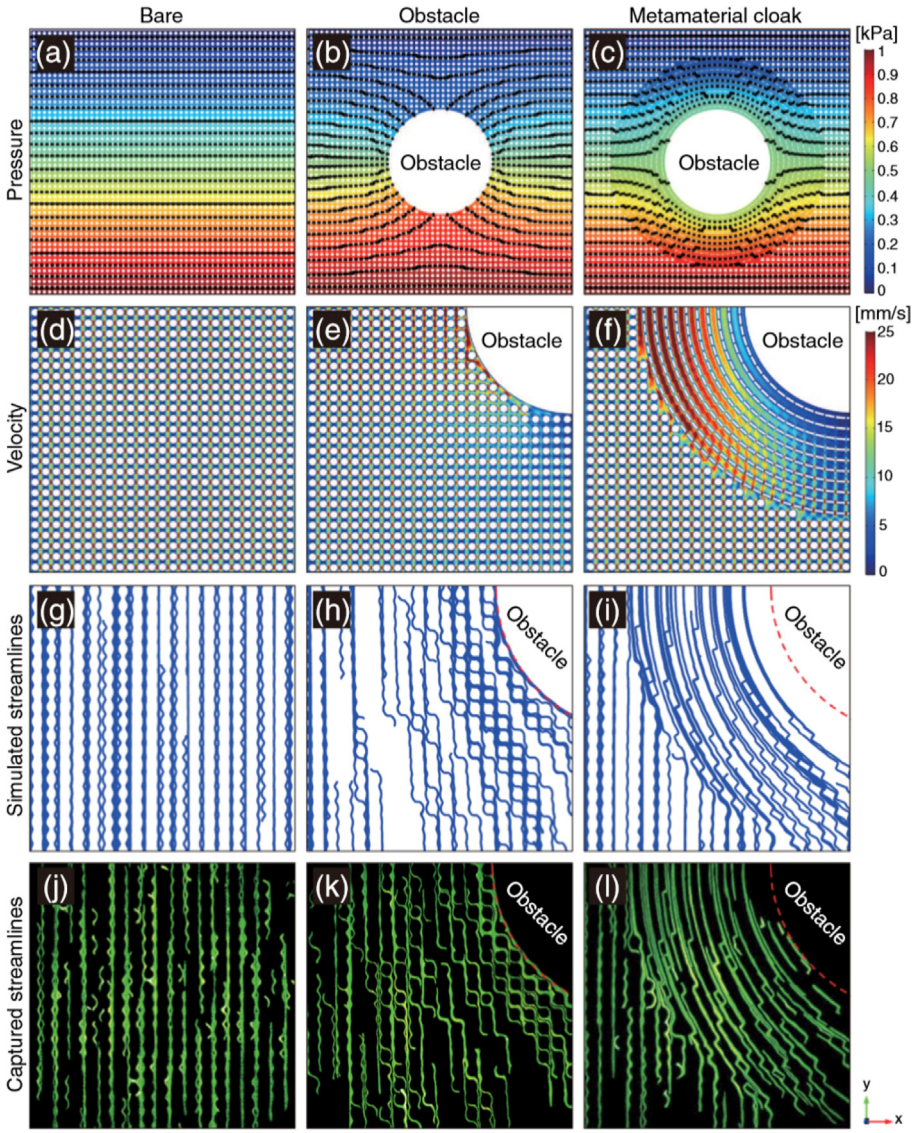

Fig. 3.5. Simulation and experimental results of the hydrodynamic metamaterial cloak. Simulation results for bare, obstacle, and metamaterial cloak of (a)–(c) pressure fields, (d)–(f) velocity fields, (g)–(i) streamlines. (j)–(l) are the experimental results for bare background, obstacle, and metamaterial cloak, respectively.
Source: Figure reprinted with permission from Park et al. Phys. Rev. Lett., 123, 074502, 2019.

point [140]. The dynamic equation of the system can be written as the Schrödinger equation with a two-level non-Hermitian–Hamiltonian, where "quantum state" represents the temperature distributions of the two rings. This phase transition of anti-parity-time symmetry at the exceptional point can be shown by the switch from motionless temperature profiles (symmetric) to moving profiles (asymmetric) of the two rings.

The diffusion process is dominated by

$$\begin{cases} \frac{\partial T_1}{\partial t} = D\left(\frac{\partial^2 T_1}{\partial x^2} + \frac{\partial^2 T_1}{\partial z^2}\right) - u\frac{\partial T_1}{\partial x}, & w_i/2 \le z \le w_i/2 + w \\ \frac{\partial T_i}{\partial t} = D_i\left(\frac{\partial^2 T_i}{\partial x^2} + \frac{\partial^2 T_i}{\partial z^2}\right), & -w_i/2 < z < w_i/2 \\ \frac{\partial T_2}{\partial t} = D\left(\frac{\partial^2 T_2}{\partial x^2} + \frac{\partial^2 T_2}{\partial z^2}\right) + u\frac{\partial T_2}{\partial x}, & -w_i/2 - w \le z \le -w_i/2 \end{cases}, \tag{3.23}$$

where D is the diffusivity of the upper and lower rings, and D_i is that of the intermediate layer. The thicknesses of the two moving rings and intermediate layer are denoted as w and w_i, respectively.

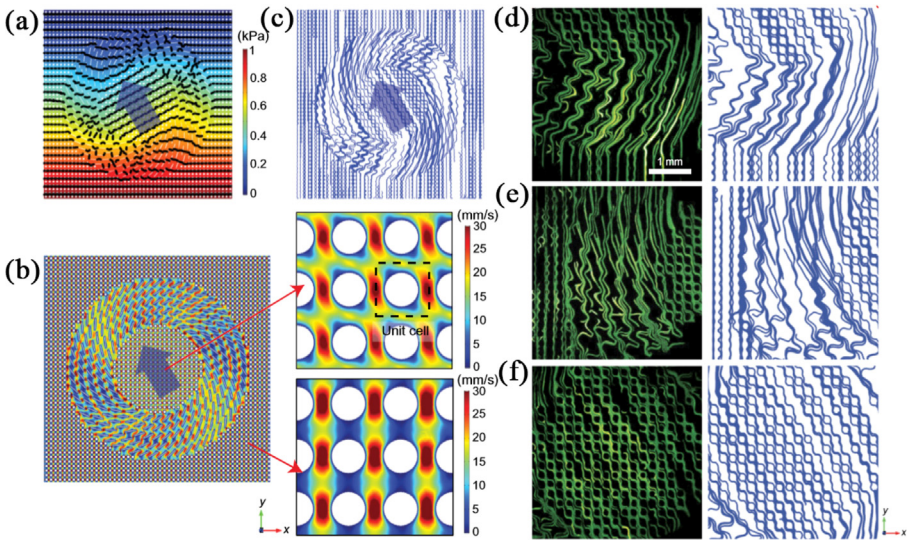

Fig. 3.6. Simulation and experimental results of the hydrodynamic metamaterial rotator. Simulation results of (a) pressure fields, (b) velocity fields, (c) flow streamlines. Experimental results in (d) the entrance region, (e) the left-side region, (f) the central region.
Source: Figure reproduced with permission from Park et al. Phys. Rev. Applied, 12, 061002, 2019.

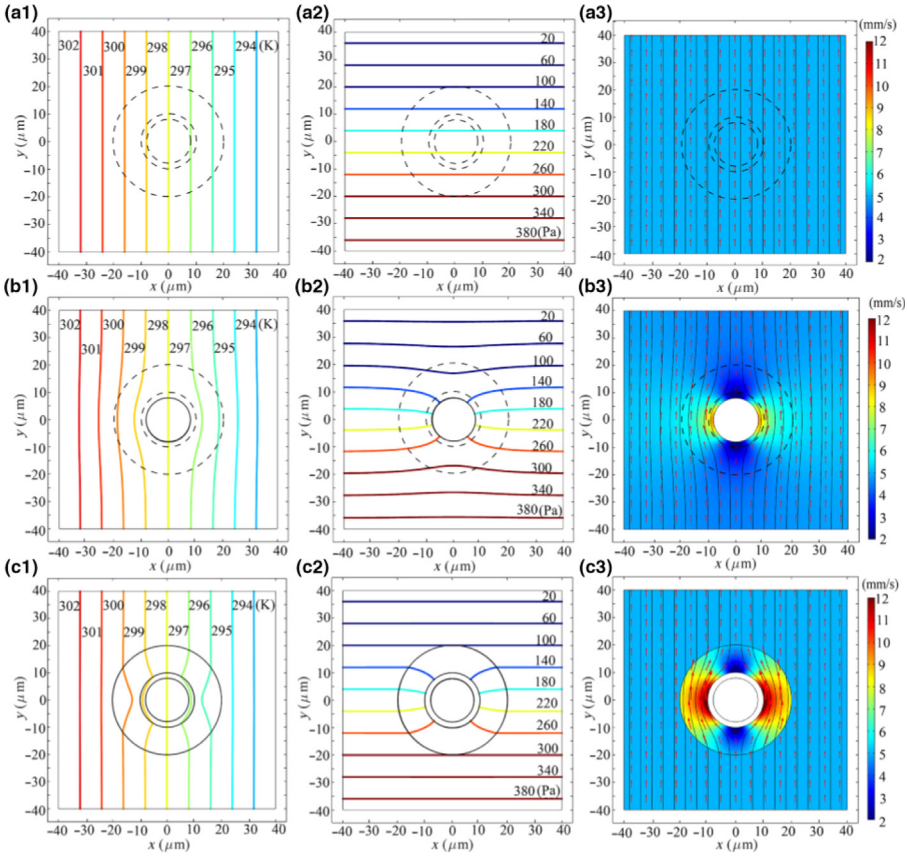

Fig. 3.7. Simulation results of the thermal and hydrodynamic cloak. (a) Bare background. (b) Bare background with obstacle. (c) Bare background with obstacle and cloak. (a1–c1), (b2–c2), and (a3–c3) displayed isotherms, isobars, and streamlines, respectively.
Source: Figure reprinted with permission from Yeung et al. Phys. Rev. Applied, 13, 064030, 2020.

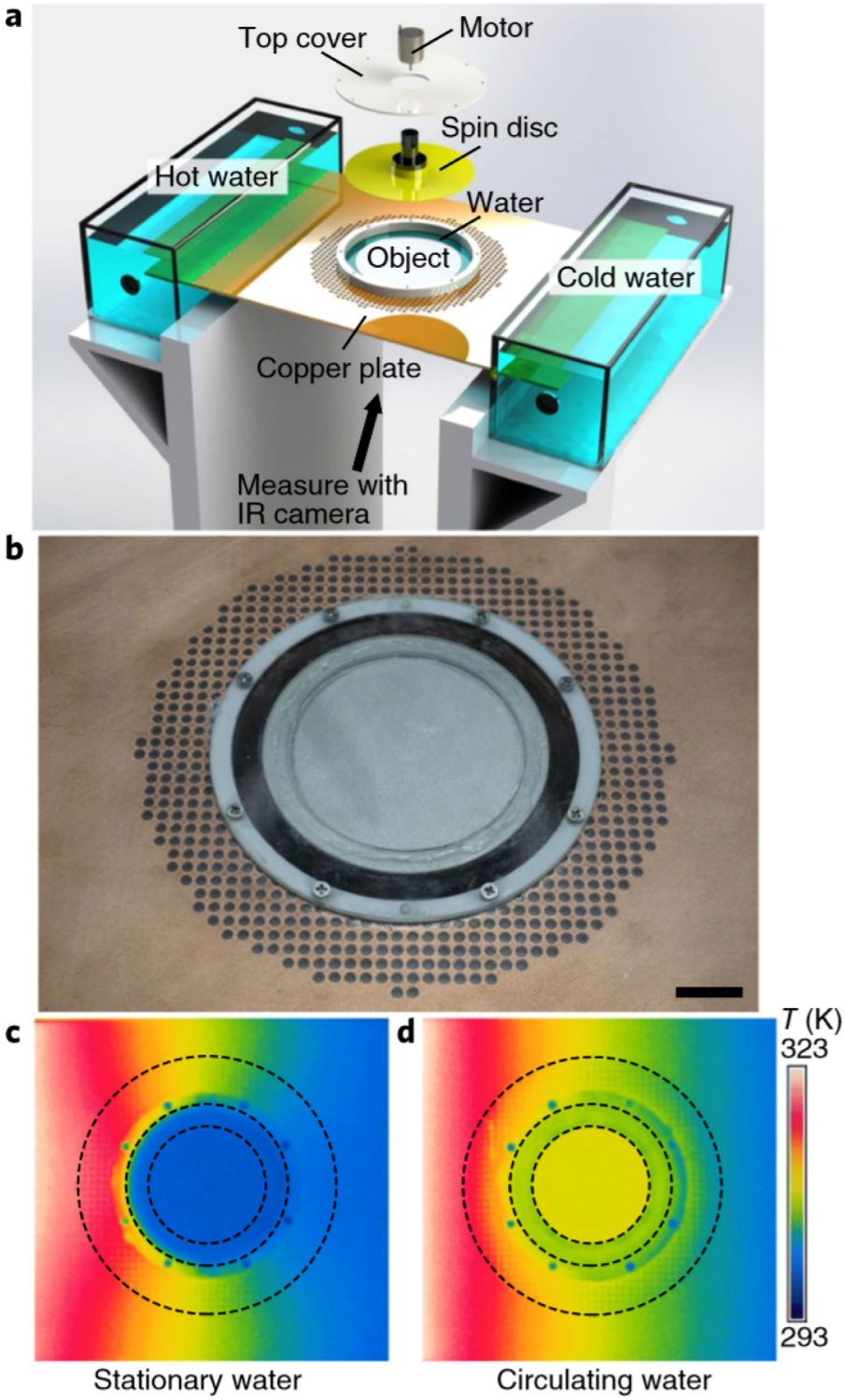

Fig. 3.8. (a) Schematic diagram of the experimental set-up. (b) Picture of the sample. (c) Experimental results when the water is motionless. (d) Experimental results when the water is rotating.
Source: Figure reprinted with permission from Li et al. Nat. Mater., 18, 48–54, 2019.

It is reasonable to suppose that the temperature variance along z axis is negligible ($\partial^2 T/\partial z^2 = 0$) as a quasi one-dimensional model. Heat energy can exchange between the two moving rings through the intermediate layer. Therefore, the middle equation of Eq. (3.23) can be replaced by two source terms, say, s_1 for the upper ring and s_2 for the lower ring. Then,

$$\begin{cases} \frac{\partial T_1}{\partial t} = D\frac{\partial^2 T_1}{\partial x^2} - u\frac{\partial T_1}{\partial x} + \frac{s_1}{\rho c}, & w_i/2 \le z \le w_i/2 + w \\ \frac{\partial T_2}{\partial t} = D\frac{\partial^2 T_2}{\partial x^2} + u\frac{\partial T_2}{\partial x} + \frac{s_2}{\rho c}, & -w_i/2 - w \le z \le -w_i/2 \end{cases}, \tag{3.24}$$

where the density-heat capacity products of the upper and lower rings are the same, denoted as ρc.

The boundary conditions are given by the continuities of temperatures and heat fluxes,

$$\begin{cases} T_1 = T_i, & z = w_i/2 \\ T_2 = T_i, & z = -w_i/2 \\ j_1 = -\kappa_1\frac{\partial T_1}{\partial z} = -\kappa_i\frac{\partial T_i}{\partial z}, & z = w_i/2 \\ j_2 = \kappa_2\frac{\partial T_2}{\partial z} = \kappa_i\frac{\partial T_i}{\partial z}, & z = -w_i/2 \end{cases}, \tag{3.25}$$

where j_1 and j_2 are heat fluxes to the upper and lower rings, respectively. κ_1, κ_2, and κ_i are the thermal conductivities of the upper ring, lower ring, and intermediate layer, respectively.

Since the higher order terms ($\partial^2 T/\partial z^2 = 0$) is neglected, T_i is linear along z axis, yielding $\partial T_i/\partial z = (T_1 - T_2)/w_i$. Meanwhile, w is small enough, so the two sources (s_1 and s_2) are uniformly distributed along the ring width, say, $s_1 = j_1/w = -\kappa_i(T_1 - T_2)/(ww_i)$ and $s_2 = j_2/w = -\kappa_i(T_2 - T_1)/(ww_i)$. Then, Eq. (3.24) can be reduced to

$$\begin{cases} \frac{\partial T_1}{\partial t} = D\frac{\partial^2 T_1}{\partial x^2} - u\frac{\partial T_1}{\partial x} + h\left(T_2 - T_1\right), & w_i/2 \le z \le w_i/2 + w \\ \frac{\partial T_2}{\partial t} = D\frac{\partial^2 T_2}{\partial x^2} + u\frac{\partial T_2}{\partial x} + h\left(T_1 - T_2\right), & -w_i/2 - w \le z \le -w_i/2 \end{cases}, \tag{3.26}$$

where $h = \kappa_i/(\rho c w w_i)$ is the exchange rate of heat energy between the two moving rings.

Then, plane-wave solutions are introduced,

$$\begin{cases} T_1 = A_1 e^{i(kx-\omega t)} + T_0 \\ T_2 = A_2 e^{i(kx-\omega t)} + T_0 \end{cases}, \tag{3.27}$$

where A_1 (or A_2) is the temperature amplitude in the upper (or lower) ring, k is wave number, ω is frequency, and T_0 is reference temperature.

The substitution of Eq. (3.27) into Eq. (3.26) yields

$$\begin{cases} \omega A_1 = -ik^2 DA_1 + kuA_1 + ih\left(A_2 - A_1\right), & w_i/2 \le z \le w_i/2 + w \\ \omega A_2 = -ik^2 DA_2 - kuA_2 + ih\left(A_1 - A_2\right), & -w_i/2 - w \le z \le -w_i/2 \end{cases}. \tag{3.28}$$

Eq. (3.28) can also be expressed as

$$\hat{\boldsymbol{H}}|\boldsymbol{\psi}\rangle = \omega|\boldsymbol{\psi}\rangle, \tag{3.29}$$

where $|\boldsymbol{\psi}\rangle = [A_1, A_2]^\tau$ is eigenstate, and τ denotes transpose. The Hamiltonian $\hat{\boldsymbol{H}}$ reads

$$\hat{\boldsymbol{H}} = \begin{bmatrix} -i\left(k^2 D + h\right) + ku & ih \\ ih & -i\left(k^2 D + h\right) - ku \end{bmatrix}. \tag{3.30}$$

The eigenvalue of the Hamiltonian [Eq. (3.30)] takes on the form

$$\omega_\pm = -i\left[\left(k^2 D + h\right) \pm \sqrt{h^2 - k^2 u^2}\right]. \tag{3.31}$$

As u varies, the system exhibits two different properties, and the point $u_{EP} = h/k$ serves as an exceptional point.

For $u < u_{EP}$, the corresponding eigenstates are

$$|\boldsymbol{\psi}_+\rangle = \left[1,\ e^{i(\pi-\alpha)}\right]^\tau,\ |\boldsymbol{\psi}_-\rangle = \left[1,\ e^{i\alpha}\right]^\tau, \tag{3.32}$$

where $\alpha = \sin^{-1}(ku/h)$. Therefore, the temperature profiles maintain a constant phase difference and decay without motion.

For $u = u_{EP}$, the difference between ω_+ and ω_- disappears and two eigenstates possess the same phase difference of $\pi/2$ and also decay without motion.

For $u > u_{EP}$, the corresponding eigenstates become

$$|\boldsymbol{\psi}_+\rangle = \left[e^{-\delta},\ e^{i\pi/2-2\delta}\right]^\tau,\ |\boldsymbol{\psi}_-\rangle = \left[e^{-\delta},\ e^{i\pi/2}\right]^\tau, \tag{3.33}$$

where $\delta = \cosh^{-1}(ku/h)$. Therefore, two eigenstates maintain a phase difference of $\pi/2$ but decay with motion.

They also carried out experiments to confirm their theory, which indicates that anti-parity-time symmetry can be achieved in diffusion systems indeed, the experimental setup can be seen in Fig. 3.9. The key point of their results lies in the competition between heat conduction and convection.

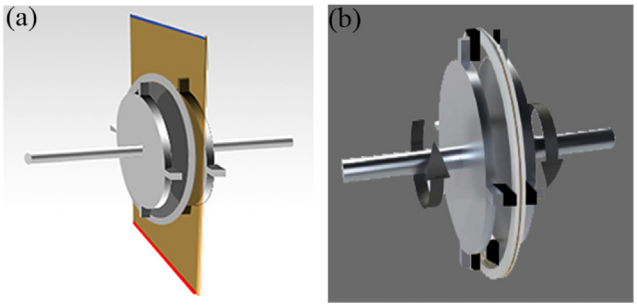

Fig. 3.9. (a–b) Schematic of the experimental setup.

Their work provides an interesting route to both studying parity-time related physics in diffusion frameworks like convection–conduction systems and developing potential methods to control heat and mass transfer. It is worth noting that higher-order exceptional points were reported recently in a similar diffusion system [141]. Similar extension was also attempted for macroscopic convection–diffusion systems. Following Li et al. [140], researchers studied two moving rings with equal-but-opposite velocities, joined together by a stationary intermediate layer [142]. They firstly confirmed an exceptional point of velocity which separates a stationary temperature profile and a moving one. They then investigated a cyclic path of time-varying velocity containing the exceptional point, and an extra phase difference of appears (say, the geometric phase). They finally revealed the mechanism of effective conductivity enhancement, which helps design an invisibility cloak. These results broaden the scope of geometric phase and effective conductivity enhancement, which have potential applications in thermal management. Although these explorations were conducted in a heat transfer system, the corresponding conclusions are general for other convection–diffusion systems such as mass transfer. Therefore, researchers also conducted similar explorations in particle diffusion systems [143]. Certainly, there are also obvious differences between heat transfer and particle diffusion. For the former, it is essentially related to energy transport; for the latter, it is essentially associated with mass transport. The application scope can also be extended to chemical reactions, fuel cells, drug delivery, and catalysis with the efforts in particle diffusion systems.

3.2.2. Thermal convection–conduction crystal

Finally, it is necessary to mention a most recent work on thermal convection–diffusion (convection–conduction) crystals, which can be used to manipulate wave-like temperature profiles [144]. In particular, it is known that periodic structures have crucial applications in wave systems, such as atomic crystals, photonic crystals, and phononic crystals. In Ref. [144], the authors extend the related physics from wave systems to convection–diffusion systems and propose the concept of thermal convection–diffusion crystals, referring to a periodic porous medium with moving fluids. Phenomenally speaking, only the temperature profiles with allowed frequencies can propagate stably in the thermal convection–diffusion crystal, and those with forbidden frequencies have to change their frequencies for stable propagation. As a model application of thermal convection–diffusion crystals, they further designed a thermal-frequency modulator to control wave-like temperature profiles. Their results might broaden the application realm of periodic structures in convection–diffusion systems and enlighten further development of thermal management and thermal metamaterials with the help of thermal convection–diffusion crystals.

3.2.3. Negative thermal transport

The concept of negative refractive index has drawn much attention due to its unique properties and practical applications in (electromagnetic) wave systems [1–3,145,146]. To promote the related physics in thermotics (diffusion systems), most recently some researchers [134] managed to coin a complex thermal conductivity whose imaginary part corresponds to the real part of complex refractive index. Therefore, the thermal counterpart of negative refractive index (namely, negative real part of complex refractive index) is just negative imaginary part of complex thermal conductivity. This is featured by the opposite directions of energy flow and wave vector in thermal conduction and advection, thus called negative thermal transport. To avoid violating causality, they designed an open system with energy exchange and explored three different cases to reveal negative thermal transport. They further provided experimental suggestions with a solid ring structure. All finite-element simulations agree with theoretical analyses, indicating that negative thermal transport is physically feasible. Their results have potential applications, such as designing the inverse Doppler effect in thermal conduction and advection.

In fact, many other novel phenomena can also appear in thermal conduction–convection systems, say, thermal chameleon-like behavior in microfluidics [147], and so on. This fact implies that thermal conduction–convection systems can be a good model system for producing novel physics, partly because convection provides an additional degree of freedom for controlling the flow of heat in conduction process.

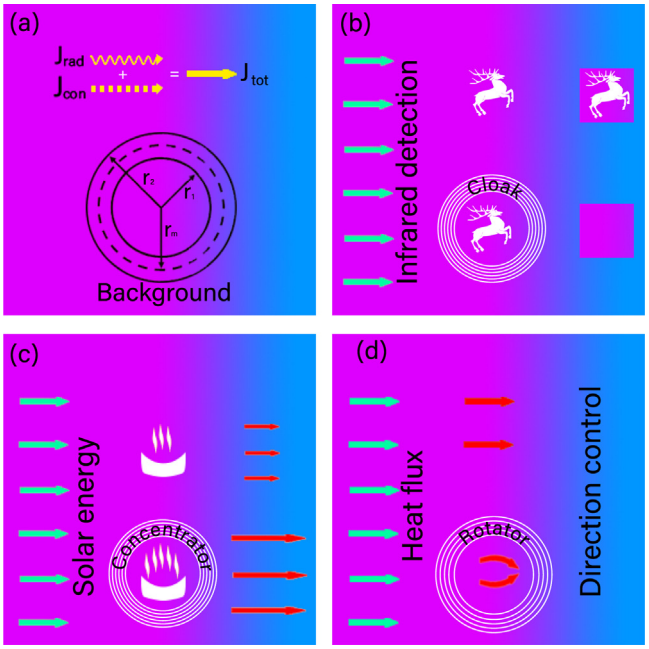

Fig. 4.1. Schematic graphs. (a) The illustration of multithermotics. Wavy arrow, dashed arrow, and solid arrow represent radiative flux, conductive flux, and total flux, respectively. (b) The illustration of cloaking. (c) The illustration of concentrating. (d) The illustration of rotating. The color surface indicates the thermal field (temperature distribution).

4. Controlling heat conduction and radiation

4.1. Transformation method

4.1.1. Cloak, concentrator, and rotator

By now, radiation has not been touched yet, while it exists almost everywhere. Although many different models beyond the Stefan–Boltzmann law for near-field or far-field radiation have been studied, a transformation theory for dealing with radiation and other heat transfer modes like conduction was absent in a long time. Xu et al. [148] studied a model case including both radiation and conduction based on the Rosseland diffusion approximation which can be seen as a perturbation of black body radiation [149]. The Rosseland diffusion approximation or the Rosseland radiation model was proposed by Rosseland for optical-thick materials in astrophysics and its applications include mantle radiation [150] and thermal behaviors of insulation materials under high temperatures [151,152]. Here, radiative heat flux is proportional to the temperature gradient just like its conductive counterpart, and gives a radiative part of thermal conductivity related to the cube of temperature and the Rosseland mean opacity.

Xu et al. [148] investigated three temperature intervals in which conductive and radiative heat flux may have different proportions. The theory of transformation multithermotics is established; see Fig. 4.1(a). They further designed three devices including cloaking, concentrating, and rotating as model applications. Cloaking [Fig. 4.1(b)] can protect inside objects from being discovered by infrared detection; concentrating [Fig. 4.1(c)] can enhance the intensity of local heat flux; and rotating [Fig. 4.1(d)] can control the direction of local heat flux. Instead of inhomogeneous and anisotropic materials, they resorted to layered structures (which are composed of two homogeneous and isotropic materials) to simplify fabrication.

Xu et al. considered a transient process of heat transfer including thermal radiation and conduction. Based on the Rosseland diffusion approximation [153], radiative flux can be written as $\boldsymbol{J}_{rad}$ $\left(=-16/3\boldsymbol{\beta}^{-1}\boldsymbol{n}^2\sigma T^3\cdot\nabla T\right)$, where $\boldsymbol{\beta}$ is the Rosseland mean attenuation coefficient, $\boldsymbol{n}$ is relative refractive index, σ is the Stefan–Boltzmann constant $\left(=5.67\times10^{-8}\ \mathrm{W\ m^{-2}\ K^{-4}}\right)$, and T denotes temperature. Conductive flux $\boldsymbol{J}_{con}$ $(=-\boldsymbol{\kappa}\cdot\nabla T)$ is given by the Fourier law, where $\boldsymbol{\kappa}$ is thermal conductivity.

Consider a passive heat transfer process, then the dominant equation of multithermotics can be expressed as

$$\rho C\partial T/\partial t+\nabla\cdot(\boldsymbol{J}_{rad}+\boldsymbol{J}_{con})=0, \tag{4.1}$$

where ρ and C are the density and heat capacity of participating media, respectively.

Based on the Jacobian transformation matrix $\boldsymbol{A}$, Eq. (4.1) will keep its form-invariance under a space transformation (from a curvilinear space X to a physical space X').

In view of this, Xu et al. wrote down the component form of Eq. (4.1). In a curvilinear space with a contravariant basis $\{\boldsymbol{g}^u, \boldsymbol{g}^v, \boldsymbol{g}^w\}$, a covariant basis $\{\boldsymbol{g}_u, \boldsymbol{g}_v, \boldsymbol{g}_w\}$, and corresponding contravariant components $\{x^u, x^v, x^w\}$, radiative term can be obtained

$$\begin{aligned}
\nabla\cdot\left(\boldsymbol{\alpha}T^3\cdot\nabla T\right) &= \boldsymbol{g}^w\cdot\frac{\partial}{\partial x^w}\left(\alpha^{uv}T^3\boldsymbol{g}_u\otimes\boldsymbol{g}_v\cdot\boldsymbol{g}^l\frac{\partial T}{\partial x^l}\right)\\
&= \boldsymbol{g}^w\cdot\frac{\partial}{\partial x^w}\left(\alpha^{uv}T^3\boldsymbol{g}_u\frac{\partial T}{\partial x^v}\right)\\
&= \frac{\partial\alpha^{uv}T^3}{\partial x^u}\frac{\partial T}{\partial x^v}+\frac{\partial^2 T}{\partial x^u\partial x^v}\alpha^{uv}T^3+\boldsymbol{g}^w\cdot\frac{\partial\boldsymbol{g}_u}{\partial x^w}\left(\alpha^{uv}T^3\frac{\partial T}{\partial x^v}\right)\\
&= \partial_u\left(\alpha^{uv}T^3\partial_v T\right)+\Gamma^w_{wu}\alpha^{uv}T^3\partial_v T\\
&= \partial_u\left(\alpha^{uv}T^3\partial_v T\right)+\frac{1}{\sqrt{g}}(\partial_u\sqrt{g})\alpha^{uv}T^3\partial_v T\\
&= \frac{1}{\sqrt{g}}\partial_u\left(\sqrt{g}\alpha^{uv}T^3\partial_v T\right),
\end{aligned}\tag{4.2}$$

where $\boldsymbol{\alpha}\left(=16/3\boldsymbol{\beta}^{-1}\boldsymbol{n}^2\sigma\right)$ is the radiative coefficient, and g is the determinant of the matrix with components $g_{ij}=\boldsymbol{g}_u\cdot\boldsymbol{g}_v$. Define the Christoffel symbol as $\Gamma^w_{vu}=\partial\boldsymbol{g}_u/\partial x^v\cdot\boldsymbol{g}^w$, thus resulting in $\Gamma^w_{wu}=\left(\partial_u\sqrt{g}\right)/\sqrt{g}$. Similarly, conductive term can be rewritten as

$$\nabla\cdot(\boldsymbol{\kappa}\cdot\nabla T)=\frac{1}{\sqrt{g}}\partial_u\left(\sqrt{g}\kappa^{uv}\partial_v T\right).\tag{4.3}$$

Then, Eq. (4.1) can be expressed in detail in the curvilinear space.

$$\sqrt{g}\rho C\partial_t T-\partial_u\left(\sqrt{g}\left(\alpha^{uv}T^3+\kappa^{uv}\right)\partial_v T\right)=0,\tag{4.4}$$

So far, they have proved the form-invariance of Eq. (4.1). Then, Eq. (4.1) is rewritten in the physical space to get the transformation rules of material properties, which is usually written in the Cartesian coordinate system $\left\{x^{u'}, x^{v'}, x^{w'}\right\}$,

$$\sqrt{g}\rho C\partial_t T-\partial_{u'}\frac{\partial x^{u'}}{\partial x^u}\left(\sqrt{g}\left(\alpha^{uv}T^3+\kappa^{uv}\right)\frac{\partial x^{v'}}{\partial x^v}\partial_{v'}T\right)=0,\tag{4.5}$$

where $\partial x^{u'}/\partial x^u$ and $\partial x^{v'}/\partial x^v$ are the components of the Jacobian transformation matrix $\boldsymbol{A}$, and $g=\det^{-2}\boldsymbol{A}$. Then, space transformation is replaced with material transformation,

$$\frac{\rho C}{\det\boldsymbol{A}}\partial_t T-\partial_{u'}\left(\left(\frac{A^{u'}_u\alpha^{uv}A^{v'}_v}{\det\boldsymbol{A}}T^3+\frac{A^{u'}_u\kappa^{uv}A^{v'}_v}{\det\boldsymbol{A}}\right)\partial_{v'}T\right)=0.\tag{4.6}$$

Therefore, transformation rules can be written as

$$\begin{aligned}
(\rho C)' &= \rho_0 C_0/\det\boldsymbol{A},\\
\boldsymbol{\alpha}' &= \boldsymbol{A}\boldsymbol{\alpha}_0\boldsymbol{A}^\tau/\det\boldsymbol{A},\\
\boldsymbol{\kappa}' &= \boldsymbol{A}\boldsymbol{\kappa}_0\boldsymbol{A}^\tau/\det\boldsymbol{A}.
\end{aligned}\tag{4.7}$$

ρ_0, C_0, $\boldsymbol{\alpha}_0$, and $\boldsymbol{\kappa}_0$ are the density, heat capacity, radiative coefficient, and thermal conductivity of the background, respectively. $\boldsymbol{A}^\tau$ denotes the transpose of $\boldsymbol{A}$. Radiative coefficient is composed of two physical quantities, say, the Rosseland mean attenuation coefficient and relative refractive index which dominates thermal radiation.

The relative refractive indexes of all regions are set to be 1. Then, considering the transformation rule of the Rosseland mean attenuation coefficient for controlling variables. If the transformation requirement of radiative coefficient is satisfied, the present theory can also be applied to other relative refraction indexes. Then, Eq. (4.7) can be simplified as

$$\begin{aligned}
(\rho C)' &= \rho_0 C_0/\det\boldsymbol{A},\\
\boldsymbol{n}' &= \boldsymbol{n}_0,\\
\boldsymbol{\beta}' &= \boldsymbol{A}^{-\tau}\boldsymbol{\beta}_0\boldsymbol{A}^{-1}\det\boldsymbol{A},\\
\boldsymbol{\kappa}' &= \boldsymbol{A}\boldsymbol{\kappa}_0\boldsymbol{A}^\tau/\det\boldsymbol{A}.
\end{aligned}\tag{4.8}$$

Eq. (4.7)/(4.8) is the key to transformation multithermotics. To perform finite-element simulations, consider Eq. (4.8) for brevity.

Since transformation multithermotics does not restrict space dimensions, Xu et al. designed cloaking, concentrating, and rotating in two dimensions without loss of generality.

To realize the space transformation of cloaking, one should compress a circular region ($r < r_1$) from the center into a shell ($r_1 < r < r_2$), then

$$\begin{aligned} r' &= (r_2 - r_1)\, r/r_2 + r_1, \\ \theta' &= \theta. \end{aligned} \tag{4.9}$$

r_1 and r_2 are the inner and outer radii of the shell, and $0 < r < r_2$ except for additional statements.

To realize the space transformation of concentrating, compress a large circular region ($r < r_m$) into a small one ($r < r_1$) firstly. Then, stretch the small shell ($r_m < r < r_2$) into a large one ($r_1 < r < r_2$), which can be concluded as

$$\begin{aligned} r' &= r_1 r/r_m \text{ for } r < r_m, \\ r' &= \left((r_2 - r_1)\, r + (r_1 - r_m)\, r_2\right)/(r_2 - r_m) \text{ for } r_m < r < r_2, \\ \theta' &= \theta, \end{aligned} \tag{4.10}$$

where r_m is the concentrating ratio.

To realize the space transformation of rotating, one should rotate the core ($r < r_1$) with angle θ_0 and rotate the shell ($r_1 < r < r_2$) as

$$\begin{aligned} r' &= r \\ \theta' &= \theta + \theta_0 \text{ for } r < r_1, \\ \theta' &= \theta + \theta_0\, (r - r_2)/(r_1 - r_2) \text{ for } r_1 < r < r_2, \end{aligned} \tag{4.11}$$

where θ_0 is the rotation angle.

Calculate the Jacobian transformation matrix of Eqs. (4.9)–(4.11) as

$$\boldsymbol{A} = \begin{pmatrix} \partial r'/\partial r & \partial r'/(r\partial\theta) \\ r'\partial\theta'/\partial r & r'\partial\theta'/(r\partial\theta) \end{pmatrix}. \tag{4.12}$$

Then, Xu et al. further performed transient finite-element simulations to validate the theory. Heat transfer equation is rewritten with tensorial parameters in the interface with general partial differential equations.

To present the influence of thermal radiation, they chose three different temperature intervals. In (I) 300–320 K temperature interval, conductive flux is far larger than radiative flux ($\boldsymbol{J}_{con} \gg \boldsymbol{J}_{rad}$) due to the low temperature. In (II) 300–1000 K temperature interval, thermal radiation starts influencing the temperature profile $\boldsymbol{J}_{con} \sim \boldsymbol{J}_{rad}$ as the temperature rises. (III) In 300–3000 K temperature interval, the temperature is very high, thermal radiation becomes the dominant effect, say $\boldsymbol{J}_{con} \ll \boldsymbol{J}_{rad}$. The left and right boundaries are set as different temperature intervals, and the upper and lower boundaries are insulated. Xu et al. set the initial temperature at 300 K. It takes about 100 min, 50 min, and 5 min for the three temperature intervals to reach steady states, respectively. The transient finite-element simulations of cloaking, concentrating, and rotating are shown in Figs. 4.2–4.4, respectively. To be mentioned, 3000 K is reasonable because carbon aerogels can tolerance up to high temperature of 3073 K [154].

The cloaking parameters are set based on Eq. (4.9). The boundary at $r = r_1$ is also set to be insulated to make the cloaking effect clear because any object can be placed in the white regions presented in Fig. 4.2. Furthermore, insulation can avoid the errors resulting form the singular parameters of cloaking. Xu et al. simulated the time evolutions of temperature profiles with three different temperature intervals; see Fig. 4.2(a)–(d), Fig. 4.2(e)–(h), and Fig. 4.2(i)–(l), respectively. Temperature profiles of the background are never distorted over time which indicate that the cloaking performance is excellent .

As required by Eq. (4.10), Xu et al. set the concentrating parameters. The time evolutions of temperature profiles with three preset temperature intervals are shown in Fig. 4.3(a)–(d), Fig. 4.3(e)–(h), and Fig. 4.3(i)–(l), respectively. It can be seen that isotherms in the center are concentrated, and meanwhile, those in the background are not distorted. Therefore, the concentrating effect is achieved.

Xu et al. set the rotation angle to be $\theta_0 = \pi/6$ to realize the direction control of local heat flux based on Eq. (4.11). Fig. 4.4(a)–(d), Fig. 4.4(e)–(h), and Fig. 4.4(i)–(l) illustrate the evolutions of temperature profiles over time with different temperature intervals. In the regions $r < r_1$, the high temperature appears at the left-top corner, indicating that the direction of heat flux is changed, which validate the rotating effect.

It is difficult to obtain the parameters directly because parameters derived from transformation multithermotics are anisotropic (for all functions) and divergent (for only cloaking). To solve this problem, it is imagined that layered structures have different properties along the directions of series connection and parallel connection with the physical image of series–parallel connection. Then, they resorted to the layered structure composed of two isotropic and homogeneous materials to realize effective anisotropy. In other words, the effective parameters of layered structures are the approximation of the theoretical parameters, which are anisotropic as expected.

There are two general principles of structural effects: (I) the more layers, the better; (II) the bigger difference of both thermal conductivities and the Rosseland mean attenuation coefficients between material A and material B, the better. Material parameters are chosen to be around the order of aerogels. A recent study reported that the thermal conductivity of ceramic aerogels can be as low as 0.0024 W m^{-1} K^{-1} [155]. Therefore, the material foundation is well established. In Fig. 5(a), (e), and (i) of Ref. [148], the layered structures of cloaking, concentrating, and rotating are shown, respectively. The corresponding steady results with three different temperature intervals are demonstrated in Figs. 5(b)–(d), (f)–(h), and (j)–(l) of Ref. [148], respectively. These results indicate that the designed structures have good performance.

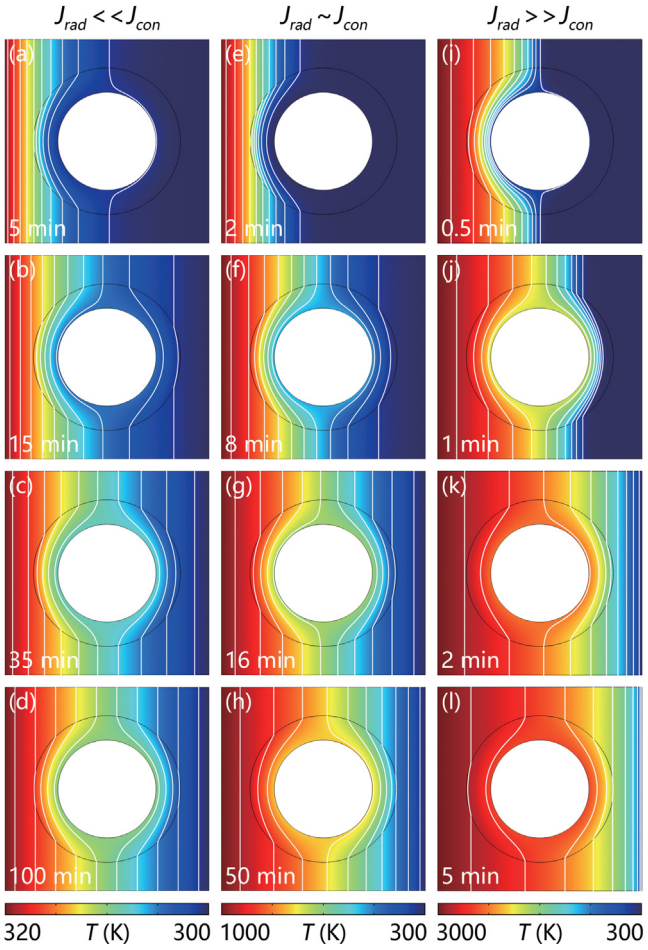

Fig. 4.2. Simulations of cloaking. The size is 10×10 cm^2, $r_1 = 2.4$ cm, $r_2 = 3.6$ cm, and the background parameters are $\rho_0 C_0 = 10^6$ J m^{-3} K^{-1}, $\boldsymbol{n}_0 = 1$, $\boldsymbol{\beta}_0 = 100$ m^{-1}, and $\boldsymbol{\kappa}_0 = 1$ W m^{-1} K^{-1}. The shell parameters are $\boldsymbol{A} = \mathrm{diag}\left[\frac{r_2-r_1}{r_2}, \frac{r_2-r_1}{r_2}\frac{r'}{r'-r_1}\right]$, $(\rho C)' = \left(\frac{r_2}{r_2-r_1}\right)^2 \frac{r'-r_1}{r'} \times 10^6$ J m^{-3} K^{-1}, $\boldsymbol{n}' = 1$, $\boldsymbol{\beta}' = \mathrm{diag}\left[\frac{r'}{r'-r_1}, \frac{r'-r_1}{r'}\right] \times 100$ m^{-1}, and $\boldsymbol{\kappa}' = \mathrm{diag}\left[\frac{r'-r_1}{r'}, \frac{r'}{r'-r_1}\right]$ W m^{-1} K^{-1}. The evolutions over time are demonstrated in (a)–(d), (e)–(h), and (i)–(l), with three different temperature intervals. White lines represent isotherms, and rainbow surfaces denote temperature distributions. *Source:* Adapted from Ref. [148].

Xu et al. only transformed spaces or materials, so transformation multithermotics is exact and robust under other conditions such as complex shapes and nonuniform thermal fields. In addition, thermal radiation in their work is essentially a far-field effect. It is also promising to extend transformation multithermotics to other radiative models [156], such as considering heat flux due to photons or other heat carriers both in near fields and far fields [157–159]. The proposed theory and devices indicate the exotic manipulations of multithermotics. Their work have applications in thermal camouflaging and solar energy utilizing [36,160,161].

Since thermal radiation features T^3 temperature-dependence, it is an excellent candidate of thermally responsive metamaterials [162,163]. Thermally response refers to the behavior that the devices can adjust their temperatures by changing the emissivity [162] or actively turning on or off [163] when the ambient temperature changes. In [163], the modular design of thermally tunable unit cells was proposed, which can realize an®on–off thermal function in response to the temperature conditions. In this mechanism, the phase change of inner materials at the critical temperature is the key point. As an application, researchers used a switchable thermal shield to protect temperature-sensitive devices from the harm of thermal disturbance. Simulations and experiments are designed to validate the theory.

4.1.2. Thermal camouflage

Also, thermal camouflage is an important application of transformation theory and thermal metamaterials, which involves both conduction and radiation. Conventional transformation techniques are usually employed for controlling heat flow in a plane or inside a bulk. However, as thermal signatures can be detected out of plane in most situations, these techniques may be invalid because they cannot be used to conceal the location of actual objects.

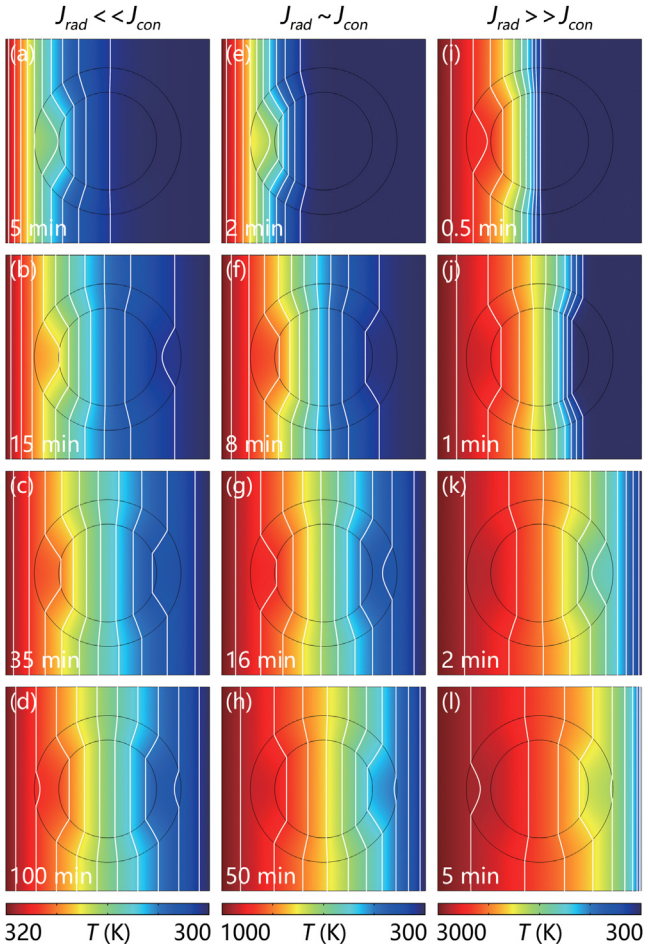

Fig. 4.3. Simulations of concentrating. The background parameters are unchanged. The shell parameters are $\boldsymbol{A} = \mathrm{diag}\left[\frac{r_2-r_1}{r_2-r_m}, \frac{(r_2-r_1)r'}{(r_2-r_m)r'-(r_1-r_m)r_2}\right]$, $(\rho C)' = \frac{(r_2-r_m)^2 r'-(r_2-r_m)(r_1-r_m)r_2}{(r_2-r_1)^2 r'} \times 10^6$ J m^{-3} K^{-1}, $\boldsymbol{n}' = 1$, $\boldsymbol{\beta}' = \mathrm{diag}\left[\frac{(r_2-r_m)r'}{(r_2-r_m)r'-(r_1-r_m)r_2}, \frac{(r_2-r_m)r'-(r_1-r_m)r_2}{(r_2-r_m)r'}\right] \times 100$ m^{-1}, and $\boldsymbol{\kappa}' = \mathrm{diag}\left[\frac{(r_2-r_m)r'-(r_1-r_m)r_2}{(r_2-r_m)r'}, \frac{(r_2-r_m)r'}{(r_2-r_m)r'-(r_1-r_m)r_2}\right]$ W m^{-1} K^{-1} with $r_m = 3.2$ cm.
Source: Adapted from Ref. [148].

Li et al. proposed a novel strategy to regenerate the conductive transformation thermotics for radiative regime [39]. They investigated the existing methods for radiative camouflage and pointed out that tailoring surface temperatures or emissivities were two straightforward methods for tailoring typical infrared imaging. However, the engineered-emissivity approach was background-dependent, thus restricting practical applications. They resorted to the conductive transformation technique and applied it along z axis. In detail, the out-of-plane coordinate transformation was executed twice. First, the background was stretched upwards in order to transfer the original background temperatures of each sites to the top surface. Second, compressing the created space for hiding an actual object inside. By taking the thickness limit of the new space to near-zero, an ultrathin thermal surface was designed for the purpose. They performed experimental demonstration by composing copper and polydimethylsiloxane to layers for achieving anisotropic thermal conductivities according to the transformation theory; see Fig. 4.5. The infrared images and temperature curves showed that the object is totally invisible as if it does not exist inside. This work enabled the compatibility of conductive transformation in radiative fields, enriching the application realm of transformation techniques.

4.2. Other methods

4.2.1. Far-field radiation

Moreover, Xu et al. proposed an effective-medium theory to control conductive and radiative heat transfer. Xu et al. considered a passive and steady process of heat transfer and proved the that total heat flux satisfies the linear Laplace

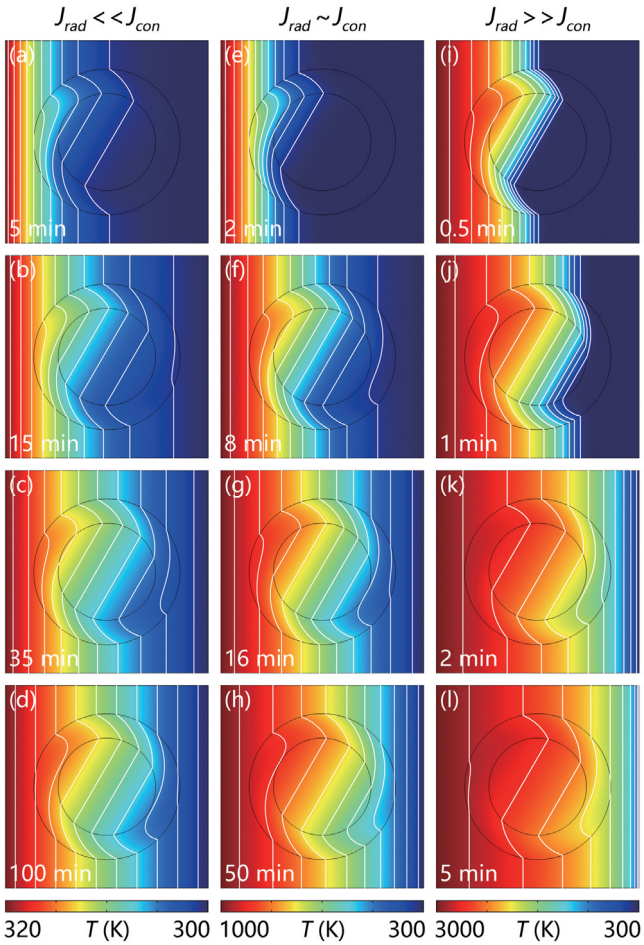

Fig. 4.4. Simulations of rotating. The background parameters are unchanged. The shell parameters are $\boldsymbol{A} = \left[(1,\,0),\,\left(\frac{\theta_0 r'}{r_1-r_2},\,1\right)\right]$, $(\rho C)' = 10^6$ J m^{-3} K^{-1}, $\boldsymbol{n}' = 1$, $\boldsymbol{\beta}' = \left[\left(\left(\frac{\theta_0 r'}{r_1-r_2}\right)^2+1,\,\frac{-\theta_0 r'}{r_1-r_2}\right),\,\left(\frac{-\theta_0 r'}{r_1-r_2},\,1\right)\right] \times 100$ m^{-1}, and $\boldsymbol{\kappa}' = \left[\left(1,\,\frac{\theta_0 r'}{r_1-r_2}\right),\,\left(\frac{\theta_0 r'}{r_1-r_2},\,\left(\frac{\theta_0 r'}{r_1-r_2}\right)^2+1\right)\right]$ W m^{-1} K^{-1} with $\theta_0 = \pi/6$.
Source: Adapted from Ref. [148].

equation after theoretical analyses [98]. They derived the effective thermal conductivity and the radiative coefficient of a core–shell structure by solving the Laplace equation in ellipsoidal coordinates. There are two key parameters which can help to control the process of heat conduction and radiation. Furthermore, they designed three different core–shell radiative metamaterials, including transparency [Fig. 4.6(a)], cloak [Fig. 4.6(b)], and expander [Fig. 4.6(c)]. Finite-element simulations is also applied to validate the theory. These radiative metamaterials are well-behaved in both steady and transient states.

In the condition of a passive and steady process of heat transfer, the total heat flux $\boldsymbol{J}_{total}$ which is composed of the conductive flux $\boldsymbol{J}_{con}$ and the radiative flux $\boldsymbol{J}_{rad}$ is divergency-free,

$$\nabla \cdot \boldsymbol{J}_{total} = \nabla \cdot (\boldsymbol{J}_{con} + \boldsymbol{J}_{rad}) = 0. \tag{4.13}$$

Based on the Fourier law, the conductive flux $\boldsymbol{J}_{con}$ can be written as

$$\boldsymbol{J}_{con} = -\kappa \nabla T, \tag{4.14}$$

where κ is thermal conductivity. The radiative flux $\boldsymbol{J}_{rad}$ is dominated by the Rosseland diffusion approximation,

$$\boldsymbol{J}_{rad} = -\gamma T^3 \nabla T. \tag{4.15}$$

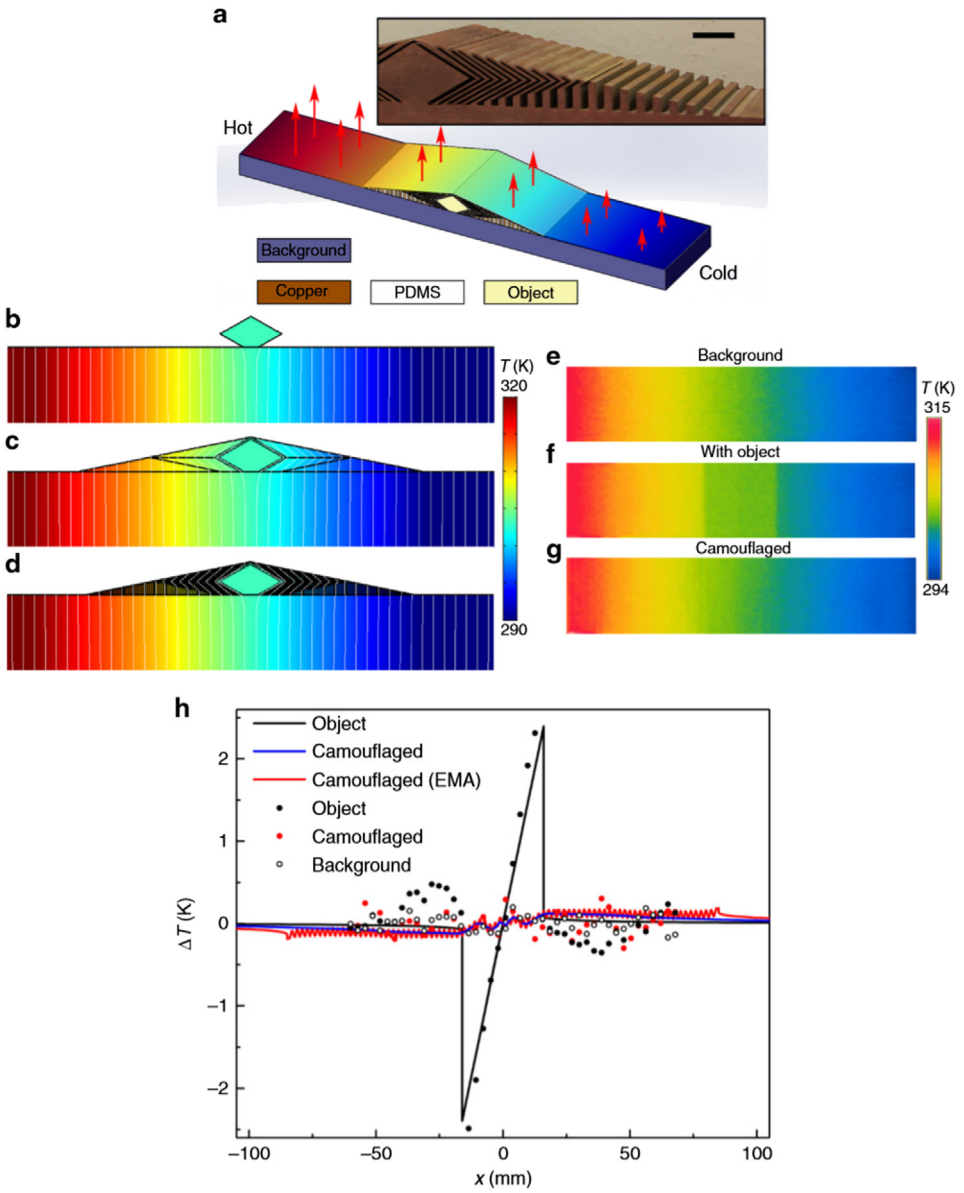

Fig. 4.5. (a) Schematic diagram of the thermal radiation camouflage. Simulation results of (b) object on the upper surface, (c) object covered with the designed cloak, and (d) practical structure. Experimental results of (e) pure background, (f) object on the surface, and (g) objected covered with the designed cloak. (h) Surface temperature deviation ΔT as a function of position x.
Source: Figure reprinted with permission from Li et al. Nat. Commun., 9, 273, 2018.

$\gamma\ \left(=16\beta^{-1}n^2\sigma/3\right)$ is the radiative coefficient, β is the Rosseland mean extinction coefficient, n is relative refraction index, and σ is the Stefan–Boltzmann constant $\left(=5.67\times10^{-8}\,\mathrm{W\,m^{-2}K^{-4}}\right)$.

Considering a three-dimensional core–shell structure which has a core with thermal conductivity κ_c, the Rosseland mean extinction coefficient β_c, and relative refraction index n_c (radiative coefficient γ_c) coated by a shell with corresponding parameters κ_s, β_s, and n_s (radiative coefficient γ_s); see Fig. 4.6(a). The subscript c/s denotes the core/shell. λ_{ci} and λ_{si} $(i=1,\ 2,\ 3)$ are semi-axis lengths of the core and shell, respectively. To realize the same effect of conduction and radiation, define a constant ratio $\alpha=\gamma/\kappa$ of the core–shell structure, say $\gamma_c/\kappa_c=\gamma_s/\kappa_s=\alpha$. Then, Eq. (4.13) can be rewritten as

$$\nabla\cdot\left(-\kappa\nabla T-\alpha\kappa T^3\nabla T\right)=\nabla\cdot\left(-\kappa\left(1+\alpha T^3\right)\nabla T\right)=\nabla\cdot\left(-\kappa\nabla\left(T+\alpha T^4/4\right)\right)=0. \tag{4.16}$$

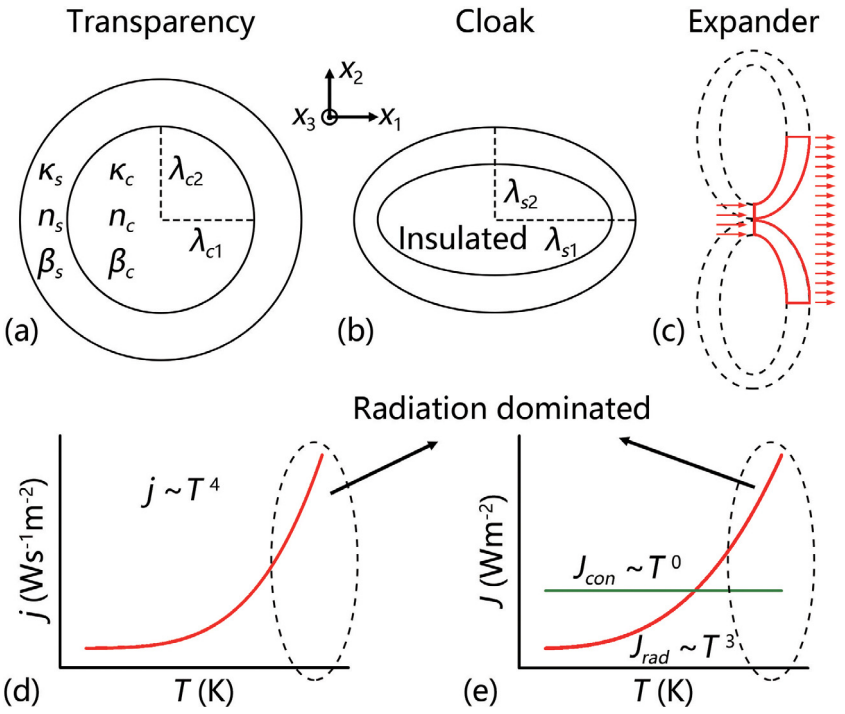

Fig. 4.6. Schematic diagrams of (a) thermal transparency, (b) thermal cloak, and (c) thermal expander. (d) and (e) qualitatively show the radiative emittance j, conductive flux J_{con}, and radiative flux J_{rad} as a function of temperature T.
Source: Adapted from Ref. [98].

The variable substitution $\varphi = T + \alpha T^4/4$ leads to

$$\nabla \cdot (-\kappa \nabla \varphi) = 0. \tag{4.17}$$

Therefore, strong nonlinearity (Eq. (4.13)) becomes a linear one (Eq. (4.17)).

Then, proceed with the derivation in ellipsoidal coordinates $(\rho,\ \xi,\ \eta)$,

$$\begin{cases} \frac{x^2}{\rho+\lambda_1^2} + \frac{y^2}{\rho+\lambda_2^2} + \frac{z^2}{\rho+\lambda_3^2} = 1 \text{ (confocal ellipsoids)} \\ \frac{x^2}{\xi+\lambda_1^2} + \frac{y^2}{\xi+\lambda_2^2} + \frac{z^2}{\xi+\lambda_3^2} = 1 \text{ (hyperboloids of one sheet)} \\ \frac{x^2}{\eta+\lambda_1^2} + \frac{y^2}{\eta+\lambda_2^2} + \frac{z^2}{\eta+\lambda_3^2} = 1 \text{ (hyperboloids of two sheets)} \end{cases}, \tag{4.18}$$

where λ_1, λ_2, and λ_3 are three constants, satisfying $\rho > -\lambda_1^2 > \xi > -\lambda_2^2 > \eta > -\lambda_3^2$. in ellipsoidal coordinates, Eq. (4.17) can be expressed as

$$\frac{\partial}{\partial \rho}\left(g\left(\rho\right)\frac{\partial \varphi}{\partial \rho}\right) + \frac{g\left(\rho\right)}{\rho+\lambda_i^2}\frac{\partial \varphi}{\partial \rho} = 0, \tag{4.19}$$

where $g\left(\rho\right) = \sqrt{\left(\rho+\lambda_1^2\right)\left(\rho+\lambda_2^2\right)\left(\rho+\lambda_3^2\right)}$. Eq. (4.19) can be solved as

$$\varphi = \left(u + v\int_0^{\rho}\left(\rho+\lambda_i^2\right)^{-1} g\left(\rho\right)^{-1} d\rho\right) x_i, \tag{4.20}$$

where u and v are two constants, and x_i $(i = 1,\ 2,\ 3)$ denotes Cartesian coordinates. The temperatures (after variable substitution) of the core, shell, and background are φ_c, φ_s, and φ_b, respectively. Then,

$$\begin{cases} \varphi_c = u_c x_i \\ \varphi_s = \left(u_s + v_s\int_{\rho_c}^{\rho}\left(\rho+\lambda_i^2\right)^{-1} g\left(\rho\right)^{-1} d\rho\right) x_i \\ \varphi_b = u_b x_i \end{cases}. \tag{4.21}$$

Based on the boundary conditions, u_c, u_s, and v_s can be determined. ρ_c and ρ_s can denote the exterior surfaces of the core and shell, where boundary conditions are given by continuities of temperatures and normal heat fluxes, then

$$\begin{cases} u_c = u_s \\ u_b = u_s + v_s \int_{\rho_c}^{\rho_s} \left(\rho + \lambda_i^2\right)^{-1} g\left(\rho\right)^{-1} d\rho \\ u_c = 2v_s\kappa_s \left(\kappa_c - \kappa_s\right)^{-1} g\left(\rho_c\right)^{-1} \\ u_b = 2v_s\kappa_s \left(\kappa_{ei} - \kappa_s\right)^{-1} g\left(\rho_s\right)^{-1} \end{cases}, \tag{4.22}$$

where κ_{ei} is the effective thermal conductivity of the core–shell structure along the direction of x_i. The expression ofκ_{ei} can be directly derived by solving Eq. (4.22). Then, to simplify the complex formula, define the semi-axis lengths of the core λ_{ci} and shell λ_{si} as

$$\begin{cases} \lambda_{ci} = \sqrt{\lambda_i^2 + \rho_c} \\ \lambda_{si} = \sqrt{\lambda_i^2 + \rho_s} \end{cases}, \tag{4.23}$$

where $i = 1,\ 2,\ 3$. Thus, the volume fraction f can be written as

$$f = \lambda_{c1}\lambda_{c2}\lambda_{c3}/(\lambda_{s1}\lambda_{s2}\lambda_{s3}) = g\left(\rho_c\right)/g\left(\rho_s\right). \tag{4.24}$$

Define the shape factor d_{wi} along the direction of x_i as

$$d_{wi} = \frac{\lambda_{w1}\lambda_{w2}\lambda_{w3}}{2} \int_0^{\infty} \left(\tau + \lambda_{wi}^2\right)^{-1} \left(\left(\tau + \lambda_{w1}^2\right)\left(\tau + \lambda_{w2}^2\right)\left(\tau + \lambda_{w3}^2\right)\right)^{-1/2} d\tau, \tag{4.25}$$

where the subscript w can take c or s, representing the shape factor of the core or shell. Thus,

$$\begin{aligned} \int_{\rho_c}^{\rho_s} \left(\rho + \lambda_i^2\right)^{-1} g\left(\rho\right)^{-1} d\rho &= \int_{\rho_c}^{\infty} \left(\rho + \lambda_i^2\right)^{-1} g\left(\rho\right)^{-1} d\rho - \int_{\rho_s}^{\infty} \left(\rho + \lambda_i^2\right)^{-1} g\left(\rho\right)^{-1} d\rho \\ &= 2d_{ci} g\left(\rho_c\right)^{-1} - 2d_{si} g\left(\rho_s\right)^{-1}. \end{aligned} \tag{4.26}$$

Finally, a brief expression for κ_{ei} can be obtained

$$\kappa_{ei} = \kappa_s \left[\frac{f\left(\kappa_c - \kappa_s\right)}{\kappa_s + \left(d_{ci} - fd_{si}\right)\left(\kappa_c - \kappa_s\right)} + 1\right]. \tag{4.27}$$

Xu et al. presented a standard method to calculate the Laplace equation [164]. The shape factors satisfy $d_{w1}+d_{w2}+d_{w3} = 1$. In principle, the effective thermal conductivity of any core–shell structure can be derived with Eq. (4.27). However, Eq. (4.27) is only applicable for the case that the core–shell structure is confocal or concentric. Moreover, Eq. (4.27) can also handle the cylindrical (two-dimensional) cases by taking $\lambda_{w3} = \infty$, thus yielding $d_{w1} = \lambda_{w2}/(\lambda_{w1} + \lambda_{w2})$, $d_{w2} = \lambda_{w1}/(\lambda_{w1} + \lambda_{w2})$, and $d_{w3} = 0$ ($d_{w1} + d_{w2} + d_{w3} = 1$ is still satisfied).

Since γ/κ is a constant, one can get the effective radiative coefficient

$$\gamma_{ei} = \gamma_s \left[\frac{f\left(\gamma_c - \gamma_s\right)}{\gamma_s + \left(d_{ci} - fd_{si}\right)\left(\gamma_c - \gamma_s\right)} + 1\right], \tag{4.28}$$

where γ_{ei} is the effective radiative coefficient of the core–shell structure along the direction of x_i. The effective thermal conductivity and effective radiative coefficient can be predicted by Eqs. (4.27)–(4.28). For realizing the same effect of conduction and radiation, one should keep γ/κ as a constant.

Further, Xu et al. confirmed the theoretical analyses by performing finite-element simulations. As qualitatively shown in Fig. 4.6(d), the Stefan–Boltzmann law indicates that the radiative emittance j is proportional to T^4. In the presence of a same temperature gradient, the conductive flux J_{con} is independent of concrete temperatures, whereas the radiative flux J_{rad} is proportional to T^3, as qualitatively presented in Fig. 4.6(e). Therefore, compared with thermal conduction, thermal radiation is of great significance at high temperatures. To show the temperature effects, three temperature intervals are applied when performing finite-element simulations. (I) 273–313 K, a small upper temperature limit where conduction (Con.) is dominant. (II) 273–673 K, a medium upper temperature limit where conduction and radiation (Rad.) are comparative. (III) 273–4273 K, a large upper temperature limit where radiation is dominant.

Thermal transparency aims to design a shell according to the object, making the temperature profile outside the shell undistorted; see Fig. 4.7.

A thermal cloak can protect an object inside from being detected. The parameters are independent of the object. To design a thermal cloak and keep the heat flux off the object, an insulated layer is required. Then, one can equivalently regard an insulated core as the object plus the insulated layer, say, $\kappa_c = \gamma = 0$. Further, to remove the effect of the insulated core, Xu et al. designed a shell based on Eqs. (4.27)–(4.28). The simulation results are shown in Fig. 4.8(a–c) and Fig. 4.8(d–f). As can be seen from the results, the isotherms are kept off the object, and the heat flux cannot enter the object. Meanwhile, the temperature profiles of the background are not distorted. That is, in this case, the cloaking works indeed.

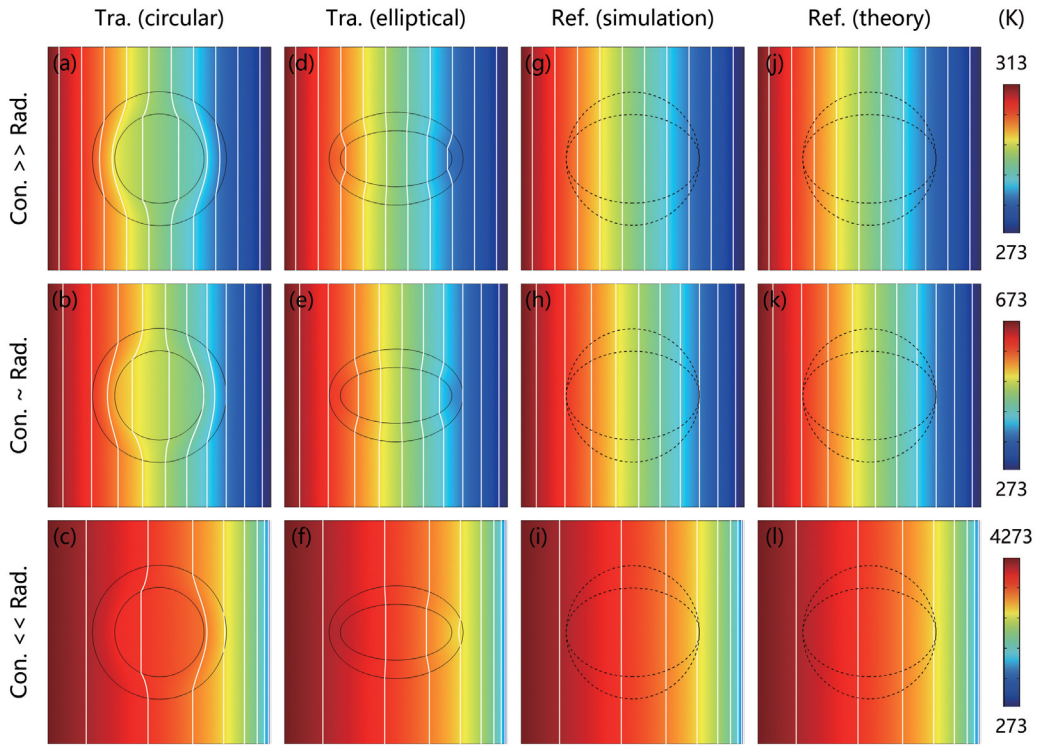

Fig. 4.7. Steady results of thermal transparency. (a)–(c): $\lambda_{c1} = \lambda_{c2} = 2$ cm, $\lambda_{s1} = \lambda_{s2} = 3$ cm, $\kappa_c = 2$ W m^{-1} K^{-1}, $\beta_c = 50$ m^{-1}, $\kappa_s = 0.62$ W m^{-1} K^{-1}, and $\beta_s = 161.1$ m^{-1}. (d)–(f): $\lambda_{c1} = 2.5$ cm, $\lambda_{c2} = 1.25$ cm, $\lambda_{s1} = 3$ cm, $\lambda_{s2} = 2.08$ cm, $\kappa_c = 0.5$ W m^{-1} K^{-1}, $\beta_c = 200$ m^{-1}, $\kappa_s = 1.61$ W m^{-1} K^{-1}, and $\beta_s = 62$ m^{-1}. (g)–(i) are the references with pure background parameters. (j)–(l) are the theoretical temperature distributions of the references. Circular (or elliptical) dashed lines are plotted for the comparison with circular (or elliptical) transparency.
Source: Adapted from Ref. [98].

Based on the design of two elliptical cloaks, thermal expander can enlarge a small source into a large one efficiently. Xu et al. put two elliptical cloaks together, and take out a quarter of the whole structure as an expander; see Fig. 4.6(c). The temperature distribution of the background is not distorted with the uniqueness theorem in thermotics [100], so the expander does work. In Fig. 4.9(a–c), finite-element simulations are presented. The straight isotherms of the background indicate the excellent performance. However, the isotherms of the background are strongly distorted with a pure background material; see Fig. 4.9(d–f). This device is flexible to adjust the source sizes and has applications in uniform heating and effective dissipating.

The above results hold only for the steady states. In fact, these radiative metamaterials can also be extended to transient states if both density and heat capacity are taken into account accordingly. For designing the transient transparency and cloak, Xu et al. set the heat diffusivity $\kappa/(\rho C)$ to be a constant. Although it is an approximate method, its performance is still satisfying. The corresponding results at $t = 10$, 20, 60 mins are presented in Figs. 5(a–c) and (d–f) of Ref. [98], respectively. For designing a transient expander, they adopted the optimization method and set the diffusivity of the shell larger than that of the background to achieve the best transient effect. The corresponding results at $t = 6$, 10, 20 mins are presented in Figs. 5(g–i) of Ref. [98].

Based on the effective medium theory for thermal radiation and conduction, Xu et al. gave the theoretical designs of three radiative metamaterials. Their work have potential applications in designing thermal camouflage [165] and thermal diode [44,166] in the regimes at high temperatures where thermal radiation is the dominant effect. Moreover, the present theory can be extended to those novel conductive metamaterials with layered structures (such as thermal bending) [167–169] to the radiative regimes. Thermal bending means that by using carefully placed layered structures with different isotropic thermal conductivities, the size and direction of heat flux can be changed according to the structure. This mechanism is effective in both steady state and transient state. Differences between the elements of the thermal conductivity tensor provide the possibility for the anisotropic heat transport. Based on the thermal bending, some novel phenomena such as anomalous refraction of heat flux and heat signature control have been realized.

In addition, some researchers attempted to control the process of thermal radiation by adjusting the emissivity [170]. Thin films of tungsten-doped vanadium dioxide are used to manipulate the infrared radiation. With this mechanism, the integrated emissivity can be reduced arbitrarily when the temperature is close to room temperature. They gave two examples; see Figs. 2–3 in [170]. Fig. 2 in [170] demonstrates a thermal infrared radiation camouflage, and one cannot

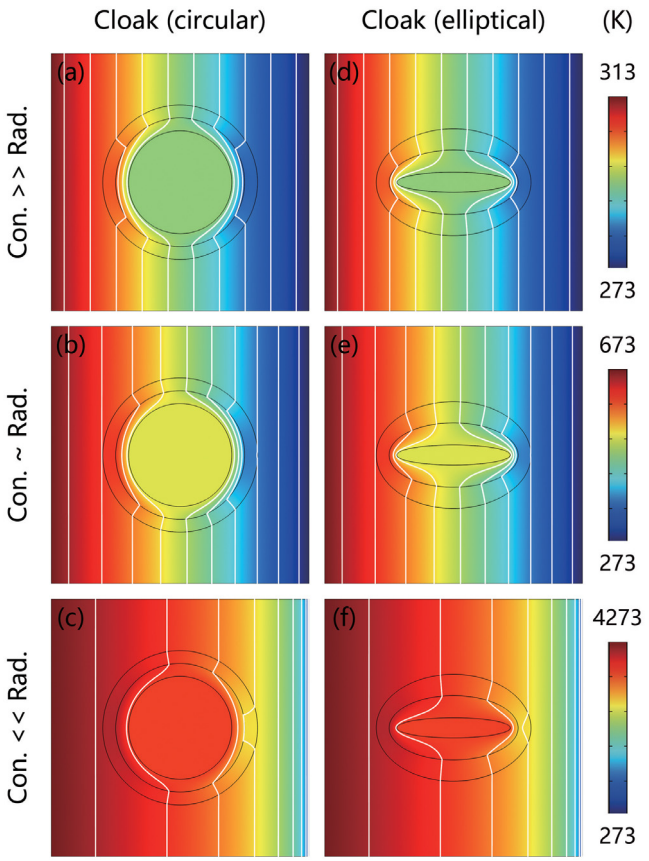

Fig. 4.8. Simulations of thermal cloak. An inner object is coated by an insulated layer with $\kappa = 10^{-5}$ W m^{-1} K^{-1} and $\beta = 10^{5}$ m^{-1}. The inner object plus the insulated layer can be equivalently regarded as an insulated core with $\kappa_c = 10^{-5}$ W m^{-1} K^{-1} and $\beta_c = 10^{5}$ m^{-1} because the heat flux cannot enter into the insulated layer. Parameters are as following. (a)–(c): $\lambda_{c1} = \lambda_{c2} = 2.5$ cm, $\lambda_{s1} = \lambda_{s2} = 3$ cm, $\kappa_s = 5.54$ W m^{-1} K^{-1}, and $\beta_s = 18.1$ m^{-1}. (d)–(f): $\lambda_{c1} = 2.5$ cm, $\lambda_{c2} = 1.25$ cm, $\lambda_{s1} = 3$ cm, $\lambda_{s2} = 2.08$ cm, $\kappa_s = 2.35$ W m^{-1} K^{-1}, and $\beta_s = 42.5$ m^{-1}.
Source: Adapted from Ref. [98].

get the true temperature of the object from the infrared image. Fig. 3 in [170] demonstrates a thermal infrared radiation decoy which means that the observer will be deceived by fake infrared images deliberately.

4.2.2. Near-field radiation

However, the Fourier law for thermal conduction is valid at the macroscale. Thus, it remains to be further explored for systems at the nanoscale where phononic effects should be considered. Meanwhile, there are many other radiative models that need to be studied further, such as near-field radiative heat transfer, see Fig. 4.10.

When the distance between objects is comparable with or shorter than the characteristic wavelength of thermal radiation, the evanescent wave on the surface contributes significantly to the radiative heat transfer. Therefore, the objects close to each other can increase heat transfer due to their enhanced near-field coupling. This behavior just corresponds to enhanced near-field radiative heat transfer [171]. Hargreaves is the first to observe the near-field enhancement of radiative heat transfer between two conducting planar plates [172] . Then, with the development of nanotechnology, Hu et al. observed that parallel glass plates have a higher near-field radiative heat transfer enhancement than metallic materials [173].

Recently, Fernandez-Hurtado et al. [159] designed a system that consists of two identical metasurfaces, which are formed by periodic arrays of square holes drilled in a doped Si layer; see Fig. 4.11. By combining fluctuation electrodynamics with a rigorous coupled wave analysis, they calculated that the Si-based metasurfaces can exhibit a larger heat transfer coefficient than any other unstructured materials. Their structure can greatly modify the properties of the surface plasmon polaritons, which dominate the radiative heat transfer in the near-field regime. Their work implies that the broadband surface-plasmon polaritons are a key factor. How to construct systems to extend the frequency of the surface-plasmon polaritons is worth further studying.

Incidentally, a further experimental exploration of near-field thermal radiation may focus on equipment fabrication and method improvement, such as applying nanoscale metamaterials in the fabrication and detecting thermal radiation quantitatively in extremely near fields.

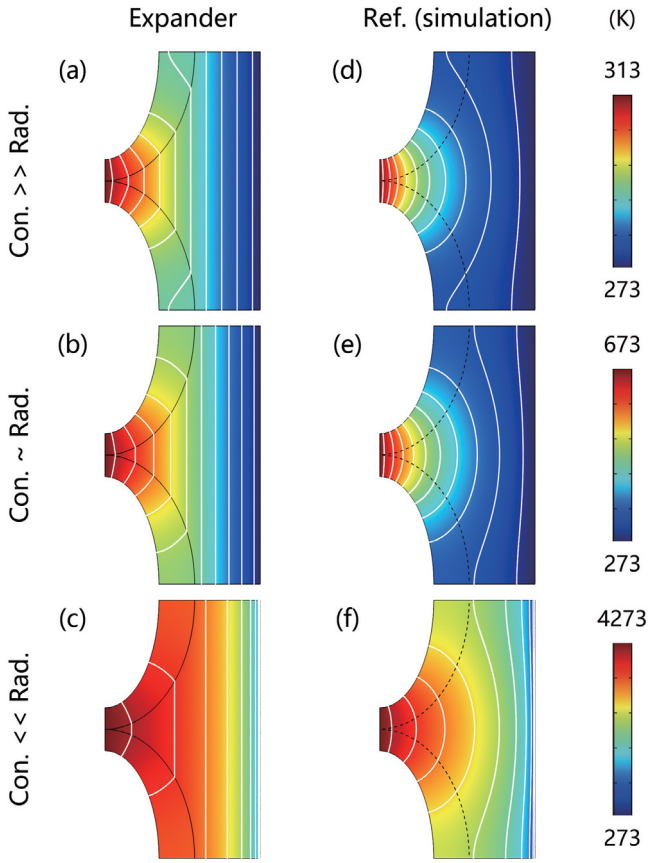

Fig. 4.9. Simulation results of thermal expander in steady regimes. Parameters: $\lambda_{c1} = 2.08$ cm, $\lambda_{c2} = 4.17$ cm, $\lambda_{s1} = 3.46$ cm, $\lambda_{s2} = 5$ cm, and the width between hot and cold sources is 6 cm. Other parameters are as follows. (a)–(c): $\kappa_s = 4.91$ W m^{-1} K^{-1} and $\beta_s = 20.3$ m^{-1}. (d)–(f): pure background parameters.
Source: Adapted from Ref. [98].

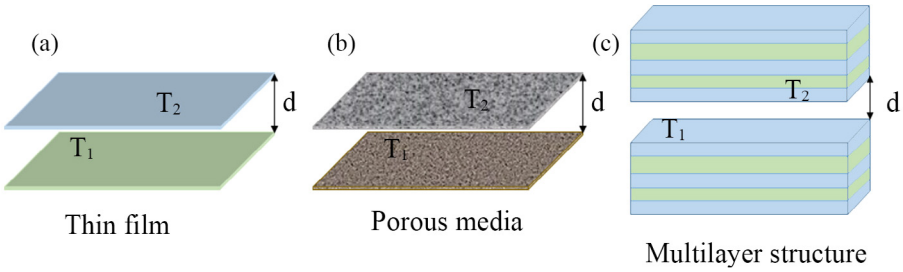

Fig. 4.10. Three typical modes of near-field radiative heat transfer between (a) thin films, (b) porous media, and (c) multilayer structures.

5. Controlling heat conduction, convection and radiation

5.1. Transformation method

5.1.1. Transformation rule

So far, transformation theories for thermal conduction, convection, and radiation have all been introduced for some convection or radiation models. Then, it is natural to think about how to take all the three basic heat transfer mechanisms into a single framework of transformation theory.

Recently, some researchers proposed the concept of transformation omnithermotics [174] which is a comprehensive model to transform conduction, convection, and radiation simultaneously. Firstly, the researchers considered the heat

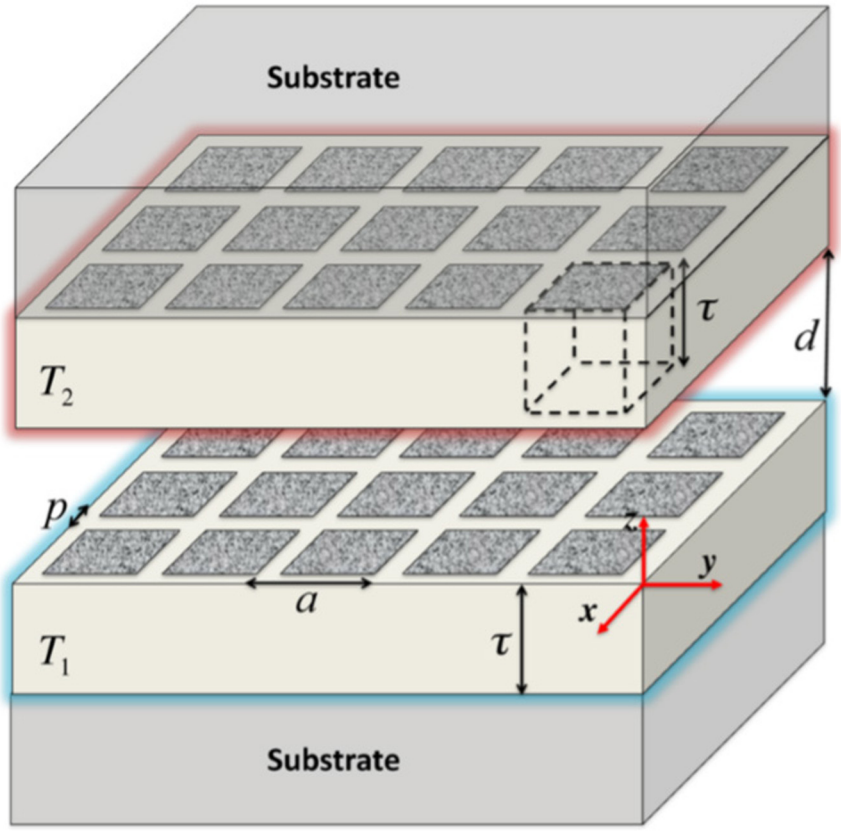

Fig. 4.11. Schematic diagram of two doped-Si metasurfaces.
Source: Figure reprinted with permission from Fernandez-Hurtado et al. Phys. Rev. Lett., 118, 203901, 2017.

transfer equation, which is a continuity equation of the total heat flux, and designed a series of devices including cloaking, concentrating, and rotating.

In the work, the radiative flux is modeled by the Rosseland diffusion approximation, and the heat transfer equation can be seen as a convection–diffusion equation where the total temperature-responsive conductivity consists of both conductive part and convective part. Here, the conductive/radiative thermal conductivities and the velocity need to be transformed directly according to the transformation theory. Then the researchers turned to a set of equations governing heat and mass transfer in porous media including the Darcy law, the continuity equation of fluid motion, and the heat transfer equation. In view of the transformation convection theory as mentioned above, designing related thermal devices means transforming both the permeability of porous media (or dynamic viscosity of fluids for convection) and the total thermal conductivity for conduction–radiation. In fact, porous media can be a typical model taking the three basic heat transfer mechanisms into account at the same time, especially under high temperatures. As a result, they predicted omnithermal metamaterials, which can control heat conduction, convection and radiation simultaneously. Details are as following.

Fluids or gases are indispensable to the existence of convective flux. In spite of different forms, they follow the same equation in terms of heat transfer. For brevity, Xu et al. [174] considered the transient process of heat transfer in pure fluids (or gases) by taking into account conduction, convection, and radiation. This process can be described by

$$\begin{aligned} \rho_f C_f \partial T/\partial t + \nabla \cdot \left(-\boldsymbol{\kappa}_f \cdot \nabla T + \rho_f C_f \boldsymbol{v}_f T - \boldsymbol{\alpha}_f T^3 \cdot \nabla T\right) = 0, \\ \partial \rho_f/\partial t + \nabla \cdot \left(\rho_f \boldsymbol{v}_f\right) = 0, \end{aligned} \tag{5.1}$$

where ρ_f, C_f, $\boldsymbol{\kappa}_f$, and $\boldsymbol{v}_f$ are the density, heat capacity, thermal conductivity, and velocity of fluid, respectively. $\boldsymbol{\alpha}_f$ $\left(= 16\boldsymbol{\beta}_f^{-1}\boldsymbol{n}_f^2\sigma/3\right)$ can be regarded as radiative coefficient where $\boldsymbol{\beta}_f$, $\boldsymbol{n}_f$, and σ $\left(= 5.67 \times 10^{-8}\,\mathrm{W\,m^{-2}\,K^{-4}}\right)$ are the Rosseland mean attenuation coefficient, relative refractive index, and the Stefan–Boltzmann constant, respectively. T and t denote temperature and time, respectively. Physically speaking, the two equations in Eq. (5.1) describe the conservation

of heat flux and mass flux, respectively. Conductive flux $\boldsymbol{J}_1$ is determined by the Fourier law $\boldsymbol{J}_1 = -\boldsymbol{\kappa}_f \cdot \nabla T$; convective flux $\boldsymbol{J}_2$ is given by $\boldsymbol{J}_2 = \rho_f C_f \boldsymbol{v}_f T$; radiative flux $\boldsymbol{J}_3$ is dealt with the Rosseland diffusion approximation $\boldsymbol{J}_3 = -\boldsymbol{\alpha}_f T^3 \cdot \nabla T$; and total flux $\boldsymbol{J}_T$ is the summation of conductive, convective, and radiative fluxes $\boldsymbol{J}_T = \boldsymbol{J}_1 + \boldsymbol{J}_2 + \boldsymbol{J}_3$.

Eq. (5.1) is form-invariant under the space transformation from a curvilinear space S to a physical space S', which is determined by the Jacobian transformation matrix $\boldsymbol{\Lambda}$. To prove the form-invariance, Xu et al. wrote down the component form of Eq. (5.1). In the curvilinear space with a set of contravariant basis $\left(\boldsymbol{g}^i, \boldsymbol{g}^j, \boldsymbol{g}^k\right)$ and corresponding contravariant components $\left(s^i, s^j, s^k\right)$, Eq. (5.1) can be rewritten as

$$\begin{aligned} \sqrt{g}\rho_f C_f \partial_t T + \partial_i \left(\sqrt{g}\left(-\kappa_f^{ij}\partial_j T + \rho_f C_f v_f^i T - \alpha_f^{ij} T^3 \partial_j T\right)\right) = 0, \\ \sqrt{g}\partial_t \rho_f + \partial_i \left(\sqrt{g}\rho_f v_f^i\right) = 0, \end{aligned} \tag{5.2}$$

where g is the determinant of the matrix $\boldsymbol{g}_i \cdot \boldsymbol{g}_j$, and $\left(\boldsymbol{g}_i, \boldsymbol{g}_j, \boldsymbol{g}_k\right)$ is a set of covariant basis. Eq. (5.2) is written in the curvilinear space, which should be rewritten in the physical space with the Cartesian coordinates $\left(s^{i'}, s^{j'}, s^{k'}\right)$,

$$\begin{aligned} \sqrt{g}\rho_f C_f \partial_t T + \partial_{i'} \frac{\partial s^{i'}}{\partial s^i}\left(\sqrt{g}\left(-\kappa_f^{ij}\frac{\partial s^{j'}}{\partial s^j}\partial_{j'} T + \rho_f C_f v_f^i T - \alpha_f^{ij} T^3 \frac{\partial s^{j'}}{\partial s^j}\partial_{j'} T\right)\right) = 0, \\ \sqrt{g}\partial_t \rho_f + \partial_{i'} \frac{\partial s^{i'}}{\partial s^i}\left(\sqrt{g}\rho_f v_f^i\right) = 0, \end{aligned} \tag{5.3}$$

where $\partial s^{i'}/\partial s^i$ and $\partial s^{j'}/\partial s^j$ are just the components of the Jacobian transformation matrix $\boldsymbol{\Lambda}$, and $\sqrt{g} = 1/\det \boldsymbol{\Lambda}$. The key to transformation theory is to turn space transformation into material transformation. For this purpose, Eq. (5.3) can be rewritten as

$$\begin{aligned} \frac{\rho_f}{\det \boldsymbol{\Lambda}} C_f \partial_t T + \partial_{i'}\left(-\frac{\frac{\partial s^{i'}}{\partial s^i}\kappa_f^{ij}\frac{\partial s^{j'}}{\partial s^j}}{\det \boldsymbol{\Lambda}}\partial_{j'} T + \frac{\rho_f}{\det \boldsymbol{\Lambda}} C_f \frac{\partial s^{i'}}{\partial s^i} v_f^i T - \frac{\frac{\partial s^{i'}}{\partial s^i}\alpha_f^{ij}\frac{\partial s^{j'}}{\partial s^j}}{\det \boldsymbol{\Lambda}} T^3 \partial_{j'} T\right) = 0, \\ \partial_t \frac{\rho_f}{\det \boldsymbol{\Lambda}} + \partial_{i'}\left(\frac{\rho_f}{\det \boldsymbol{\Lambda}}\frac{\partial s^{i'}}{\partial s^i} v_f^i\right) = 0. \end{aligned} \tag{5.4}$$

Thus, transformation rules can be derived as

$$\begin{aligned} \rho_f' &= \rho_f / \det \boldsymbol{\Lambda}, \\ C_f' &= C_f, \\ \boldsymbol{\kappa}_f' &= \boldsymbol{\Lambda}\boldsymbol{\kappa}_f \boldsymbol{\Lambda}^\tau / \det \boldsymbol{\Lambda}, \\ \boldsymbol{v}_f' &= \boldsymbol{\Lambda}\boldsymbol{v}_f, \\ \boldsymbol{\alpha}_f' &= \boldsymbol{\Lambda}\boldsymbol{\alpha}_f \boldsymbol{\Lambda}^\tau / \det \boldsymbol{\Lambda}, \end{aligned} \tag{5.5}$$

where $\boldsymbol{\Lambda}^\tau$ is the transpose of $\boldsymbol{\Lambda}$. The radiative coefficient is determined by two parameters, namely the Rosseland mean attenuation coefficient and relative refractive index. Since natural materials have only a small range of relative refractive indexes, it is not necessary to transform relative refractive indexes, namely $\boldsymbol{n}_f' = \boldsymbol{n}_f$. Then, the transformation of radiative coefficient $\boldsymbol{\alpha}_f$ becomes $\boldsymbol{\beta}_f' = \boldsymbol{\Lambda}^{-\tau}\boldsymbol{\beta}_f \boldsymbol{\Lambda}^{-1} \det \boldsymbol{\Lambda}$. For brevity, they also did not transform relative refractive indexes when performing finite-element simulations.

5.1.2. Omnithermal metamaterial

To exhibit different influences of the three basic heat transfer mechanisms, Xu et al. chose three different cases in the simulations. The first case (I): the temperature interval is 300–360 K and background velocity is along $+x$ axis. In case (I), convection is dominant. The second case (II): the temperature interval is 300–1200 K background velocity is along $+x$ axis. In case (II), radiation starts taking effects. The third case (III), the temperature interval is 300–1200 K and background velocity is along $-x$ axis. In case (III), the total flux recedes because convective flux has an opposite direction compared to cases (I) and (II). When the initial temperatures are set at 300 K, it needs about 80, 30, and 50 mins for the three cases to reach steady states.

Fig. 5.1 presents the transient simulation results of cloaking. The temperature evolutions with time under three different cases (say, I, II, and III) are demonstrated in Fig. 5.1(a–d), (e–h), and (i–j), respectively. To avoid the problems of singular parameters, the boundary at $r = R_1$ is set with insulated and no-flow conditions. In this way, any object can be placed in the central white regions of Fig. 5.1. Moreover, the background isotherms are kept unchanged, thus confirming the cloaking effect.

Xu et al. also plotted the conductive, convective, radiative, and total flux of the background in Fig. 5.1(d), (h), and (l) for quantitative analyses. The distributions of heat fluxes are presented in Fig. 5.2(a–c).

Concentrating effect is shown in Fig. 3 of Ref. [174]. The isotherms in the center of each simulation are more intensive than those in the background, indicating the presence of larger heat fluxes. Therefore, the concentrating effect is achieved, as expected.

Figure 4 of Ref. [174] presents the rotating effect. The isotherms in the center of each simulation become horizontal and high temperatures appear in the bottom, indicating that the direction of heat fluxes is vertically upward. In other words, heat fluxes are successfully rotated $\pi/2$ rad.

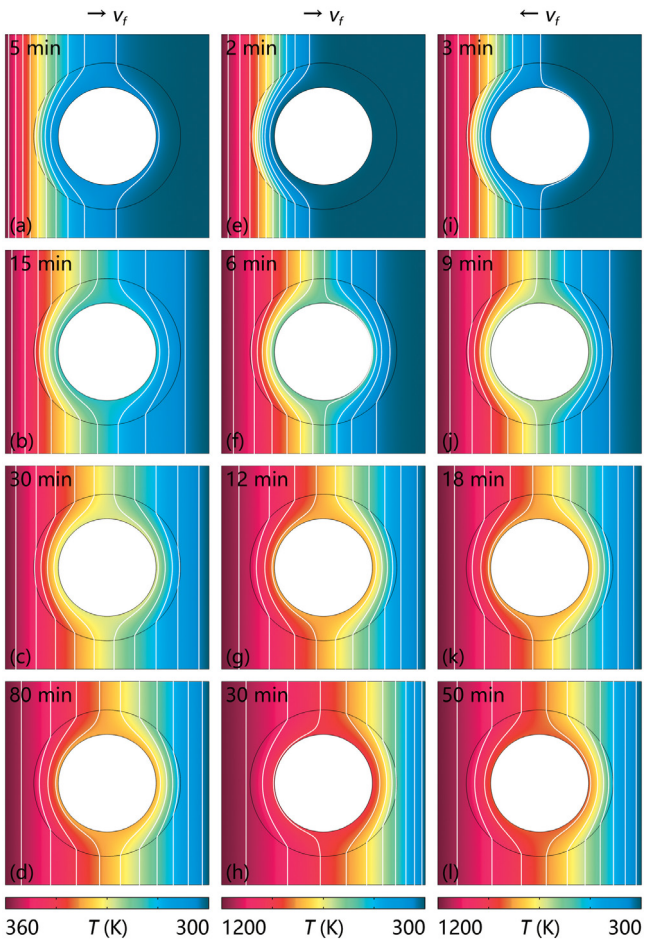

Fig. 5.1. Transient simulations of cloaking. The size of each simulation box is 0.1 m×0.1 m, $R_1 = 0.024$ m, and $R_2 = 0.036$ m, where R_1 and R_2 are the inner and outer radii, respectively. The parameters of background fluid are as following: density of the fluid $\rho_f = 1000$ kg/m^3, heat capacity of the fluid $C_f = 1000$ J kg^{-1} K^{-1}, thermal conductivity of the fluid $\boldsymbol{\kappa}_f = 1$ W m^{-1} K^{-1}, velocity of the fluids $\boldsymbol{v}_f = 10^{-5}$ m/s, the Rosseland mean attenuation coefficient $\boldsymbol{\beta}_f = 100$ m^{-1}, and relative refractive index $\boldsymbol{n}_f = 1$. (a)–(d), (e)–(h), and (i)–(l) show the temperature evolutions over time with case I, II, and III, respectively. White lines represent isotherms, and color surfaces denote temperature distributions.
Source: Adapted from Ref. [174].

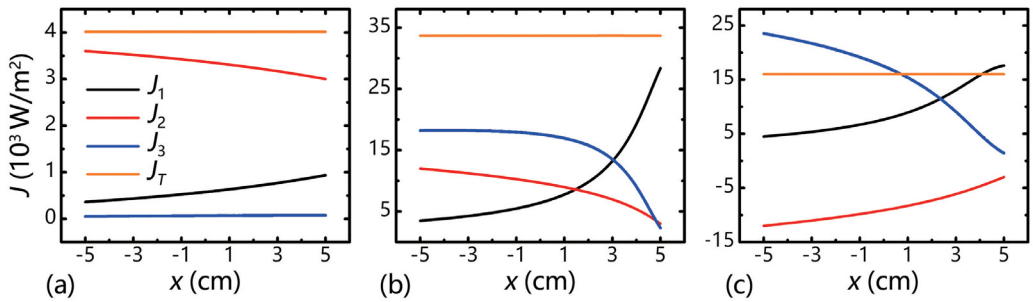

Fig. 5.2. Heat flux distributions in background along x axis. (a), (b), and (c) present the distributions of steady heat flux with the same boundary conditions applied in the first, second, and third columns in Fig. 5.1, respectively.
Source: Adapted from Ref. [174].

In the above discussion, they transformed flow velocity directly because velocity field is pre-established. This operation is completely right in mathematics, but extremely difficult in experiments. Therefore, Xu et al. controlled flow velocity with porous media to ensure feasibility.

To confirm the theoretical analyses, they also performed finite-element simulations. The first row in Fig. 5 of Ref. [174] presents the results with transforming the permeability of porous media as $\boldsymbol{\eta}_s' = \boldsymbol{\Lambda}\boldsymbol{\eta}_s\boldsymbol{\Lambda}^{\mathrm{T}}/\det\boldsymbol{\Lambda}$. The second row in Fig. 5 of Ref. [174] shows the results with directly transforming flow velocity as $\boldsymbol{v}_f' = \boldsymbol{\Lambda}\boldsymbol{v}_f/\det\boldsymbol{\Lambda}$. As a result, they confirmed the feasibility of controlling flow velocity with designed permeability by comparing the velocity distributions of two different methods.

For most commonly used coordinate transformations, it is a challenge to construct an anisotropic radiative conductivity or a radiative conductivity tensor, which is similar to transformation multithermotics [148]. A convenient method is to adopt composites made of bulk homogeneous isotropic materials with different Rosseland mean opacities or radiative conductivities. On the other hand, from a microscopic perspective, the anisotropy in an anisotropic diffusive radiation model for porous media usually comes from the anisotropic scattering and absorption process. The radiative conductivity tensor is a complicated function of extinction and scattering coefficients [175]. In general cases, the Beer–Lambert law might break down and the Rosseland model should be adjusted or generalized [176–178]. Anyway, since one needs a radiative transport equation with an anisotropic radiative thermal conductivity, in the transformed space, the radiation process does not need to satisfy all the assumptions of the Rosseland diffusion approximation. But it can be described by a more general radiative Fourier law.

For experimental demonstration, one can resort to porous media by adjusting thermal conductivities, permeabilities, and extinction coefficients simultaneously. Fortunately, the experiments on either conduction or convection have been conducted as mentioned above. Nevertheless, for the current purpose, the crucial challenge lies in combining heat radiation into the existing frameworks.

Xu et al. established the theory of transformation omnithermotics to control thermal conduction, convection and radiation simultaneously. In other words, within the theoretical framework of transformation omnithermotics, Xu et al. had achieved a unification among the three basic modes of heat transfer. They further designed three devices with functions of cloaking, concentrating, and rotating as model applications. Finite-element simulations are used to confirm the theory. To ensure the feasibility and completeness of this work, Xu et al. also applied porous media to control flow velocity. These results have potential applications, say, in solar vapor generation or aerogel insulation, where conduction, convection, and radiation must be taken into account simultaneously.

5.2. Other methods

5.2.1. Radiative cooling

Radiative cooling is common in real life. For example, people feel cool at night because there is almost no radiation from the sun, but the earth radiates heat to the outer space [179]. The principle of radiative cooling is shown in Fig. 5.3. Consider an object which is exposed to the sun. It dissipates heat through radiation but absorbs heat under the direct sunlight. In addition, natural convention and thermal conduction also affect the temperature. To achieve cooling, one needs to cover the object with a carefully designed layer to enhance its radiation and reflection of the sunlight. It is known that the earth has a transparency window in the atmosphere, mostly between 8 and 13 μm. Raman and coauthors [161] described the net cooling power $P_{cool}(T)$ of a radiative cooler as $P_{cool}(T) = P_{rad}(T) - P_{atm}(T) - P_{sun}(T) - P_{cond+conv}(T)$, where $P_{rad}(T)$ is the radiative power, $P_{atm}(T)$ is the absorbed power due to incident atmospheric thermal radiation, $P_{sun}(T)$ is the incident solar power absorbed by the object, and $P_{cond+conv}(T)$ is the power loss or gain due to convection and conduction. To achieve the best cooling effect, the radiative cooler must emit strongly and selectively in the atmospheric transparency window to maximize $P_{rad}(T)$, and reflect all other light at visible and near-infrared wavelengths to minimize $P_{atm}(T) + P_{sun}(T)$. The advent of nanoscale optical materials represented by photonic crystals and metamaterials makes it possible to design materials which can meet the above requirements. Therefore, the research of passive radiative cooling through the atmospheric infrared transparency window has become a hot topic in the field of heat radiation.

In 2013, Fan's group designed a metal–dielectric photonic structure which minimizes solar absorption and selectively emits in the atmospheric transparency window by numerical simulations [180]. The photonic crystal is a multilayer micro–nano structure with periodic holes, whose net cooling power exceeds 100 W/m^2. Later, they simplified the multilayer structure, and fabricated a photonic crystal which is composed of SiO_2, HfO_2, and Sliver [161]. This structure can reflect 97 percent of the incident sunlight while strongly and selectively emitting in the atmospheric infrared transparency window, and it can achieve 5 ^{o}C below the ambient temperature under the direct sunlight. However, the difficulty and cost of processing seriously limit the large-scale application of this kind of device.

To solve the above problem, some other researchers designed a randomized glass-polymer hybrid metamaterial which is made of polymethyl-pentene [36]. They randomly inlaid small spheres of SiO_2 with an average diameter of eight microns on one side of the material and coated the other side with sliver. The 8-micron glass spheres can radiate heat from beneath of the material in infrared light of 8-14 μm, which corresponds to the atmospheric transparency window. Meanwhile, polymethyl-pentene and sliver layer will reflect most of incident visible light, see Fig. 5.4(a–b). This kind of metamaterial has an infrared emissivity larger than 0.93 across the atmospheric window, and shows a 93 watts radiative cooling power per square meter under the direct sunlight. The most prominent advantage of such metamaterials is that it can be fabricated at low cost and on a large scale, based on which this type of metamaterials (films) has obtained mass production successfully, see Fig. 4(A) in Ref. [36].

In 2018, some researchers fabricated hierarchically porous poly coatings (vinylidene fluoride-co-hexafluoropropene), which have excellent performance of passive daytime radiative cooling [181]. Poly and water were mixed in acetone, and

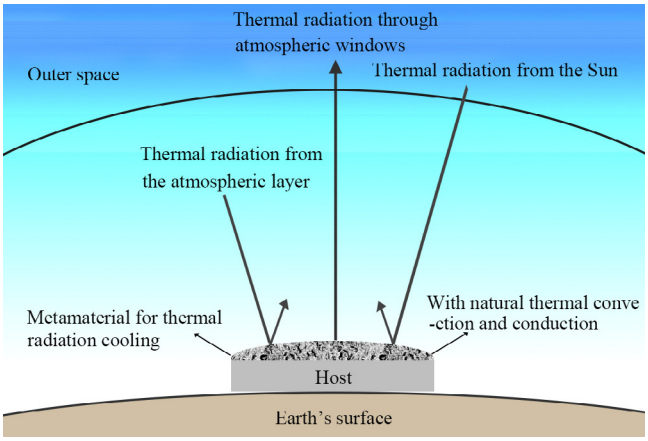

Fig. 5.3. Schematic diagram showing the full heat-transfer modes associated with radiative cooling.

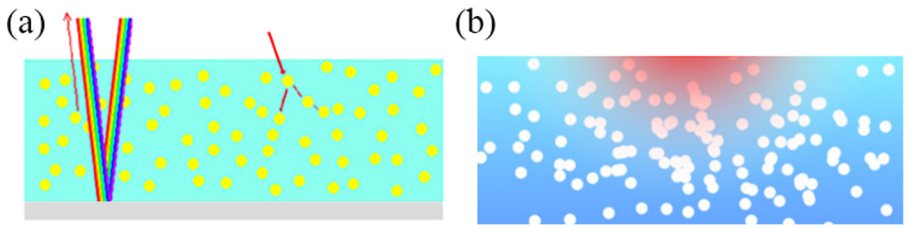

Fig. 5.4. (a) Schematic diagram of the hybrid metamaterial. The yellow circles are SiO_2. (b) Schematic of the polymer-based hybrid metamaterial for large-scale radiative cooling.

dry it in air. The evaporation of the acetone and water results in the formation of micro–nano air cavity inside poly. As a result, this coating has a high reflectance of 96 percent in the visible light band, and shows a 96 watts cooling power per square meter. Compared with the previous approach, the polymer is convenient to use and easier to fabricate, which is a promising candidate as a passive radiative cooling material.

It is interesting that the mechanism of radiative cooling exists in nature as well. Say, the silver ant of the Sahara desert is a typical example. Shi et al. reported that Saharan silver ants are covered with a dense array of hairs on the top and sides of their bodies [89]. The special arrangement of hairs enhances reflectivity in the visible and near-infrared and enhances emissivity in the middle-infrared, thus protecting ants against getting overheated.

It is known that the sun and the outer space are the two most important thermal resources for the earth. How to combine solar heating and radiative cooling technology is a challenge. Fan et al. reported the first experimental demonstration of simultaneously and synergistically harvesting energy from these two resources [182]. Their setup is composed of a solar absorber placed on the top of a radiative cooler, which is a selective emitter [183] with a high transparency in the 8–13 μm wavelength range. They enclosed the cooler in a vacuum chamber with a ZnSe window, which is also transparent in the atmospheric transparency window. The final experimental results show that the absorber (or the cooler) is 24 K (or 29 K) above (or below) the ambient with the same physical area. They offered a new way to make renewable energy more efficient.

The above-mentioned experimentally radiative cooling works in dry regions. Liu et al. studied the effect of atmospheric water vapor on radiative cooling performance [184]. Their theoretical calculations and experimental results show that the cooling power decreases and the deceleration is attenuating with an increasing water vapor column. This is because the increment of water vapor causes the radiative cooler to absorb more atmospheric radiation. Their work provides guidance for practical applications of radiative cooling in different weather.

So far, the radiative cooling technology has been used in many practical applications, including those for making woods stronger and cooler [37]. Some experiments also demonstrated the excellent effect of radiative cooling on daytime building cooling [185–188]. Firstly, researchers proved the possibility of daytime radiative cooling [185]. A high content $Ti0_2$ white paint is used to achieve a reduction of two degrees under direct sunlight on a clear day. Then, by using the method of separating daytime and nighttime cooling, researchers proposed an integrated radiation cold system which can provide efficient and continuous day-and-night cooling. Based on the existing results, this type of system can be up to 10.6 degrees lower than the surrounding environment at noon [188]. Radiative cooling technology can also be used to cool solar cells [189–191]. As we all know, solar radiation is necessary for the operation of solar devices, but at the same time, the heat caused by radiation will affect the performance of solar cells. To overcome this problem, researches

proposed a comprehensive photonic approach to reduce the temperature of solar cells. One-dimensional photonic films are used here to absorb sunlight selectively and meanwhile realize radiative cooling. Experimental results showed that by applying the photonic cooler, the temperature of the cell can be reduced by 5.7 degrees [191]. Recently, researchers have also used radiative cooling method to collect the dew efficiently [192–194]. Current radiation cooling devices can reflect almost all solar radiation, so even under direct sunlight, it can produce dew. What is more, metamaterials, which are designed and manufactured with nanotechnology, can achieve radiative cooling beyond silk. They are especially suitable for making comfortable clothing [195–197].

Obviously, radiative cooling has a huge application prospect, and more work can be expected in this direction. Finally, it is worth mentioning that, in all the existing application scenarios of radiative cooling, heat conduction and convection play an important role too. That is, the integrated effects of heat radiation, heat conduction and heat convection yield the desired cooling at certain regions.

5.2.2. Restructurable metasurface

Recently Wang et al. proposed a class of restructurable metasurfaces to show both illusion in infrared view and similarity in visible-light view [198]. They considered three basic modes of heat transfer (omnithermotics) in theoretical designs and adopt radiation-cavity effects in experimental manufactures. They also made it feasible to tune surface temperature and emissivity synergistically.

Wang et al. designed an omnithermal restructurable thermal metasurface for infrared illusion; see Fig. 1 of Ref. [198].

The total thermal radiative energy density I_{bb} of a black body is determined by the Stefan−Boltzmann law [199], which is related to the biquadrate of surface temperature T_{sur},

$$\begin{aligned} I_{\mathrm{bb}} &= \int_0^\infty u_{bb}\left(\lambda,\ T_{\mathrm{sur}}\right) d\lambda = \int_0^\infty \frac{2\pi hc^2}{\lambda^5} \frac{1}{e^{\frac{hc}{\lambda k_B T_{\mathrm{sur}}}} - 1} d\lambda \\ &= \left(\frac{2\pi^5 k_B^4}{15c^2h^3}\right) T_{\mathrm{sur}}^4 = \sigma T_{\mathrm{sur}}^4, \end{aligned} \tag{5.6}$$

where λ is radiative wavelength and $u_{bb}\left(\lambda,\ T_{\mathrm{sur}}\right)$ is the black-body spectral radiance, which is described by the Planck law. Here, h is the Planck constant, c is light's velocity in vacuum, k_B is the Boltzmann constant, and σ is the Stefan−Boltzmann constant. Consider that an infrared camera captures the infrared signals of an object in a far field for identification, and the actually received spectral radiance deviates from the result described by Eq. (5.6). This deviation can be described by spectral directional emissivity $\varepsilon_{\mathrm{sur}}(\lambda,\ T_{\mathrm{sur}}, \theta, \phi)$, which is defined as the spectral-radiance ratio of actual objects to black bodies at temperature T_{sur}, wavelength λ, and direction angles θ and ϕ. However, the diffuse-emitter approximation is reasonable enough in most practical situations without elaborate directed thermal emission. Therefore, the surface emissivity can be simplified as $\varepsilon_{\mathrm{sur}}(\lambda,\ T_{\mathrm{sur}})$. Then, write down the actual radiative energy density I_{ac},

$$\begin{aligned} I_{\mathrm{ac}} &= \int_0^\infty \varepsilon_{\mathrm{sur}}\left(\lambda,\ T_{\mathrm{sur}}\right) u_{bb}\left(\lambda,\ T_{\mathrm{sur}}\right) d\lambda \\ &= \int_0^\infty \varepsilon_{\mathrm{sur}}\left(\lambda,\ T_{\mathrm{sur}}\right) \frac{2\pi hc^2}{\lambda^5} \frac{1}{e^{\frac{hc}{\lambda k_B T_{\mathrm{sur}}}} - 1} d\lambda. \end{aligned} \tag{5.7}$$

As the total thermal radiative energy is taken into consideration, the full wavelength emissivity $\varepsilon_{\mathrm{sur}}(T_{\mathrm{sur}})$ makes sense, which can be defined as

$$\begin{aligned} \varepsilon_{\mathrm{sur}}(T_{\mathrm{sur}}) &= \frac{I_{\mathrm{ac}}}{I_{\mathrm{bb}}} \\ &= \frac{\int_0^\infty \varepsilon_{\mathrm{sur}}\left(\lambda,\ T_{\mathrm{sur}}\right) u_{bb}\left(\lambda,\ T_{\mathrm{sur}}\right) d\lambda}{\int_0^\infty u_{bb}\left(\lambda,\ T_{\mathrm{sur}}\right) d\lambda} \\ &= \frac{\int_0^\infty \varepsilon_{\mathrm{sur}}\left(\lambda,\ T_{\mathrm{sur}}\right) u_{bb}\left(\lambda,\ T_{\mathrm{sur}}\right) d\lambda}{\sigma T_{\mathrm{sur}}^4}. \end{aligned} \tag{5.8}$$

Except for the fact that the intrinsic emissivity affects thermal radiation, they took both signal collection range and resolution of the infrared camera into consideration. The signal collection range $(\lambda_1,\ \lambda_2)$ covers the main emission band according to practical situations. Then, they could adopt the full wavelength emissivity $\varepsilon_{\mathrm{sur}}(T_{\mathrm{sur}})$ in this scene. The combination of Eqs. (5.7)–(5.8) yields the reading temperature T_{read} as [165]

$$\begin{aligned} T_{\mathrm{read}} = C \times I_{ac} &= C \int_{\lambda_1}^{\lambda_2} \varepsilon_{\mathrm{sur}}\left(\lambda,\ T_{\mathrm{sur}}\right) u_{bb}\left(\lambda,\ T_{\mathrm{sur}}\right) d\lambda \\ &\approx C\varepsilon_{\mathrm{sur}}\left(T_{\mathrm{sur}}\right) \int_{\lambda_1}^{\lambda_2} u_{bb}\left(\lambda,\ T_{\mathrm{sur}}\right) d\lambda \\ &\approx C\varepsilon_{\mathrm{sur}}\left(T_{\mathrm{sur}}\right) \int_{\lambda_1}^{\lambda_2} \frac{2\pi hc^2}{\lambda^5} \frac{1}{e^{\frac{hc}{\lambda k_B T_{\mathrm{sur}}}} - 1} d\lambda, \end{aligned} \tag{5.9}$$

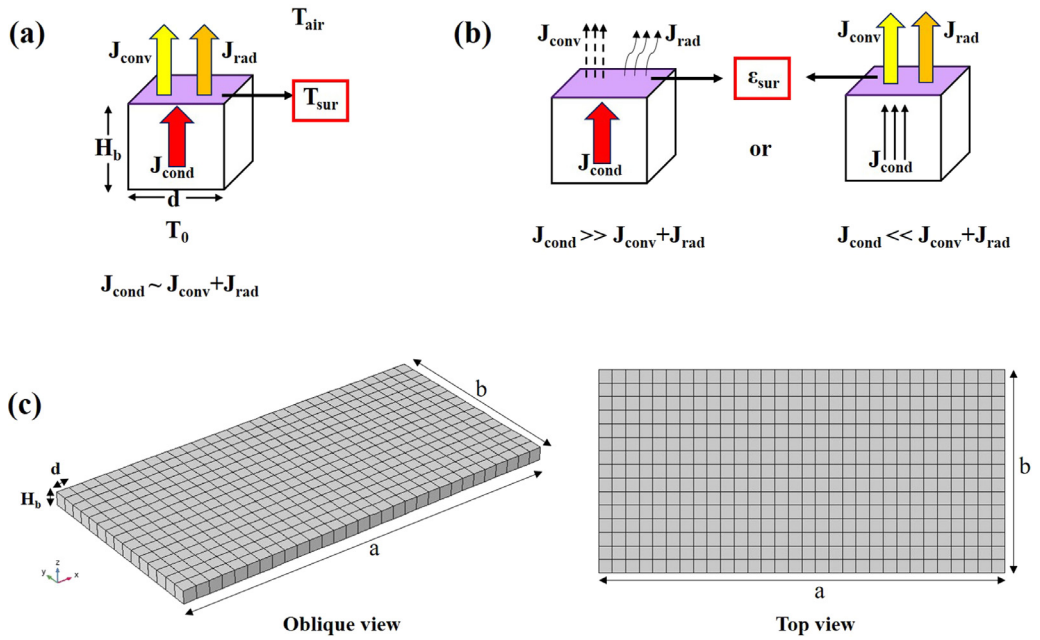

Fig. 5.5. Different tuning methods. (a–b) A cuboid as a block unit. Conductive flow is comparable with convective and radiative flow in (a), but dramatically different in (b). (c) Assembly of the units, which construct the whole metasurface.
Source: Adapted from Ref. [198].

where C is a built-in conversion parameter of the infrared camera. Eq. (5.9) indicates that two factors dominate the infrared imaging, say, the camera capacity [C, (λ_1, λ_2)] and the surface properties (T_{sur}, ε_{sur}). Here, modulating the characteristic radiative spectrum is of their concern, which depends on the surface properties (T_{sur}, ε_{sur}). Within a limited surface temperature region, the full wavelength emissivity $\varepsilon_{\text{sur}}(T_{\text{sur}})$ is treated as ε_{sur}, which is independent on T_{sur}. To be mentioned, if the surface temperature varies sharply, the coupling relation between ε_{sur} and λ should be underlined. Meanwhile, while the surface temperature difference is large enough between units, the coupling relation between ε_{sur} and T_{sur} should also be taken into account. Their strategy for controllable infrared illusion includes tuning T_{sur} and ε_{sur} individually and assembling them in any specific way.

Wang et al. considered a three-dimensional bulk as a unit for the first step, as illustrated in Fig. 5.5(a). They set its sides to be thermally insulated and place a homothermal source at the bottom. The heat flows in the bulk along z axis and dissipates into surroundings from the top surface due to thermal convection and radiation. This process contains three basic modes of heat transfer. In a steady regime, the temperature of top surface T_{sur} can be determined by the conservation law of heat flow,

$$\boldsymbol{J}_{\text{cond}} = \boldsymbol{J}_{\text{conv}} + \boldsymbol{J}_{\text{rad}}, \tag{5.10}$$

where $\boldsymbol{J}_{\text{cond}}$, $\boldsymbol{J}_{\text{conv}}$, and $\boldsymbol{J}_{\text{rad}}$ are conductive, convective and radiative heat flow density, respectively. The unit's height is denoted as H_b and thermal conductivity is κ_b. The convective coefficient and radiative emissivity of the surface are h_b and ε_b, respectively. Moreover, they set the source and room temperatures as T_0 and T_{air}, respectively. The expressions of $\boldsymbol{J}_{\text{cond}}$, $\boldsymbol{J}_{\text{conv}}$, and $\boldsymbol{J}_{\text{rad}}$ can be written as

$$J_{\text{cond}} = \kappa_b \nabla T|_{\text{bulk}} = \kappa_b \frac{T_0 - T_{\text{sur}}}{H_b}, \tag{5.11a}$$

$$J_{\text{conv}} = h_b(T_{\text{sur}} - T_{\text{air}}), \tag{5.11b}$$

$$\begin{aligned} J_{\text{rad}} &= \varepsilon_b \sigma (T_{\text{sur}}^4 - T_{\text{air}}^4) \\ &= \varepsilon_b \sigma (T_{\text{sur}}^2 + T_{\text{air}}^2)(T_{\text{sur}} + T_{\text{air}})(T_{\text{sur}} - T_{\text{air}}) \\ &= R_b(T_{\text{sur}})(T_{\text{sur}} - T_{\text{air}}), \end{aligned} \tag{5.11c}$$

where $R_b(T) = \varepsilon_b \sigma (T_{\text{sur}}^2 + T_{\text{air}}^2)(T_{\text{sur}} + T_{\text{air}})$, representing the radiative ability of the surface. The combination of Eqs. (5.10)–(5.11c) yields the temperature of the top surface T_{sur} as

$$T_{\text{sur}} = \frac{\kappa_b T_0 / H_b + [h_b + R_b(T_{\text{sur}})]\, T_{\text{air}}}{\kappa_b / H_b + h_b + R_b(T_{\text{sur}})}. \tag{5.12}$$

Hereto, the general solution of the top-surface temperature of a unit is obtained. An iteration of $R_b(T_{\rm sur})$ should be executed by calculator to obtain the value of $T_{\rm sur}$. Compared with the method reported in Ref. [80] where only κ_b is tuned, the present scheme has four parametric freedoms for realizing infrared illusion. They are κ_b, h_b, ε_b, and H_b, involving the three basic modes of heat transfer. κ_b and H_b play the role of controlling conductive flow. h_b and ε_b are related to convective and radiative flows, respectively. These four parameters can be expressed as

$$\kappa_b = \frac{H_b[h_b(T_{\rm sur} - T_{\rm air}) + \varepsilon_b\sigma(T_{\rm sur}^4 - T_{\rm air}^4)]}{T_0 - T_{\rm sur}}, \tag{5.13a}$$

$$H_b = \frac{\kappa_b(T_0 - T_{\rm sur})}{h_b(T_{\rm sur} - T_{\rm air}) + \varepsilon_b\sigma(T_{\rm sur}^4 - T_{\rm air}^4)}, \tag{5.13b}$$

$$h_b = \frac{\kappa_b(T_0 - T_{\rm sur})/H_b - \varepsilon_b\sigma(T_{\rm sur}^4 - T_{\rm air}^4)}{T_{\rm sur} - T_{\rm air}}, \tag{5.13c}$$

$$\varepsilon_b = \frac{\kappa_b(T_0 - T_{\rm sur})/H_b - h_b(T_{\rm sur} - T_{\rm air})}{\sigma(T_{\rm sur}^4 - T_{\rm air}^4)}. \tag{5.13d}$$

In fact, only three of them are independent if the surface temperature $T_{\rm sur}$ of each unit is preset to create specific infrared illusion. Moreover, these four parameters can be tuned arbitrarily and simultaneously to achieve the designed $T_{\rm sur}$ of each unit. Thus, the tuning strategy is flexible. Suppose $\varepsilon_{\rm b}$ (equivalent to $\varepsilon_{\rm sur}$) is uniform in each unit and approximate to that of a black body. Then, the reading temperature can be estimated by Eq. (5.9) as

$$T_{\rm read1}(x,\ y) \approx C \times \int_{\lambda_1}^{\lambda_2} \frac{2\pi hc^2}{\lambda^5} \frac{1}{e^{\frac{hc}{\lambda k_B T_{\rm sur}}} - 1} d\lambda \approx T_{\rm sur}(x,\ y), \tag{5.14}$$

where $(x,\ y)$ refers to the central position of each unit.

Note that tuning ε_b plays a limited role in controlling $T_{\rm sur}$ due to its maximum value 1, especially in low temperature regions. Moreover, when $T_{\rm sur}$ is nearly uniform in each unit under some circumstances, tuning surface emissivity is another effective method to create illusion because $\varepsilon_{\rm sur}$ becomes a major impact beyond $T_{\rm sur}$ in Eq. (5.9). For example, if κ_b is far greater than h_b and $R_b(T_{\rm sur})$, $T_{\rm sur}$ will reach T_0 according to Eq. (5.12). Inversely, it will reach $T_{\rm air}$, as shown in Fig. 5.5(b). Therefore, tailoring emissivity is the only way for creating infrared illusion in the infrared imaging. On the basis of Eq. (5.9), the reading temperature in this case can be expressed as

$$T_{\rm read2}(x,\ y) \approx \varepsilon_{\rm sur}(x,\ y) \times C \times \int_{\lambda_1}^{\lambda_2} \frac{2\pi hc^2}{\lambda^5} \frac{1}{e^{\frac{hc}{\lambda k_B T_{\rm sur}}} - 1} d\lambda \approx \varepsilon_{\rm sur}(x,\ y) \cdot T_{\rm sur}. \tag{5.15}$$

The last step is to assemble these units together in a specific array to create infrared illusion, see Fig. 5.5(c). Each unit can be regarded as a pixel. The fake surface temperature of each pixel should be distinguishable enough in infrared imaging, so as to make the illusion valid. Therefore, under any conditions, the contrast ratio should be larger than the intrinsic resolution of the infrared camera, which is based on the maximum and minimum values of reading temperatures. Therefore, the contrast ratio C can be defined as

$$C = \frac{T_{\rm read}\big|_{\rm max} - T_{\rm read}\big|_{\rm min}}{T_{\rm read}\big|_{\rm max} + T_{\rm read}\big|_{\rm min}}. \tag{5.16}$$

$T_{\rm read}$ can be tailored in two ways. If the three modes of heat transfer are comparable, tuning $T_{\rm sur}$ solely is enough. According to Eq. (5.14), Eq. (5.16) can be written as

$$C_1 = \frac{T_{\rm sur}\big|_{\rm max} - T_{\rm sur}\big|_{\rm min}}{T_{\rm sur}\big|_{\rm max} + T_{\rm sur}\big|_{\rm min}}. \tag{5.17}$$

Otherwise, tuning $\varepsilon_{\rm sur}$ is necessary to present a distinguishable temperature distribution in the infrared camera. With Eq. (5.15), Eq. (5.16) can be written as

$$C_2 = \frac{\varepsilon_{\rm sur}\big|_{\rm max} - \varepsilon_{\rm sur}\big|_{\rm min}}{\varepsilon_{\rm sur}\big|_{\rm max} + \varepsilon_{\rm sur}\big|_{\rm min}}. \tag{5.18}$$

The contrast ratio is determined by the ratio of surface temperature or the extremum difference of effective emissivity, which is an intrinsic character of a sort of specifically-designed thermal metasurfaces. The flexible combination of units contributes to the reconfigurability, and does not affect the contrast ratio C. Therefore, the thermal metasurface can always meet the resolution requirement of the detector once the units are designed completely.

Then, they performed finite-element simulations. They aimed to create an illusion of "FUDAN". When tuning κ_b, keep h_b and ε_b as two constants, so as the other two parameters. Then, the six groups are assembled together as shown in Fig. 5.6(a). For brevity, the entire lower surface is heated with a homothermal source T_0 to keep the room temperature $T_{\rm air}$ at 300 K. To mimic the real situation, the laterals of the surface are thermal contacted with neighboring units. Fig. 5.6(b–d)

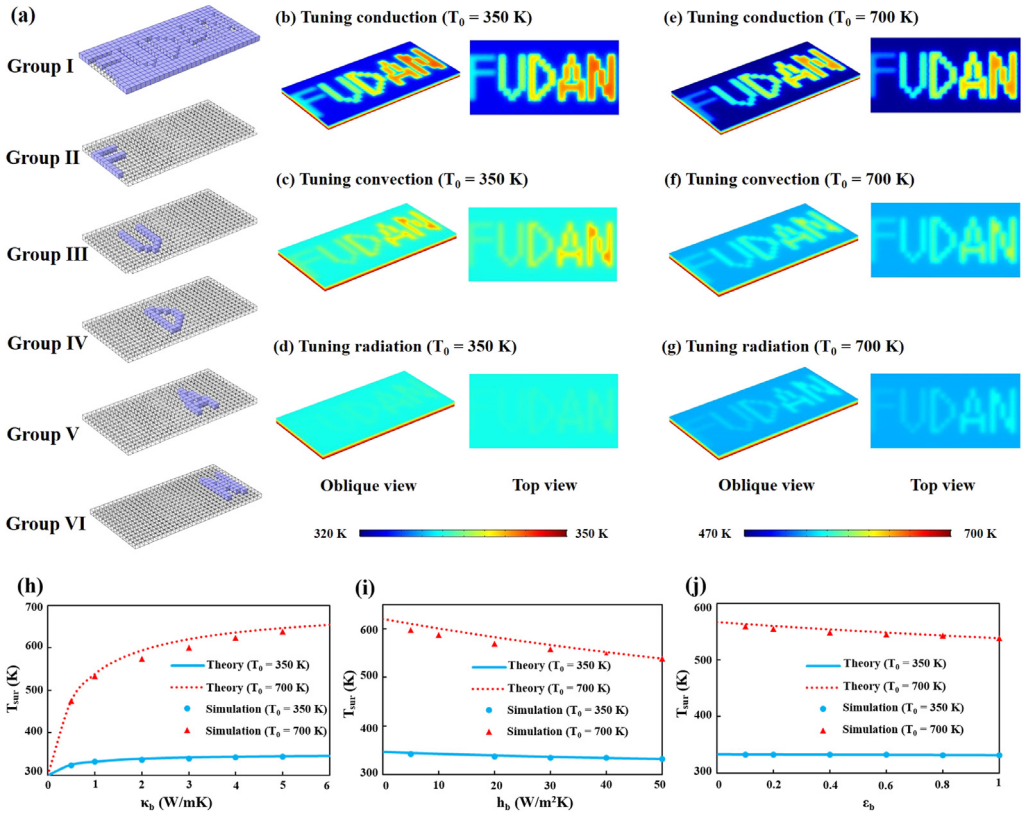

Fig. 5.6. Simulation results of tuning temperature T_{sur}. (a) Six groups and arrays with letters "FUDAN". (b–g) Temperature distributions with different tuning methods. T_0 is set at 350 K and 700 K. For tuning thermal conduction, κ_b is set as 0.5, 1, 2, 3, 4, and 5 W/(m·K) for six groups while h_b is 50 W/m^{2}K and ε_b is 1. For tuning thermal convection, h_b is 5, 10, 20, 30, 40, and 50 W/m^{2}K while κ_b is 1 W/(m·K) and ε_b is 1. For tuning thermal radiation, ε_b is 0.1, 0.2, 0.4, 0.6, 0.8, and 1 while κ_b is 1 W/(m·K) and h_b is 50 W/m^{2}K. (h–j) Comparisons between theoretical values and simulation values of T_{sur}, corresponding to the data extracted from (b–g).
Source: Adapted from Ref. [198].

respectively show the results of tuning κ_b, h_b, and ε_b at $T_0 = 350$ K, while Fig. 5.6(e–g) are the results at $T_0 = 700$ K. Under low-temperature surroundings, convection and radiation play a minor role.

Figs. 5.6(h–j) demonstrate the comparisons of T_{sur} between theoretical results and simulation results under three tuning modes. They echo well at low temperatures, and show a little shift when the temperature is high. This is because the thermal interaction between different units comes to appear. Therefore, more heat energy is exchanged in x–y plane, which has impact on T_{sur}. One should tune the effective emissivity when the condition goes to extremes (say, T_{sur} reaches T_0 or T_{air}).

As presented in Fig. 5.6(d), it has little effect on infrared illusion by tuning radiation with emissivity at low-temperature condition. However, the engineered emissivities can impact apparent temperature distribution. To modulate ε_{sur}, resort to the surface-cavity effect [200,201]. The cavity structures on the surface promote the block to a higher radiant exitance. Hence, apparent temperature in infrared imaging will be deviated from the actual one, forming an illusive pattern. For simplification, the cylindrical structure is adopted because it is easy to fabricate, as demonstrated in Fig. 5.7(a). The process of heat transfer is between surface cavity and free space, where the angle factor of the cavity can be neglected. According to Ref. [200], the effective emissivity of an isolated cylindrical cavity ε_e depends on its area ratio of mouth and inwall, which can be expressed as

$$\varepsilon_e = [1 + \frac{S_0}{S_1}(\frac{1}{\varepsilon_b} - 1)]^{-1}, \tag{5.19}$$

where S_0 and S_1 are the area of mouth and inwall, respectively. ε_{sur} is intrinsic surface emissivity. The surface temperature can be considered as a constant owing to the high thermal conductivities and regular shape of the blocks. The plate surface only allows heat energy to transfer into the environment, so only the thermal interaction between cavities occurs. Thus, they derived a quantitative emissivity expression of the whole surface of the block as

$$\varepsilon_{sur} = \varepsilon_e' \approx f\varepsilon_e + (1-f)\varepsilon_0 = f\left[1 + \frac{S_0}{S_1}(\frac{1}{\varepsilon_b} - 1)\right]^{-1} + (1-f)\varepsilon_b. \tag{5.20}$$

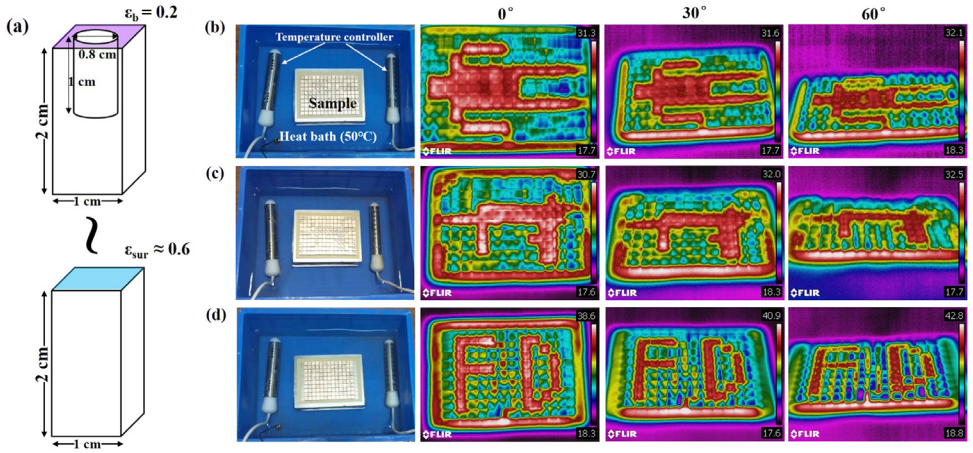

Fig. 5.7. Experimental measurements for different effective emissivities ε_{sur}. (a) Cavity structure (upper panel) and effective emissivity principle. The effective emissivity of a flat surface with cavity (upper panel) is equivalent to ε_{sur} of another flat surface (lower panel), which is quantitatively expressed in Eqs. (5.19) and (5.20). The first column of (b), (c), and (d) shows the photo of experimental apparatus for a human pattern, a machine-gun pattern, and an "FD" pattern, respectively. And the other three columns display the experimental measurements, each for one observation angle (0°, 30°, or 60°). Note that the experimental apparatus is placed in a heat bath of 50°C. The unit of numerical values in the color bars is °C.
Source: Adapted from Ref. [198].

The area proportion of the cavity f and inherent area ratio S_0/S_1 help to tailor the effective emissivity of the surface, so as to form a specific apparent temperature distribution in infrared imaging.

Wang et al. directly examined the practical effects with the infrared camera FLIR E60, whose resolution is 0.1 K. At different angles to observe, its robustness is confirmed in both infrared and visible-light views, see Fig. 5.7(b–d). It is worth mentioning that the feature pattern disappears when the surface is coated with an anti-reflection film, and the reading temperatures become a little higher than the previous ones. This confirms that the cavity engineering method helps to change the imaging indeed.

The proposed restructurability is essentially distinguished with the common reconfigurability or adjustability [202]. This is because the former is property-invariant but structurally rearrangeable, while the latter is structure-invariant but property-adjustable.

5.2.3. Switchable omnithermal metamaterial

Both transparency and cloaking are two typical functions of thermal metamaterials. However, there are two restrictions remaining to be solved: the first one is that the existing studies considered only one or two modes of heat transfer, which may not be consistent with practical conditions because conduction, radiation, and convection often coexist; the second one is that transparency and cloaking cannot be switched between each other at will. To solve these problems, based on the Fourier law, the Rosseland diffusion approximation, and the Darcy law, some researchers [203] proposed an effective medium theory to handle conductive, radiative, and convective (thus called omnithermal) processes simultaneously. As a result, they designed an omnithermal metamaterial switchable between transparency and cloaking, which results from the nonlinear properties of radiation and convection. Finite-element simulations help to confirm the scheme under different boundary conditions [203]. Such results can inspire the researches on omnithermal metamaterials with switchable functions, and have potential applications in nonlinear thermotics, intelligent thermotics, and thermal illusion/camouflage.

6. Conclusion and outlook

6.1. Conclusion

In this review, we have introduced the research development of thermal metamaterials for controlling the different modes of heat transfer on the basis of the different implementation mechanisms described by both transformation theories and their extended theories. Such theories are called theoretical thermotics for convenience [26]. In view of the current era of thermal metamaterials, more achievements and breakthroughs can be expected in the near future, ranging from fundamental theories to industrial applications.

6.2. Outlook

Convective heat flux has a completely different form from the Fourier law for heat conduction (diffusion), and radiative heat flux with the Rosseland approximation shows a nonlinear thermal conductivity. It can be expected that more devices

beyond conduction with the Fourier law can be designed by exhibiting the unique nature of convection and radiation. For example, a nonreciprocal thermal material by spatiotemporal modulation in conduction [204] was reported, which is dependent on an internal convection-like term for providing nonreciprocity.

In wave systems, gain and loss are commonly introduced to construct a non-Hermitian–Hamiltonian, and non-Hermitian physics has been intensively explored, including but not limited to parity-time-symmetry, anti-parity-time symmetry, and topology. In thermal systems, diffusion features inevitable energy loss, which is a natural non-Hermitian system. Therefore, the novel phenomena revealed in non-Hermitian wave systems are possible to be extended to thermal systems. Anti-parity-time symmetry is a typical attempt by means of the non-Hermitian property of thermal systems, which provides insights into extending the non-Hermitian physics from wave systems to diffusion systems. In addition, the thermal system where anti-parity-time symmetry is revealed is essentially a convection–diffusion system which has both parabolic and hyperbolic properties. Briefly speaking, convection has a hyperbolic property and diffusion has a parabolic system. Therefore, when convection is dominant, the thermal process is governed by a hyperbolic equation; when conduction is dominant, the thermal process is governed by a parabolic equation. Therefore, the introduction of convection is crucially important because it essentially changes the equation property. In terms of that wave systems are generally dominated by hyperbolic equations, the introduction of convection can also make thermal systems possible to display wave-like properties. A simplest example is that convection can support the propagation of temperature waves where convection contributes to their propagation and conduction leads to their temperature amplitude decay.

Besides, the classical effective medium approximations play a critical role in designing thermal metamaterials. However, the theoretical prediction of composites often deviates from practical cases when applied on irregular geometries, inhomogeneous distributions, asymmetric locations, and anisotropic thermal conductivities. More general theories are required to treat such complex systems. Another challenge is the integration of microscopic energy-band engineering and macroscopic thermal metamaterial design. As these two methods seem mutually independent for describing heat transport from different viewpoints, a bridge is surely to exist because energy transfer is substantial regardless of description ways. Then, the techniques on micro- and nano-heat become very important [205,206]. In this direction, thermal metamaterials need more research about their extensions from the macroscopic scale to the microscopic scale or even nanoscale [207]. This has both scientific significance and application value due to the different features of heat, especially at the nanoscale, as already inspired by some initial works [46–48].

Also, nonlinear thermotics, referring to that thermal conductivities are temperature dependent, continues to thrive. On the one hand, a large number of natural materials have nonlinear thermal conductivities. On the other hand, nonlinear thermal conductivities provide new functions to conventional thermal metamaterials such as intelligent and switchable thermal metamaterials. Therefore, more thermal metamaterials with nonlinear thermal conductivities can be expected to have more practical applications. In addition to natural materials that can bring nonlinearity, other modes of heat transfer beyond thermal conduction can also lead to nonlinearity. For example, thermal convection can also give rise to a nonlinear temperature distribution; thermal radiation dominated by the Rosseland diffusion approximation features the T^4 dependence of temperature, which belong to strong nonlinearity and become a powerful tool to achieve similar rectification effects [157,158,208] as anomalous conduction in nonlinear lattices [209]. The combination of three basic modes of heat transfer is more applicable for practical scenarios. More generally, the spatiotemporal modulation of thermal conductivity, which is a recent research hot point, can also be regarded as nonlinearity, to some extent. This is because that the spatiotemporal modulation of thermal conductivity (and mass density) can also generate an effective convective term which contributes to nonlinearity. In the application aspect, macroscopic calculation devices based on nonlinearity thermotics are promising in achieving thermal-energy-based calculation, which is the counterpart of phononic computers [209,210]. Moreover, nonlinear thermal conductivities are also beneficial for thermal rectification and thermal diode, which have practical applications to achieve one-way propagation in thermal protection or thermal dissipation. Meanwhile, their integration is another challenge for actual applications.

Regarding the practical applications of thermal metamaterials, a severe problem lies in the interfacial thermal resistance between two different materials, which always results in temperature discontinuous. Fortunately, the interfacial thermal resistance between macro-scale materials for constructing thermal cloaks with multilayer structures can be small enough to be neglected according to an analytical method and a numerical method [211]. This provides a theoretical hint on how to reduce the difficulty of fabricating macroscopic thermal metamaterials by eliminating the interfacial thermal resistance as much as possible, say, by using the heterogeneous structure of solids and soft matters [21]. Incidentally, it is worth noting that the interfacial thermal resistance plays a significant role at the nanoscale [212] due to many reasons including abnormal heat conduction, which has a non-negligible effect on macroscopic devices like thermal cloaks [19]. Nevertheless, we believe the interfacial thermal resistance is more close to engineering problems than physical problems. For treating physical problems, one can initially neglect this kind of interfacial thermal resistance to reveal new physics, as inspired by the roles of abundant ideal models (like ideal gases and free falling) in developing physics. After that, it must be carefully considered and tailored for practical applications in engineering.

Metamaterials were first discussed in electromagnetics. After more than ten years' development, metamaterials have achieved fruitful results in thermotics. Amounts of novel thermal devices are highly innovative in the entire field of metamaterials, as we have mentioned before. These researches play a positive role in promoting the development of metamaterials in various fields, even the interaction with other fields. For example, thermo-electricity metamaterials are being actively developed. As the governing equations of heat or electricity conduction under steady states share

similar Laplacian forms, it is intuitional to simultaneously tailor thermal and electrical conductivities in a same way. Based on this consideration, novel phenomena like cloaking, concentrating, and rotating were achieved in thermo-electric fields [19,56,57,71,213]. It is proved that both the transformation theory [19,57] and scattering-cancellation method [56,71,213] can be transplanted to thermo-electric fields. But two issues need to be further addressed in manipulating thermo-electric fields. One is that if heat and electricity flows are coupled via Seeback coefficients, the governing equations are no longer Laplacian forms. Do the reported results continue to work? Fortunately, Stedman et al. [59] have verified that the coupling thermo-electricity conduction equations still keep form invariance under coordinate transformation. So the transformation theory are valid in coupling cases. It is a challenge to fabricate the thermo-electric composite structure with anisotropic thermal conductivity, electrical conductivity and Seebeck coefficient simultaneously. Several experimental schemes exist but have not been verified [59,214]. Another concern is how to activate the scattering-cancellation method in coupling cases. In other words, an effective medium theory for treating coupling thermo-electric fields needs to be studied. Although some attempts have been executed [97,215], the lack of experimental verification will limit its practical applications. Besides, thermo-electric metamaterials may play a role in raising efficiency of energy generation and management due to its directional functionality. Integration of thermo-electric metamaterials and subsistent devices is another enormous problem, especially for further potential utilization. In addition to thermo-electricity metamaterials, thermo-acoustic and thermo-magnetic metamaterials remain to be explored. Prosperity in metamaterials is under way and can be expected in the future.

Declaration of competing interest

The authors declare that they have no known competing financial interests or personal relationships that could have appeared to influence the work reported in this paper.

Acknowledgments

We are grateful to Mr. Jipeng Huang for helping to polish the figures and to Mr. Liujun Xu for helping to improve the outlook. We acknowledge financial support from the National Natural Science Foundation of China under Grant Nos. 11725521 and 12035004 , and from the Science and Technology Commission of Shanghai Municipality under Grant No. 20JC1414700.

References

[1] V.G. Veselago, The electrodynamics of substances with simultaneously negative values of ϵ and μ, Sov. Phys. Usp. 10 (1968) 509–514.
[2] J. Pendry, A. Holden, W. Stewart, I. Youngs, Extremely low frequency plasmons in metallic mesostructures, Phys. Rev. Lett. 76 (1996) 4773–4776.
[3] J. Pendry, A. Holden, D. Robbins, W. Stewart, Magnetism from conductors and enhanced nonlinear phenomena, IEEE Trans. Microw. Theory Tech. 47 (1999) 2075–2084.
[4] J.B. Pendry, D. Schurig, D.R. Smith, Controlling electromagnetic fields, Science 312 (2006) 1780–1782.
[5] U. Leonhardt, Optical conformal mapping, Science 312 (2006) 1777–1780.
[6] D. Schurig, J.J. Mock, B.J. Justice, S.A. Cummer, J.B. Pendry, A.F. Starr, D.R. Smith, Metamaterial electromagnetic cloak at microwave frequencies, Science 314 (2006) 977–980.
[7] G.W. Milton, N.-A.P. Nicorovici, On the cloaking effects associated with anomalous localized resonance, Proc. R. Soc. A Math. Phys. 462 (2006) 3027–3059.
[8] M. Maldovan, Sound and heat revolutions in phononics, Nature 503 (2013) 209.
[9] C. Fan, Y. Gao, J. Huang, Shaped graded materials with an apparent negative thermal conductivity, Appl. Phys. Lett. 92 (2008) 251907.
[10] T.Y. Chen, C.-N. Weng, J.-S. Chen, Cloak for curvilinearly anisotropic media in conduction, Appl. Phys. Lett. 93 (2008) 114103.
[11] M. Farhat, S. Guenneau, S. Enoch, Ultrabroadband elastic cloaking in thin plates, Phys. Rev. Lett. 103 (2009) 024301.
[12] N. Stenger, M. Wilhelm, M. Wegener, Experiments on elastic cloaking in thin plates, Phys. Rev. Lett. 108 (2012) 014301.
[13] H.Y. Chen, J. Yang, J. Zi, C.T. Chan, Transformation media for linear liquid surface waves, Europhys. Lett. 85 (2009) 24004.
[14] S. Zhang, D.A. Genov, C. Sun, X. Zhang, Cloaking of matter waves, Phys. Rev. Lett. 100 (2008) 123002.
[15] A. Diatta, S. Guenneau, Non-singular cloaks allow mimesis, J. Opt. 13 (2011) 024012.
[16] H.Y. Chen, C.T. Chan, Acoustic cloaking in three dimensions using acoustic metamaterials, Appl. Phys. Lett. 91 (2007) 183518.
[17] M. Farhat, S. Enoch, S. Guenneau, A.B. Movchan, Broadband cylindrical acoustic cloak for linear surface waves in a fluid, Phys. Rev. Lett. 101 (2008) 134501.
[18] S. Zhang, C.G. Xia, N. Fang, Broadband acoustic cloak for ultrasound waves, Phys. Rev. Lett. 106 (2011) 024301.
[19] J. Li, Y. Gao, J. Huang, A bifunctional cloak using transformation media, J. Appl. Phys. 108 (2010) 074504.
[20] S. Guenneau, C. Amra, D. Veynante, Transformation thermodynamics: cloaking and concentrating heat flux, Opt. Express 20 (2012) 8207–8218.
[21] S. Narayana, Y. Sato, Heat flux manipulation with engineered thermal materials, Phys. Rev. Lett. 108 (2012) 214303.
[22] R. Schittny, M. Kadic, S. Guenneau, M. Wegener, Experiments on transformation thermodynamics: Molding the flow of heat, Phys. Rev. Lett. 110 (2013) 195901.
[23] J.P. Huang, Thermal metamaterial: Geometric structure, working mechanism, and novel function, Prog. Phys. 38 (2018) 219–238.
[24] M. Wegener, Metamaterials beyond optics, Science 342 (2013) 939–940.
[25] M. Kadic, T. Bueckmann, R. Schittny, M. Wegener, Metamaterials beyond electromagnetism, Rep. Progr. Phys. 76 (2013) 126501.
[26] J.P. Huang, Theoretical Thermotics: Transformation Thermotics and Extended Theories for Thermal Metamaterials, Springer, 2020.
[27] J.P. Huang, On theoretical thermotics, Physics 49 (2020) 493–496 (in Chinese).
[28] J. Valentine, S. Zhang, T. Zentgraf, E. Ulin-Avila, D.A. Genov, G. Bartal, X. Zhang, Three-dimensional optical metamaterial with a negative refractive index, Nature 455 (2008) 376–379.
[29] J. Valentine, J. Li, T. Zentgraf, G. Bartal, X. Zhang, An optical cloak made of dielectrics, Nature Mater. 8 (2009) 568–571.
[30] R. Liu, C. Ji, J.J. Mock, J.Y. Chin, T.J. Cui, D.R. Smith, Broadband ground-plane cloak, Science 323 (2009) 366–369.

[31] Y. Lai, J. Ng, H.Y. Chen, D.Z. Han, J.J. Xiao, Z.Q. Zhang, C.T. Chan, Illusion optics: The optical transformation of an object into another object, Phys. Rev. Lett. 102 (2009) 253902.
[32] H.Y. Chen, B. Hou, S.Y. Chen, X.Y. Ao, W.J. Wen, C.T. Chan, Design and experimental realization of a broadband transformation media field rotator at microwave frequencies, Phys. Rev. Lett. 102 (2009) 183903.
[33] T. Ergin, N. Stenger, P. Brenner, J.B. Pendry, M. Wegener, Three-dimensional invisibility cloak at optical wavelengths, Science 328 (2010) 337–339.
[34] S. Xu, X.X. Cheng, S. Xi, R.R. Zhang, H.O. Moser, Z. Shen, Y. Xu, Z.L. Huang, X.M. Zhang, F.X. Yu, B.L. Zhang, H.S. Chen, Experimental demonstration of a free-space cylindrical cloak without superluminal propagation, Phys. Rev. Lett. 109 (2012) 223903.
[35] Z.Y. Liu, X.X. Zhang, Y.W. Mao, Y.Y. Zhu, Z.Y. Yang, C.T. Chan, P. Sheng, Locally resonant sonic materials, Science 289 (2000) 1734.
[36] Y. Zhai, Y.G. Ma, S.N. David, D.L. Zhao, R.N. Lou, G. Tan, R.G. Yang, X.B. Yin, Scalable-manufactured randomized glass-polymer hybrid metamaterial for daytime radiative cooling, Science 355 (2017) 1062–1066.
[37] T. Li, Y. Zhai, S.M. He, W.T. Gan, Z.T. Wei, M. Heidarinejad, D. Dalgo, R.Y. Mi, X.P. Zhao, J.W. Song, J.Q. Dai, C.J. Chen, A. Aili, A. Vellore, A. Martini, R.G. Yang, J. Srebric, X.B. Yin, L.B. Hu, A radiative cooling structural material, Science 364 (2019) 760–763.
[38] T.C. Han, X. Bai, J.T.L. Thong, B.W. Li, C.-W. Qiu, Full control and manipulation of heat signatures: Cloaking, camouflage and thermal metamaterials, Adv. Mater. 26 (2014) 1731.
[39] Y. Li, X. Bai, T.Z. Yang, H.L. Luo, C.-W. Qiu, Structured thermal surface for radiative camouflage, Nature Commun. 9 (2018) 273.
[40] N. Zhu, X. Shen, J. Huang, Converting the patterns of local heat flux via thermal illusion device, AIP Adv. 5 (2015) 053401.
[41] X.Y. Peng, R. Hu, Three-dimensional illusion thermotics with separated thermal illusions, ES Energy Environ. 6 (2019) 39–44.
[42] I. Lienhard, J.H. Lienhard V, A Heat Transfer Textbook, fifth ed., Dover Publications, Mineola, NY, 2019.
[43] X. Shen, J. Huang, Thermally hiding an object inside a cloak with feeling, Int. J. Heat Mass Transfer 78 (2014) 1.
[44] Y. Li, X.Y. Shen, Z.H. Wu, J.Y. Huang, Y.X. Chen, Y.S. Ni, J.P. Huang, Temperature-dependent transformation thermotics: From switchable thermal cloaks to macroscopic thermal diodes, Phys. Rev. Lett. 115 (2015) 195503.
[45] X.Y. Shen, Y. Li, C.R. Jiang, J. Huang, Temperature trapping: Energy-free maintenance of constant temperatures as ambient temperature gradients change, Phys. Rev. Lett. 117 (2016) 055501.
[46] H. Choe, R. Prabhakar, G. Wehmeyer, F.I. Allen, W. Lee, L. Jin, Y. Li, P.D. Yang, C.-W. Qiu, C. Dames, M. Scott, A. Minor, J.-H. Bahk, J.Q. Wu, Ion write microthermotics: Programing thermal metamaterials at the microscale, Nano Lett. 19 (2019) 3830–3837.
[47] R. Hu, X.B. Luo, Two-dimensional phonon engineering triggers microscale thermal functionalities, Nat. Sci. Rev. 6 (2019) 39–44.
[48] Z.Q. Ye, B.Y. Cao, Nanoscale thermal cloaking in graphene via chemical functionalization, Phys. Chem. Chem. Phys. 18 (2016) 32952.
[49] T.C. Han, P. Yang, Y. Li, D.Y. Lei, B.W. Li, K. Hippalgaonkar, C.-W. Qiu, Full-parameter omnidirectional thermal metadevices of anisotropic geometry, Adv. Mater. 26 (2018) 1731–1734.
[50] G.-X. Yu, Y.-F. Lin, G.-Q. Zhang, Z. Yu, L.-L. Yu, J. Su, Design of square-shaped heat flux cloaks and concentrators using method of coordinate transformation, Front. Phys. 6 (2011) 70.
[51] T.C. Han, J.J. Zhao, T. Yuan, D.Y. Lei, B.W. Li, C.-W. Qiu, Theoretical realization of an ultra-efficient thermalenergy harvesting cell made of natural materials, Energy Environ. Sci. 6 (2013) 3537.
[52] R. Kapadia, P. Bandaru, Heat flux concentration through polymeric thermal lenses, Appl. Phys. Lett. 105 (2014) 233903.
[53] J.-L. Wang, H.-C. Zhang, C. Ma, C.-S. Su, H. Shen, G.-N. Xie, Performance of meta-material thermal concentrator with sensu-shaped structure through entropy generation approach, Thermal Sci. 20 (2016) S651–S658.
[54] R.Z. Wang, L.J. Xu, Q. Ji, J. Huang, A thermal theory for unifying and designing transparency, concentrating and cloaking, J. Appl. Phys. 123 (2018) 115117.
[55] Y. Li, X.Y. Shen, J. Huang, Y.S. Ni, Temperature-dependent transformation thermotics for unsteady states: Switchable concentrator for transient heat flow, Phys. Lett. A 380 (2016) 1641.
[56] Y.G. Ma, Y.C. Liu, M. Raza, Y.D. Wang, S.L. He, Experimental demonstration of a multiphysics cloak: Manipulating heat flux and electric current simultaneously, Phys. Rev. Lett. 113 (2014) 205501.
[57] M. Moccia, G. Castaldi, S. Savo, Y. Sato, V. Galdi, Independent manipulation of heat and electrical current via bifunctional metamaterials, Phys. Rev. X 4 (2014) 021025.
[58] C.W. Lan, B. Li, J. Zhou, Simultaneously concentrated electric and thermal fields using fan-shaped structure, Opt. Express 23 (2015) 24475.
[59] T. Stedman, L.M. Woods, Cloaking of thermoelectric transport, Sci. Rep. 7 (2017) 6988.
[60] X.Y. Shen, Y. Li, C.R. Jiang, Y.S. Ni, J.P. Huang, Thermal cloak-concentrator, Appl. Phys. Lett. 109 (2016) 031907.
[61] S. Guenneau, C. Amra, Anisotropic conductivity rotates heat fluxes in transient regimes, Opt. Express 21 (2013) 6578.
[62] F.B. Yang, B.Y. Tian, L.J. Xu, J.P. Huang, Experimental demonstration of thermal chameleonlike rotators with transformation-invariant metamaterials, Phys. Rev. Appl. 14 (2020) 054024.
[63] Y.X. Chen, X.Y. Shen, J.P. Huang, Engineering the accurate distortion of an object's temperature-distribution signature, Eur. Phys. J. Appl. Phys. 70 (2015) 20901.
[64] R. Hu, S.L. Zhou, Y. Li, D.-Y. Lei, X.B. Luo, C.-W. Qiu, Illusion thermotics, Adv. Mater. 30 (2018) 1707237.
[65] T.C. Han, X. Bai, D.L. Gao, J.T.L. Thong, B.W. Li, C.-W. Qiu, Experimental demonstration of a bilayer thermal cloak, Phys. Rev. Lett. 112 (2014) 054302.
[66] H.Y. Xu, X.H. Shi, F. Gao, H.D. Sun, B.L. Zhang, Ultrathin three-dimensional thermal cloak, Phys. Rev. Lett. 112 (2014) 054301.
[67] F. Gömöry, M. Solovyov, J. Souc, C. Navau, J. Prat-Camps, A. Sanchez, Experimental realization of a magnetic cloak, Science 335 (2012) 1466.
[68] Y. Li, K.J. Zhu, Y.G. Peng, W. Li, T.Z. Yang, H.X. Xu, H. Chen, X.F. Zhu, S.H. Fan, C.-W. Qiu, Thermal meta-device in analogue of zero-index photonics, Nature Mater. 18 (2019) 48–54.
[69] L.J. Xu, S. Yang, J.P. Huang, Effectively infinite thermal conductivity and zero-index thermal cloak, Europhys. Lett. 131 (2020) 24002.
[70] T.Z. Yang, Y.S. Su, W.K. Xu, X.D. Yang, Transient thermal camouflage and heat signature control, Appl. Phys. Lett. 109 (2016) 121905.
[71] T.Z. Yang, X. Bai, D.L. Gao, L.Z. Wu, B.W. Li, J.T.L. Thong, C.-W. Qiu, Invisible sensors: Simultaneous sensing and camouflaging in multiphysical fields, Adv. Mater. 27 (2015) 7752.
[72] P. Jin, L.J. Xu, T. Jiang, L. Zhang, J.P. Huang, Making thermal sensors accurate and invisible with an anisotropic monolayer scheme, Int. J. Heat Mass Trasfer 163 (2020) 120437.
[73] R.Z. Wang, J. Shang, J. Huang, Design and realization of thermal camouflage with many-particle systems, Int. J. Therm. Sci. 131 (2018) 14.
[74] X. He, L.Z. Wu, Thermal transparency with the concept of neutral inclusion, Phys. Rev. E 88 (2013) 033201.
[75] L.W. Zeng, R.X. Song, Experimental observation of heat transparency, Appl. Phys. Lett. 104 (2014) 201905.
[76] S. Yang, L. Xu, R. Wang, J. Huang, Full control of heat transfer in single-particle structural materials, Appl. Phys. Lett. 111 (2017) 121908.
[77] J. Shang, C.R. Jiang, L.J. Xu, J. Huang, Many-particle thermal invisibility and diode from effective media, J. Heat Trans. 140 (2018) 092004.
[78] R.Z. Wang, L.J. Xu, J. Huang, Thermal imitators with single directional invisibility, J. Appl. Phys. 122 (2017) 215107.
[79] L.J. Xu, S. Yang, J.P. Huang, Thermal transparency induced by periodic interparticle interaction, Phys. Rev. Appl. 11 (2019) 034056.
[80] J. Shang, B.Y. Tian, C.R. Jiang, J.P. Huang, Digital thermal metasurface with arbitrary infrared thermogram, Appl. Phys. Lett. 113 (2018) 261902.

[81] L.J. Xu, S. Yang, J.P. Huang, Designing effective thermal conductivity of materials of core-shell structure: Theory and simulation, Phys. Rev. E 99 (2019) 022107.
[82] L.J. Xu, S. Yang, J.P. Huang, Thermal theory for heterogeneously architected structure: Fundamentals and application, Phys. Rev. E 98 (2018) 052128.
[83] L.J. Xu, S. Yang, J.P. Huang, Passive metashells with adaptive thermal conductivities: Chameleonlike behavior and its origin, Phys. Rev. Appl. 11 (2019) 054071.
[84] R.G. Peng, Z.Q. Xiao, Q. Zhao, F.L. Zhang, Y.G. Meng, B. Li, J. Zhou, Y.C. Fan, P. Zhang, N.-H. Shen, T. Koschny, C.M. Soukoulis, Temperature-controlled chameleonlike cloak, Phys. Rev. X 7 (2017) 011033.
[85] J. Zi, X.D. Yu, Y.Z. Li, X.H. Hu, C. Xu, X.J. Wang, X.H. Liu, R.T. Fu, Coloration strategies in peacock feathers, Proc. Natl. Acad. Sci. 100 (2003) 12576.
[86] Y.F. Zhang, B.Q. Dong, A. Chen, X. Shi, L. Shi, J. Zi, Using cuttlefish ink as an additive to produce non-iridescent structural colors of high color visibility, Adv. Mater. 27 (2015) 4719.
[87] V.S. Ramachandran, C.W. Tyler, R.L. Gregory, D. Rogers-Ramachandran, S. Duensing, C. Pillsbury, C. Ramachandran, Rapid adaptive camouflage in tropical flounders, Nature 379 (1996) 815.
[88] C.J. Yu, Y.H. Li, X. Zhang, X. Huang, V. Malyarchuk, S.D. Wang, Y. Shi, L. Gao, Y.W. Su, Y.H. Zhang, H.X. Xu, R.T. Hanlon, Y.G. Huang, J.A. Rogers, Adaptive optoelectronic camouflage systems with designs inspired by cephalopod skins, Proc. Natl. Acad. Sci. 111 (2014) 12998.
[89] N.N. Shi, C.C. Tsai, F. Camino, G.D. Bernard, N.F. Yu, R. Wehner, Keeping cool: Enhanced optical reflection and radiative heat dissipation in Saharan silver ants, Science 349 (2015) 298–301.
[90] S.R. Sklan, X. Bai, B.W. Li, X. Zhang, Detecting thermal cloaks via transient effects, Sci. Rep. 6 (2016) 32915.
[91] J.P. Huang, K.W. Yu, Enhanced nonlinear optical responses of materials: Composite effects, Phys. Rep. 431 (2006) 87–172.
[92] G.L. Dai, J. Shang, R.Z. Wang, J. Huang, Nonlinear thermotics: nonlinearity enhancement and harmonic generation in thermal metasurfaces, Eur. Phys. J. B 91 (2018) 59.
[93] S. Yang, L.J. Xu, J.P. Huang, Metathermotics: Nonlinear thermal responses of core-shell metamaterials, Phys. Rev. E 99 (2019) 04214.
[94] G.L. Dai, J.P. Huang, Nonlinear thermal conductivity of periodic composites, Int. J. Heat Mass Transfer 147 (2019) 118917.
[95] J. Wang, G.L. Dai, F.B. Yang, J.P. Huang, Designing bistability or multistability in macroscopic diffusive systems, Phys. Rev. E 101 (2020) 022119.
[96] L. Wang, B.W. Li, Thermal memory: A storage of phononic information, Phys. Rev. Lett. 101 (2008) 267203.
[97] J. Wang, J. Shang, J.P. Huang, Negative energy consumption of thermostats at ambient temperature: Electricity generation with zero energy maintenance, Phys. Rev. Appl. 11 (2019) 024053.
[98] L.J. Xu, J.P. Huang, Metamaterials for manipulating thermal radiation: Transparency, cloak, and expander, Phys. Rev. Appl. 12 (2019) 044048.
[99] L.J. Xu, S. Yang, J.P. Huang, Dipole-assisted thermotics: Experimental demonstration of dipole-driven thermal invisibility, Phys. Rev. E 100 (2019) 062108.
[100] L.J. Xu, R.Z. Wang, J.P. Huang, Camouflage thermotics: A cavity without disturbing heat signatures outside, J. Appl. Phys. 123 (2018) 245111.
[101] X. He, L.Z. Wu, Illusion thermodynamics: A camouflage technique changing an object into another one with arbitrary cross section, Appl. Phys. Lett. 105 (2014) 221904.
[102] S.L. Zhou, R. Hu, X.B. Luo, Thermal illusion with twinborn-like heat signatures, Int. J. Heat Mass Transfer 127 (2018) 607.
[103] R. Hu, S.Y. Huang, M. Wang, X.L. Luo, J. Shiomi, C.-W. Qiu, Encrypted thermal printing with regionalization transformation, Adv. Mater. 31 (2019) 1807849.
[104] J.X. Li, Y. Li, T.L. Li, W.Y. Wang, L.Q. Li, C.-W. Qiu, Doublet thermal metadevice, Phys. Rev. Appl. 11 (2019) 044021.
[105] J. Ren, P. Hanggi, B.W. Li, Berry-phase-induced heat pumping and its impact on the fluctuation theorem, Phys. Rev. Lett. 104 (2010) 170601.
[106] J. Ren, S. Liu, B.W. Li, Geometric heat flux for classical thermal transport in interacting open systems, Phys. Rev. Lett. 108 (2012) 210603.
[107] M. Maldovan, Narrow low-frequency spectrum and heat management by thermocrystals, Phys. Rev. Lett. 110 (2013) 025902.
[108] B.L. Davis, M.I. Hussein, Nanophononic metamaterial: Thermal conductivity reduction by local resonance, Phys. Rev. Lett. 112 (2014) 055505.
[109] T.S. Zhu, K. Swaminathan-Gopalan, K.J. Cruse, K. Stephani, E. Ertekin, Vibrational energy transport in hybrid ordered/disordered nanocomposites: Hybridization and avoided crossings of localized and delocalized modes, Adv. Funct. Mater. 28 (2018) 1706268.
[110] M. Sledzinska, B. Graczykowski, J. Maire, E. Chavez-Angel, C. Sotomayor-Torres, F. Alzina, 2d phononic crystals: Progress and prospects in hypersound and thermal transport engineering, Adv. Funct. Mater. 30 (2019) 1904434.
[111] M.I. Hussein, C.N. Tsai, H. Honarvar, Thermal conductivity reduction in a nanophononic metamaterial versus a nanophononic crystal: A review and comparative analysis, Adv. Funct. Mater. 30 (2020) 8.
[112] K.Y. Fong, H.K. Li, R.K. Zhao, S. Yang, Y. Wang, X. Zhang, Phonon heat transfer across a vacuum through quantum fluctuations, Nature 576 (2019) 243.
[113] J.B. Pendry, K. Sasihithlu, R.V. Craster, Phonon-assisted heat transfer between vacuum-separated surfaces, Phys. Rev. B 94 (2016) 075414.
[114] E.M. Dede, P. Schmalenberg, T. Nomura, M. Ishigaki, Design of anisotropic thermal conductivity in multilayer printed circuit boards, IEEE Trans. Compon. Packag. Manuf. 5 (2015) 1763.
[115] E.M. Dede, P. Schmalenberg, C.-M. Wang, F. Zhou, T. Nomura, Collection of low-grade waste heat for enhanced energy harvesting, AIP Adv. 6 (2016) 055113.
[116] S. Guenneau, T. Puvirajesinghe, Fick's second law transformed: one path to cloaking in mass diffusion, J. Royal Soc. Interface 10 (2013) 20130106.
[117] S. Guenneau, D. Petiteau, M. Zerrad, C. Amra, T.M. Puvirajesinghe, Transformed fourier and fick equations for the control of heat and mass diffusion, AIP Adv. 5 (2015) 053404.
[118] L.D. Landau, E.M. Lifshitz, Fluid Mechanics, Elsevier, 1987.
[119] G.L. Dai, J. Shang, J. Huang, Theory of transformation thermal convection for creeping flow in porous media: Cloaking, concentrating, and camouflage, Phys. Rev. E 97 (2018) 022129.
[120] G.L. Dai, J.P. Huang, A transient regime for transforming thermal convection: Cloaking, concentrating, and rotating creeping flow and heat flux, J. Appl. Phys. 124 (2018) 235103.
[121] Y.A. Urzhumov, D.R. Smith, Fluid flow control with transformation media, Phys. Rev. Lett. 107 (2011) 074501.
[122] H.F. Burcharth, O.H. Andersen, On the one-dimensional steady and unsteady porous flow equations, Coastal Eng. 24 (1995) 233.
[123] T. Zhu, C. Waluga, B. Wohlmuth, M. Manhar, A study of the time constant in unsteady porous media flow using direct numerical simulation, Transp. Porous Media 104 (2014) 161.
[124] T. Zhu, M. Manhar, Oscillatory Darcy flow in porous media, Transp. Porous Media 111 (2016) 521.
[125] J. Bear, Dynamics of Fluids in Porous Media, Elsevier, 1972.
[126] J. Bear, M.Y. Corapcioglu, Fundamentals of Transport Phenomena in Porous Media, Springer, 1984.
[127] M. Rahm, D. Schurig, D.A. Roberts, S.A. Cummer, D.R. Smith, J.B. Pendry, Design of electromagnetic cloaks and concentrators using form-invariant coordinate transformations of Maxwell's equations, Photon. Nanostruct.: Fundam. Appl. 6 (2008) 87.
[128] H. Chen, C.T. Chan, Transformation media that rotate electromagnetic fields, Appl. Phys. Lett. 90 (2007) 241105.
[129] Y.A. Urzhumov, D.R. Smith, Flow stabilization with active hydrodynamic cloaks, Phys. Rev. E 86 (2012) 056313.

[130] P.T. Bowen, D.R. Smith, Y.A. Urzhumov, Wake control with permeable multilayer structures: The spherical symmetry case, Phys. Rev. E 92 (2015) 063030.
[131] D.R. Culver, E. Dowell, D. Smith, Y. Urzhumov, A. Varghese, A volumetric approach to wake reduction: Design, optimization, and experimental verification, J. Fluids 2016 (2016) 3587974.
[132] J. Park, J.R. Youn, Y.S. Song, Hydrodynamic metamaterial cloak for drag-free flow, Phys. Rev. Lett. 123 (2019) 074502.
[133] J. Park, J.R. Youn, Y.S. Song, Fluid-flow rotator based on hydrodynamic metamaterial, Phys. Rev. Appl. 12 (2019) 061002.
[134] L.J. Xu, J.P. Huang, Negative thermal transport in conduction and advection, Chin. Phys. Lett. (Express Letter) 37 (2020) 080502.
[135] L.J. Xu, J.P. Huang, Controlling thermal waves with transformation complex thermotics, Int. J. Heat Mass Transfer 159 (2020) 120133.
[136] L.J. Xu, J.P. Huang, Active thermal wave cloak, Chin. Phys. Lett. 37 (2020) 120501.
[137] F.B. Yang, L.J. Xu, J.P. Huang, Thermal illusion of porous media with convection-diffusion process: Transparency, concentrating, and cloaking, ES Energy Environ. 6 (2019) 45–50.
[138] W.-S. Yeung, V.-P. Mai, R.-J. Yang, Cloaking: Controlling thermal and hydrodynamic fields simultaneously, Phys. Rev. Appl. 13 (2020) 064030.
[139] C.M. Bender, S. Boettcher, Real spectra in non-hermitian hamiltonians having PT symmetry, Phys. Rev. Lett. 80 (1998) 5243–5246.
[140] Y. Li, Y. Peng, L. Han, M.A. Miri, W. Li, M. Xiao, X.F. Zhu, J.L. Zhao, A. Alù, S.H. Fan, C.-W. Qiu, Anti-parity-time symmetry in diffusive systems, Science 364 (2019) 170–173.
[141] P.C. Cao, Y. Li, Y.G. Peng, C.-W. Qiu, High-order exceptional points in diffusive systems: Robust APT symmetry 2 against perturbation and phase oscillation at APT symmetry breaking, ES Energy Environ. 7 (2020) 48–55.
[142] L.J. Xu, J. Wang, G.L. Dai, S. Yang, F.B. Yang, G. Wang, J.P. Huang, Geometric phase, effective conductivity enhancement, and invisibility cloak in thermal convection-conduction, Int. J. Heat Mass Transfer 165 (2021) 120659.
[143] L.J. Xu, G.L. Dai, G. Wang, J.P. Huang, Geometric phase and bilayer cloak in macroscopic particle-diffusion systems, Phys. Rev. E 102 (2020) 032140.
[144] L.J. Xu, J.P. Huang, Thermal convection-diffusion crystal for prohibition and modulation of wave-like temperature profiles, Appl. Phys. Lett. 117 (2020) 011905.
[145] D.R. Smith, W.J. Padilla, D. Vier, S.C. Nemat-Nasser, S. Schultz, Composite medium with simultaneously negative permeability and permittivity, Phys. Rev. Lett. 84 (18) (2000) 4184–4187.
[146] R.A. Shelby, D.R. Smith, S. Schultz, Experimental verification of a negative index of refraction, Science 292 (5514) (2001) 77–79.
[147] L.J. Xu, J.P. Huang, Chameleonlike metashells in microfluidics: A passive approach to adaptive responses, Sci. China-Phys. Mech. Astron. 63 (2020) 228711.
[148] L.J. Xu, G.L. Dai, J.P. Huang, Transformation multithermotics: Controlling radiation and conduction simultaneously, Phys. Rev. Appl. 13 (2020) 024063.
[149] S. Rosseland, Astrophysik auf atomtheoretischer Grundlage, Springer, 1931.
[150] S.P. Clark, Radiative transfer ia the Earth's mantle, EOS Trans. Am. Geophys. Union 38 (1957) 6.
[151] D. Dan, H. Zhang, W.Q. Tao, Effective structure of aerogels and decomposed contributions of its thermal conductivity, Appl. Therm. Eng. 72 (2014) 2–9.
[152] Y.J. Dai, Y.Q. Tang, W.Z. Fang, H. Zhang, W.Q. Tao, A theoretical model for the effective thermal conductivity of silica aerogel composites, Appl. Therm. Eng. 128 (2017) 1634–1645.
[153] S. Rosseland, Theoretical Astrophysics, Oxford Univ. Press, 1936.
[154] Y. Hanzawa, H. Hatori, N. Yoshizawa, Y. Yamada, Structural changes in carbon aerogels with high temperature treatment, Appl. Energy 40 (2002) 575.
[155] X. Xu, Q.Q. Zhang, M.L. Hao, Y. Hu, Z.Y. Lin, L.L. Peng, T. Wang, X.X. Ren, C. Wang, Z.P. Zhao, C.Z. Wan, H.L. Fei, L. Wang, J. Zhu, H.T. Sun, W.L. Chen, T. Du, B.W. Deng, G.J. Cheng, C. Shakir, T.S. Fisher, X. Zhang, H. Li, Y. Huang, X.F. Duan, Double-negative-index ceramic aerogels for thermal superinsulation, Science 363 (2019) 723.
[156] J.R. Howell, M.P. Menguc, R. Siegel, Thermal Radiation Heat Transfer, CRC Press, 2016.
[157] P. Ben-Abdallah, S.-A. Biehs, Near-field thermal transistor, Phys. Rev. Lett. 112 (2014) 044301.
[158] V. Kubytskyi, S.-A. Biehs, P. Ben-Abdallah, Radiative bistability and thermal memory, Phys. Rev. Lett. 113 (2014) 074301.
[159] V. Fernandez-Hurtado, F.J. Garcła-Vidal, S.H. Fan, J.C. Cuevas, Enhancing near-field radiative heat transfer with si-based metasurfaces, Phys. Rev. Lett. 118 (2017) 203901.
[160] Y. Tian, C.Y. Zhao, A review of solar collectors and thermal energy storage in solar thermal applications, Appl. Energy 104 (2013) 538.
[161] A.P. Raman, M.A. Anoma, L.X. Zhu, E. Rephaeli, S.H. Fan, Passive radiative cooling below ambient air temperature under direct sunlight, Nature 515 (2014) 540.
[162] K.L. Nguyen, O. Merchiers, P.O. Chapuis, Temperature-dependent and optimized thermal emission by spheres, Appl. Phys. Lett. 112 (2018) 111906.
[163] S. Kang, J. Cha, K. Seo, S. Kim, Y. Cha, H. Lee, J. Park, W. Choi, Temperature-responsive thermal metamaterials enabled by modular design of thermally tunable unit cells, Int. J. Heat Mass Transfer 130 (2019) 469.
[164] G.W. Milton, The Theory of Composites, Cambridge Univ. Press, 2004.
[165] Y.R. Qu, Q. Li, L. Cai, M.Y. Pan, P. Ghosh, K.K. Du, M. Qiu, Thermal camouflage based on the phase-changing material GST, Light-Sci. Appl. 7 (2018) 26.
[166] B.W. Li, L. Wang, G. Casati, Thermal diode: Rectification of heat flux, Phys. Rev. Lett. 93 (18) (2004) 184301.
[167] K.P. Vemuri, P.R. Bandaru, Anomalous refraction of heat flux in thermal metamaterials, Appl. Phys. Lett. 104 (2014) 083901.
[168] T.Z. Yang, K.P. Vemuri, P.R. Bandaru, Experimental evidence for the bending of heat flux in a thermal metamaterial, Appl. Phys. Lett. 105 (2014) 083908.
[169] K. Vemuri, F. Canbazoglu, P.R. Bandaru, Guiding conductive heat flux through thermal metamaterials, Appl. Phys. Lett. 105 (2014) 193904.
[170] K. Tang, X. Wang, K. Dong, Y. Li, J. Li, B. Sun, X. Zhang, C. Dames, C.-W. Qiu, J. Yao, J. Wu, A thermal radiation modulation platform by emissivity engineering with graded metal–insulator transition, Adv. Mater. 32 (2020) 1907071.
[171] S. Basu, Z.M. Zhang, C.J. Fu, Review of near-field thermal radiation and its application to energy conversion, Int. J. Energy Res. 33 (2009) 1203–1232.
[172] C.M. Hargreaves, Anomalous radiative transfer between closely-spaced bodies, Phys. Lett. A 30 (1969) 491–492.
[173] L. Hu, A. Narayanaswamy, X.Y. Chen, G. Chen, Near-field thermal radiation between two closely spaced glass plates exceeding Planck's blackbody radiation law, Appl. Phys. Lett. 92 (2008) 220–222.
[174] L.J. Xu, S. Yang, G.L. Dai, J.P. Huang, Transformation omnithermotics: Simultaneous manipulation of three basic modes of heat transfer, ES Energy Environ. 7 (2020) 65–70.
[175] M.Q. Brewster, Thermal Radiative Transfer and Properties, Wiley, 1992.
[176] F. Bellet, E. Chalopin, F. Fichot, E. Iacona, J. Taine, Rdfi determination of anisotropic and scattering dependent radiative conductivity tensors in porous media: Application to rod bundles, Int. J. Heat Mass Transfer 52 (2009) 1544–1551.

[177] J. Taine, F. Bellet, V. Leroy, E. Iacona, Generalized radiative transfer equation for porous medium upscaling: Application to the radiative Fourier law, Int. J. Heat Mass Transfer 53 (2010) 4071–4081.
[178] H. Gomart, J. Taine, Validity criterion of the radiative Fourier law for an absorbing and scattering medium, Phys. Rev. E 83 (2011) 021202.
[179] Y. Liu, D. Pan, W. Chen, W.Q. Wang, H. Shen, H.X. Xu, Radiative heat transfer in nanophotonics: From thermal radiation enhancement theory to radiative cooling applications, Acta. Phys. Sin. 69 (2020) 036501.
[180] E. Rephaeli, A.P. Raman, S.H. Fan, Ultrabroadband photonic structures to achieve high-performance daytime radiative cooling, Nano Lett. 13 (2013) 1457.
[181] J. Mandal, Y. Fu, A.C. Overvig, M. Jia, K. Sun, N.N. Shi, H. Zhou, X. Xiao, N. Yu, Y. Yang, Hierarchically porous polymer coatings for highly efficient passive daytime radiative cooling, Science 362 (2018) 315–319.
[182] Z. Chen, L.X. Zhu, W. Li, S.H. Fan, Simultaneously and synergistically harvest energy from the sun and outer space, Joule 3 (2018) 1–10.
[183] Z. Chen, L.X. Zhu, A. Raman, S.H. Fan, Radiative cooling to deep sub-freezing temperatures through a 24-h day-night cycle, Nature Commun. 7 (2016) 13729.
[184] C.Y. Liu, Y.Z. Wu, B.X. Wang, C.Y. Zhao, H. Bao, Effect of atmospheric water vapor on radiative cooling performance of different surfaces, Sol. Energy 183 (2019) 218–225.
[185] A.W. Harrison, M.R. Walton, Radiative cooling of TiO_2 white paint, Sol. Energy 20 (1978) 185–188.
[186] C.I. Ezekwe, Performance of a heat pipe assisted night sky radiative cooler, Energy Convers. Manage. 30 (1990) 403–408.
[187] E.A. Goldstein, A.P. Raman, S.H. Fan, Sub-ambient non-evaporative fluid cooling with the sky, Nat. Energy 2 (2017) 17143.
[188] D.L. Zhao, A. Aili, Y. Zhai, J.T. Lu, D. Kidd, G. Tan, X.B. Yin, Y.G. Yang, Subambient cooling of water: Toward real-world applications of daytime radiative cooling, Joule 3 (2019) 111–123.
[189] L.X. Zhu, A.P. Raman, S.H. Fan, Radiative cooling of solar absorbers using a visibly transparent photonic crystal thermal blackbody, Proc. Natl. Acad. Sci. 112 (2015) 12282.
[190] L.X. Zhu, A.P. Raman, K.X. Wang, M.A. Anoma, S.H. Fan, Radiative cooling of solar cells, Optica 1 (2014) 32–38.
[191] W. Li, Y. Shi, K.F. Chen, L.X. Zhu, S.H. Fan, A comprehensive photonic approach for solar cell cooling, ACS Photonics 4 (2017) 774.
[192] J. Guadarrama-Cetina, A. Mongrued, M.-G. Medici, E. Baquero, A.R. Parker, I. Milimouk-Melnytchuk, W. Gonzalez-Vinas, D. Beysens, Dew condensation on desert beetle skin, Eur. Phys. J. E 37 (2014) 109.
[193] M. Benlattar, S. Laatioui, E.M. Oualim, M. Mazroui, A. Mouhsen, M. Harmouchi, Numerical modelling of lawsonite thin film as radiative cooling minerals for dew harvesting, Results Phys. 7 (2017) 1959–1964.
[194] M. Zhou, H.M. Song, X.Y. Xu, A. Shahsafi, Z.Y. Xia, Z.Q. Ma, M. Kats, J. Zhu, B.S. Ooi, Q.Q. Gan, Accelerating vapor condensation with daytime radiative cooling, Proc. SPIE 11121 (2018) 1112107.
[195] J.K. Tong, X.P. Huang, S.V. Boriskina, J. Loomis, Y.F. Xu, G. Chen, Infrared-transparent visible-opaque fabrics for wearable personal thermal management, ACS Photonics 2 (2015) 769–778.
[196] P.-C. Hsu, A.Y. Song, P.B. Catrysse, C. Liu, Y.C. Peng, J. Xie, S.H. Fan, Y. Cui, Radiative human body cooling by nanoporous polyethylene textile, Science 353 (2016) 1019.
[197] Y.C. Peng, J. Chen, A.Y. Song, P.B. Catrysse, P.C. Hsu, L.L. Cai, B.F. Liu, Y.Y. Zhu, G.M. Zhou, D.S. Wu, Nanoporous polyethylene microfibres for large-scale radiative cooling fabric, Nat. Sustain. 1 (2018) 105–112.
[198] J. Wang, F.B. Yang, L.J. Xu, J.P. Huang, Omnithermal restructurable metasurfaces for both infrared-light illusion and visible-light similarity, Phys. Rev. Appl. 14 (2020) 014008.
[199] J.C. Cuevas, F.J. Garcła-Vidal, Radiative heat transfer, ACS Photonics 5 (2018) 3896.
[200] Y. Ohwada, Calculation of the effective emissivity of a cavity having non-lambertian isothermal surfaces, J. Opt. Soc. Amer. A 16 (1999) 1059.
[201] G. Mei, J. Zhang, S. Zhao, Z. Xie, Simple method for calculating the local effective emissivity of the blackbody cavity as a temperature sensor, Infrared Phys. Technol. 85 (2017) 372.
[202] L. Bao, T.J. Cui, Tunable, reconfigurable, and programmable metamaterials, Microw. Opt. Technol. Lett. 62 (2020) 9.
[203] S. Yang, L.J. Xu, G.L. Dai, J.P. Huang, Omnithermal metamaterials switchable between transparency and cloaking, J. Appl. Phys. 128 (2020) 095102.
[204] D. Torrent, O. Poncelet, J.C. Batsale, Nonreciprocal thermal material by spatiotemporal modulation, Phys. Rev. Lett. 120 (2018) 125501.
[205] Q.C. Weng, S. Komiyama, L. Yang, Z.H. An, P.P. Chen, S.A. Biehs, Y. Kajihara, W. Lu, Imaging of nonlocal hot-electron energy dissipation via shot noise, Science 360 (2018) 775–778.
[206] R.J. Qian, X. Gong, H.Y. Xue, W.K. Lu, L.P. Zhu, Z.H. An, Developments on thermometric techniques in probing micro- and nano-heat, ES Energy Environ. 6 (2019) 4–17.
[207] J. Wang, G.L. Dai, J.P. Huang, Thermal metamaterial: Fundamental, application, and outlook, iScience 23 (2020) 101637.
[208] P. Ben-Abdallah, S.A. Biehs, Phase-change radiative thermal diode, Appl. Phys. Lett. 103 (2013) 191907.
[209] N.B. Li, J. Ren, L. Wang, G. Zhang, P. Hänggi, B.W. Li, Phononics: Manipulating heat flow with electronic analogs and beyond, Rev. Modern Phys. 84 (2012) 1045.
[210] D. Loke, J.M. Skelton, T.-C. Chong, S.R. Elliott, Design of a nanoscale, CMOS-integrable, thermal-guiding structure for boolean-logic and neuromorphic computation, ACS Appl. Mater. Interfaces 8 (2016) 34530.
[211] X. Zheng, B.W. Li, Effect of interfacial thermal resistance in a thermal cloak, Phys. Rev. Appl. 13 (2020) 024071.
[212] D. Liu, R.G. Xie, N. Yang, B.W. Li, J.T.L. Thong, Profiling nanowire thermal resistance with a spatial resolution of nanometers, Nano Lett. 14 (2014) 806–812.
[213] C.W. Lan, K. Bi, X.J. Fu, B. Li, J. Zhou, Bifunctional metamaterials with simultaneous and independent manipulation of thermal and electric fields, Opt. Express 24 (2016) 23080.
[214] W.C. Shi, T. Stedman, L.M. Woods, Transformation optics for thermoelectric flow, J. Phys. Energy 1 (2019) 025002.
[215] W.C. Shi, T. Stedman, L.M. Woods, Thermoelectric transport control with metamaterial composites, J. Appl. Phys. 128 (2020) 025104.